

**Search for supersymmetry using boosted Higgs bosons and  
missing transverse momentum in proton-proton collisions  
at 13 TeV**

by

**Frank Jensen**

M.S., University of Colorado Boulder, 2014

B.A., University of California Berkeley, 2008

A thesis submitted to the  
Faculty of the Graduate School of the  
University of Colorado in partial fulfillment  
of the requirements for the degree of  
Doctor of Philosophy  
Department of Physics

2018

This thesis entitled:  
Search for supersymmetry using boosted Higgs bosons and missing transverse momentum in  
proton-proton collisions at 13 TeV  
written by Frank Jensen  
has been approved for the Department of Physics

---

Professor Kevin Stenson

---

Professor William Ford

---

Professor Jamie Nagle

---

Professor Markus Pflaum

---

Professor Senarath de Alwis

Date \_\_\_\_\_

The final copy of this thesis has been examined by the signatories, and we find that both the content and the form meet acceptable presentation standards of scholarly work in the above mentioned discipline.

Jensen, Frank (Ph.D., experimental high-energy physics)

Search for supersymmetry using boosted Higgs bosons and missing transverse momentum in proton-proton collisions at 13 TeV

Thesis directed by Professor Kevin Stenson

A search for physics beyond the Standard Model (SM) in events with one or more high-momentum Higgs bosons ( $H$ ) decaying to pairs of  $b$  quarks in association with missing transverse momentum is presented. The data, corresponding to an integrated luminosity of  $35.9 \text{ fb}^{-1}$ , were collected with the CMS detector at the Large Hadron Collider in proton-proton collisions at the center-of-mass energy  $\sqrt{s} = 13 \text{ TeV}$ . The analysis utilizes a new  $b$  quark tagging technique based on jet substructure to identify jets from  $H \rightarrow b\bar{b}$ . Events are categorized by the multiplicity of  $H$ -tagged jets, jet mass, and the missing transverse momentum. No significant deviation from SM expectations is observed. In the context of supersymmetry (SUSY), limits on the cross sections of pair-produced gluinos are set, assuming that gluinos decay to quark pairs,  $H$  or  $Z$  bosons, and the lightest SUSY particle (LSP). The decay chain proceeds through an intermediate SUSY particle, assumed to be the second lightest in the theory (NLSP). With large mass splitting between the NLSP and LSP, and 100% NLSP branching fraction to  $H$ , the lower limit on the gluino mass is found to be 2010 GeV.

## **Dedications**

*The taxpayers.*

## Contents

### Chapter

<b>1</b>	<b>Introduction</b>	<b>1</b>
<b>2</b>	<b>The Standard Model of Particle Physics</b>	<b>2</b>
2.1	Introduction . . . . .	2
2.2	Quantum Electrodynamics . . . . .	3
2.3	Quantum Chromodynamics . . . . .	4
2.3.1	Confinement, Hadrons, & the Quark Model . . . . .	6
2.4	Electroweak Theory . . . . .	7
2.4.1	Introduction . . . . .	7
2.4.2	The Higgs Mechanism . . . . .	9
2.4.3	Quark Mixing - the CKM Matrix . . . . .	12
2.4.4	Brief Electroweak Summary . . . . .	13
2.5	Parameters of the Standard Model . . . . .	13
2.6	Neutrino Mass . . . . .	14
<b>3</b>	<b>The Minimal Supersymmetric Model</b>	<b>16</b>
<b>4</b>	<b>The Large Hadron Collider</b>	<b>22</b>
<b>5</b>	<b>The CMS Detector</b>	<b>25</b>
5.1	Silicon Tracker . . . . .	26

5.1.1	Pixel Detector	28
5.1.2	Strips Detector	29
5.2	Electromagnetic Calorimeter	29
5.2.1	Preshower	31
5.3	Hadronic Calorimeter	31
5.4	Solenoidal Magnet	32
5.5	Muon System	34
5.5.1	Drift Tubes	35
5.5.2	Cathode Strip Chambers	35
5.5.3	Resistive Plate Chambers	37
5.6	Trigger System	38
<b>6</b>	<b>Event Reconstruction</b>	<b>40</b>
6.1	Basic Elements From the Detector	40
6.1.1	Tracks and Vertices	40
6.1.2	ECAL & HCAL Clusters	41
6.1.3	Muon Tracks	42
6.2	Obtaining a Particle-level Description	42
6.3	Additional High-Level Objects	45
6.3.1	Jets	45
6.3.2	b-tagging of Jets	45
6.3.3	Invisible Particles $\rightarrow p_T^{\text{miss}}$	46
6.3.4	$\pi^0$ meson	46
<b>7</b>	<b>Search for new physics using boosted H bosons and missing energy</b>	<b>47</b>
7.1	Motivation & Strategy	47
7.2	Object Definition & Event Selection	49
7.3	Dataset & Trigger	50

7.4	Event Simulation . . . . .	52
7.4.1	Standard Model Processes . . . . .	52
7.4.2	Signal Models . . . . .	54
7.5	Event Binning & Background Estimation . . . . .	54
7.5.1	Control Regions within Data . . . . .	57
7.5.2	$\kappa$ as a Correction to the Estimation . . . . .	59
7.5.3	Sideband Yields & Predictions . . . . .	68
7.6	Signal Systematics . . . . .	69
7.7	Results - Yields in the Signal Regions & Exclusion Curves . . . . .	73
<b>8</b>	<b>Conclusions</b>	<b>76</b>
 <b>Appendix</b>		
<b>A</b>	<b>Reinterpretation</b>	<b>78</b>
<b>B</b>	<b><math>b\bar{b}</math>-tagging Scale Factors for W jets in <math>t\bar{t}</math> Events</b>	<b>83</b>
 <b>Bibliography</b>		<b>87</b>

## Tables

### Table

2.1	Summary of field content within the SM. . . . .	3
3.1	Summary of the additional particle content within the MSSM. . . . .	17
3.2	Mixing of the supersymmetric electroweak fields. . . . .	17
6.1	Seeding requirements for each step in the iterative track reconstruction. . . . .	41
7.1	SM samples used in the analysis. . . . .	53
7.2	Summary of the control region scale-factors integrated over $p_T^{\text{miss}}$ . . . . .	65
7.3	Single lepton control region scale-factors in the anti-tag sideband region. . . . .	65
7.4	The $\kappa$ factor computed by throwing Gaussian toys for the scale factors. . . . .	66
7.5	Corrected yields in the signal regions. $\kappa = \text{AD} / \text{BC}$ . . . . .	67
7.6	Corrected yields in the sideband regions. $\kappa = \text{AD} / \text{BC}$ . . . . .	67
7.7	Sideband region yields, $\kappa$ , and background predictions for the 6 signal bins. . . . .	69
7.8	Fit results for W-mass resolution in data and simulation. . . . .	71
7.9	Summary of signal shape and normalization uncertainties. . . . .	72
7.10	Signal yields and background predictions. . . . .	73
A.1	Comparison of the true reco-level event yield with those obtained via the prediction. . . . .	81
A.2	T5HH signal event efficiencies. . . . .	81
A.3	T5HH/ZH signal event cutflow. . . . .	82

B.1 W jet $b\bar{b}$ mistag rates in data and simulation, inclusive in $p_T$ . Errors are statistical only. . . . .	85
B.2 Summary of scale factors for $b\bar{b}$ -tagging W jets in $t\bar{t}$ events. . . . .	86

## Figures

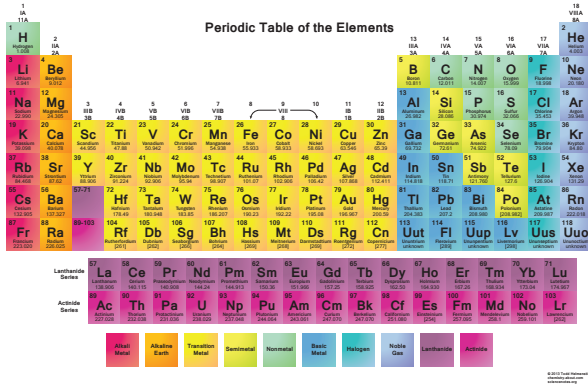
### Figure

2.1	SU(3) flavor symmetry multiplets predicted by the quark model.	7
3.1	Interactions between SM and MSSM particles.	19
3.2	Tree-level gluino pair-production mechanisms.	20
3.3	Previous results for searches of gluino-mediated supersymmetry.	21
4.1	High energy cosmic rays in the atmosphere.	23
4.2	The LHC complex.	23
4.3	The integrated luminosity of CMS over its lifetime.	24
5.1	A diagram of the CMS detector.	26
5.2	A diagram of the CMS detector in the $r\phi$ plane; particle signatures are shown.	27
5.3	A diagram of the CMS detector in the $rz$ plane.	27
5.4	The CMS silicon tracker	28
5.5	The CMS electromagnetic calorimeter	30
5.6	The CMS hadron calorimeter	33
5.7	A simulation of the 4T CMS magnetic field.	34
5.8	The CMS muon drift tube detector.	36
5.9	The CMS muon cathode strip chambers.	37
5.10	The CMS muon resistive plate chamber.	38

7.1	Diagrams of the benchmark models used for motivation of the targeted signal. . . . .	48
7.2	Distributions of the bb-tagging discriminator and jet mass for AK8 jets. . . . .	51
7.3	Generator level distributions for the H bosons in the T5HH model. . . . .	55
7.4	Partitioning of the signal and sideband regions for event binning. . . . .	56
7.5	$p_T^{\text{miss}}$ distributions and predictions in the signal regions using simulation only. . . . .	57
7.6	The fractional composition of expected SM backgrounds in the 6 analysis regions. . .	58
7.7	Comparisons of the predicted and observed yields within the data control regions. .	60
7.8	Signal and sideband yields in the single photon control region. . . . .	62
7.9	Signal and sideband yields in the single lepton control region. . . . .	63
7.10	Signal and sideband yields in the the low- $\Delta\phi$ control region. . . . .	64
7.11	Signal region $p_T^{\text{miss}}$ distributions using scale-factor corrected simulation. . . . .	66
7.12	Control region $p_T^{\text{miss}}$ distributions comparing data and scale-factor corrected simulation.	68
7.13	Pruned jet mass in semi-leptonic $t\bar{t}$ events. . . . .	72
7.14	Observed yields in the signal regions. . . . .	73
7.15	The single event in the $A_2$ region. . . . .	74
7.16	Observed and expected limits on the gluino cross section. . . . .	75
A.1	Efficiencies for an AK8 jet originating from H boson decay, relative to baseline selection.	80
A.2	Efficiencies for an AK8 jet originating from Z boson decay, relative to baseline selection.	81
B.1	A diagram of a semi-leptonic $t\bar{t}$ event in the center-of-mass frame. . . . .	83
B.2	W jet mass and $b\bar{b}$ -tagging discriminator in data and simulation. Simulation is scaled to match the data normalization. . . . .	84

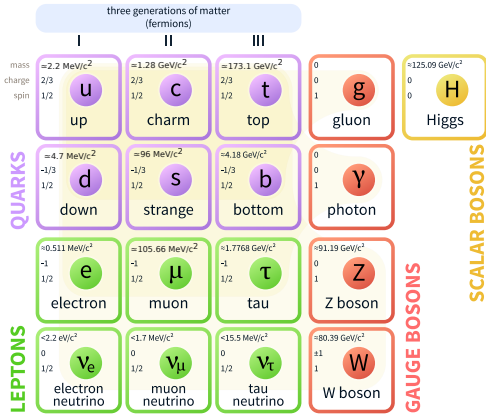
# Chapter 1

## Introduction



(a) The Period Table of the Elements.

### Standard Model of Elementary Particles



(b) The Standard Model of Particle Physics.

The thesis is outlined as follows: A description of the Standard Model (SM) of particle physics is presented in Chapter 2. A description of the Minimal Supersymmetric Standard Model (MSSM) is presented in Chapter 3. A description of the Large Hadron Collider (LHC), the facility which acts as our source of high-energy proton-proton collisions, is presented in Chapter 4. A description of the CMS particle detector, situated to detect the fragments of the proton collisions, is presented in Chapter 5. A description of how the data from the detector are reconstructed and identified as physical particles is presented in Chapter 6. The focus of the thesis, a description of the how the physics data can be used to search for evidence of new particles such as those predicted by SUSY, is presented in Chapter 7. The conclusions are presented in Chapter 8.

## Chapter 2

### The Standard Model of Particle Physics

#### 2.1 Introduction

The Standard Model (SM) is a mathematical framework for the quantum mechanical description of matter and physical forces. It provides a description of the weak, strong, and electromagnetic interactions as mediated via “messenger” particles (gravity has so far eluded a quantum mechanical description). The particles constituting matter can be classified as *quarks* or *leptons* - quarks participate in the weak and strong force, leptons participate in the weak force; any charged particle experiences the electromagnetic force. *Gauge bosons* are the particles responsible for the force interactions. The Higgs field is important for the generation of particle mass. This particle content has been seen in Figure 1.1b, we now turn to the field theory approach for these objects.

Matter particles are massive spin-1/2 fermions which are represented by solutions to the free-particle Dirac equation generated by the following Lagrangian, with equation of motion:

$$\begin{aligned}\mathcal{L} &= i\bar{\psi}\gamma^\mu\partial_\mu\psi - m\bar{\psi}\psi \\ i\gamma^\mu\partial_\mu\psi - m\psi &= 0\end{aligned}\tag{2.1}$$

respectively.

Particle interactions are generated by requiring the free-particle Lagrangian to be invariant under the action of different symmetry groups. Demanding local (gauge) invariance requires one to introduce spin-1 vector fields to the Lagrangian which couple with the fermions. The vector fields are to be identified with the generators of the symmetry group and act as the mediator of

Table 2.1: Summary of field content within the SM.

Gauge Sector	Matter Fields	Gauge Fields
<b>SU(3)</b>	u, d, c, s, t, b	$G_\mu^{1\dots 8} \rightarrow g_\mu^{1\dots 8}$
<b>SU(2) <math>\times</math> U(1)</b>	$Q_L = \begin{pmatrix} u \\ d \end{pmatrix}_L, \begin{pmatrix} s \\ c \end{pmatrix}_L, \begin{pmatrix} t \\ b_L \end{pmatrix}_L$ $q = u, d, c, s, t, b$ $L_L = \begin{pmatrix} \nu_e \\ e^- \end{pmatrix}_L, \begin{pmatrix} \nu_\mu \\ \mu^- \end{pmatrix}_L, \begin{pmatrix} \nu_\tau \\ \tau^- \end{pmatrix}_L$ $\ell = (e, \mu, \tau)$	$W_\mu^{012}, B_\mu^0$ $W_\mu^0, B_\mu^0 \rightarrow Z_\mu^0, A_\mu^0$ $W_\mu^1, W_\mu^2 \rightarrow W_\mu^+, W_\mu^-$
<b>Higgs Sector</b>	$H = \begin{pmatrix} H^+ \\ H^0 \end{pmatrix} \rightarrow h^0$	

the force via particle exchange. U(1) generates electromagnetism via interactions with photons. A combination of U(1) and SU(2) generates the electroweak theory, simultaneously describing the electromagnetic and weak nuclear force via interactions with  $W^\pm$  bosons, Z bosons and photons. SU(3) generates quantum chromodynamics, the theory of the strong nuclear force via interactions with gluons. These massive spin-1 gauge bosons are represented by solutions to the free particle Proca equations generated by the following Lagrangian, with equation motion:

$$\begin{aligned} \mathcal{L} &= -\frac{1}{16\pi} B^{\mu\nu} B_{\mu\nu} + \frac{1}{8\pi} m^2 B_\nu B^\nu \\ \partial^\mu \partial_\mu \psi - m^2 \psi &= 0 \end{aligned} \tag{2.2}$$

where  $B_{\mu\nu} \equiv \partial_\mu B_\nu + \partial_\nu B_\mu$  is known as the *energy-momentum tensor* representing the kinetic energy of the field.

The mathematical fields which are contained with the SM are seen in Table 2.1. This table will serve as a reference for the remainder of the chapter.

## 2.2 Quantum Electrodynamics

Quantum electrodynamics describes the interactions of particles with electric charge. Beginning with a free-particle Dirac fermion we see the Lagrangian is invariant under the following U(1)

transformation:

$$\psi(x) \xrightarrow{U(1)} e^{iq\alpha} \psi(x) \quad (2.3)$$

where  $q$  is the electric charge, and  $\alpha$  is an arbitrary constant.

In light of this symmetry, Noether's theorem implies the existence of a conserved (electromagnetic) current  $j^\mu = -e\bar{\psi}\gamma^\mu\psi$  ( $\partial_\mu j^\mu = 0$ ). If we then allow the  $U(1)$  transformation to be space-time dependent, that is  $\alpha = \alpha(x)$ , we must introduce a new spin-1 vector field  $A^\mu$  in order for the derivative to transform such that the Lagrangian remain invariant. This new field is introduced by making a redefinition of the partial derivative, called the *covariant derivative*, and the following transformation property for the new field:

$$\begin{aligned} \partial_\mu &\rightarrow \partial_\mu - ieA_\mu \\ A_\mu &\xrightarrow{U(1)} A_\mu + \frac{1}{e}\partial_\mu\alpha \end{aligned} \quad (2.4)$$

We then make the substitution into the Lagrangian:

$$\mathcal{L}_{QED} = i\bar{\psi}\gamma^\mu\partial_\mu\psi - e\bar{\psi}\gamma^\mu\psi A_\mu - m\bar{\psi}\psi - \frac{1}{4}F_{\mu\nu}F^{\mu\nu} \quad (2.5)$$

where  $F_{\mu\nu} \equiv \partial_\mu A_\nu - \partial_\nu A_\mu$  is the field strength tensor.

We see that in order for the Lagrangian to remain invariant under this  $U(1)$  transformation, we were forced to introduce an additional term which links the conserved electromagnetic current with the spin-1 field:  $e\bar{\psi}\gamma^\mu\psi A_\mu = j^\mu A_\mu$ . This new field is to be identified with the photon, it acts as a mediator of the force between two particles with electric charge. A photon mass term of the form  $\frac{1}{2}m^2 A^\mu A_\mu$  is forbidden as it is not invariant under the transformation rule, the photon remains massless.

### 2.3 Quantum Chromodynamics

Quantum chromodynamics describes the interactions of quarks due to the strong nuclear force. The theory is generated by demanding local invariance of the Lagrangian under an  $SU(3)$

symmetry operating on *color triplets*. Eight new gauge fields must be introduced to give the proper transformation rule of the covariant derivative. These new gauge fields become the gluons and act as the mediator of the strong force, mixing the color states within a quark.

Consider the following SU(3) transformation:

$$q_c \xrightarrow{\text{SU}(3)} e^{\frac{1}{2}ig_s\boldsymbol{\xi}(x)\cdot\boldsymbol{\lambda}} q_c \quad (2.6)$$

where  $g_s$  is the strong coupling constant,  $\boldsymbol{\xi}$  is an 8-dimensional vector of arbitrary functions of spacetime,  $\boldsymbol{\lambda}$  are the 8 3x3 Gell-Mann matrices, and  $\bar{q}_c = (\bar{q}_{red}, \bar{q}_{green}, \bar{q}_{blue})$  is a color-triplet such that  $q(x) = q_c q_D(x)$  and  $q_D(x)$  is a Dirac fermion (any of the 6 SM quarks).

SU(3) gauge invariance requires us to modify the definition of the partial derivative to include 8 spin-1 vector fields  $\mathbf{G}_\mu$ :

$$\begin{aligned} \partial_\mu &\rightarrow \partial_\mu - ig_s \boldsymbol{\lambda} \cdot \mathbf{G}_\mu \\ G_\mu^k &\xrightarrow{\text{SU}(3)} G_\mu^k - \frac{1}{g_s} \partial_\mu \xi_k - f_{ijk} \xi_i G_\mu^j \end{aligned} \quad (2.7)$$

where  $f_{ijk}$  are known as the *structure constants* of SU(3) and arise from its non-abelian nature, they satisfy  $[\lambda_i, \lambda_j] = 2if_{ijk}\lambda_k$ .

The complete Lagrangian becomes:

$$\mathcal{L}_{\text{QCD}} = i\bar{q}\gamma^\mu \partial_\mu q - \frac{1}{2}(g_s \bar{q}\gamma^\mu \boldsymbol{\lambda} q) \cdot \mathbf{G}_\mu - m\bar{q}q - \frac{1}{4}\mathbf{G}^{\mu\nu} \cdot \mathbf{G}_{\mu\nu} \quad (2.8)$$

where  $G_i^{\mu\nu} \equiv \partial^\mu G_i^\nu - \partial^\nu G_i^\mu - g_s f_{ijk} G_j^\mu G_k^\nu$  is the field strength tensor for the gluon field  $i$ .

We see the non-abelian nature of SU(3) manifests itself as self-couplings within the gluon field, giving rise to interaction vertices with 3 or 4 gluons. 8 conserved color currents, analogous to the electromagnetic current, are seen as interaction terms between two quarks and a gluon ( $\frac{1}{2}g_s \bar{q}\gamma^\mu \boldsymbol{\lambda} q \cdot \mathbf{G}_\mu = j^\mu \cdot \mathbf{G}_\mu$ ).

$$\mathbf{G}_\mu = \mathbf{j}^\mu \cdot \mathbf{G}_\mu.$$

To conserve color charge at the QCD vertices, gluons themselves must carry both color and anti-color. The color charge allows for self interactions of the gluons (contrast with the to the elec. The 8 physical gluons are members of a color/anticolor octet. 6 of them are expressed as ladder operators within SU(3) and the other two are diagonal matrices.

A gluon mass term of the form  $\frac{1}{2}m^2\mathbf{G}^\mu \cdot \mathbf{G}_\mu$  is forbidden as it is not invariant under the transformation rule, the gluons remain massless.

### 2.3.1 Confinement, Hadrons, & the Quark Model

Experimentally we have never detected a free quark. The physical manifestation of quark production results in a final state consisting of many lower energy particles produced collinear with the original quark. This “spray” of particles is known as a *jet*. This behavior can be explained if one accepts the hypothesis of *color confinement* stating that all objects with color charge are confined to colorless singlets. The origins of color confinement may be traced to the self interactions of the gluon fields resulting in the strong force between two quarks to **increase** as they separate. It eventually becomes energetically favorable to create quark-antiquark pairs from the vacuum which can subsequently combine with other quarks to form the colorless objects (constituting the jets).

*Hadrons* are bound states of quarks which interact through the strong force. Color confinement limits the possible combinations of quarks and antiquarks which can exist together in a bound state (antiquarks carry anticolor). Among states consisting of two quarks+antiquarks, the only possible color singlet wave function is a  $q\bar{q}$  pair:  $\psi = \frac{1}{\sqrt{3}}(r\bar{r} + g\bar{g} + b\bar{b})$  - these states are called *mesons*. For systems of three quarks+antiquarks, the only color singlet consists of three quarks  $qqq$ :  $\psi = \frac{1}{\sqrt{6}}(rgb - rbg + gbr - grb + brg - bgr)$  - these states are called *baryons*.

The strength of the strong force between two quarks is independent of their flavor and therefore QCD possesses a symmetry under rotations in flavor-space. This would be an exact symmetry if it were not for the physical quark masses (Figure 1.1b). To a crude approximation the  $u$ ,  $d$ , and  $s$  quarks have the same mass: 2.2, 4.7, and 96 MeV, (compare to the  $c$  with a mass of 1.28 GeV). The  $uds$  quarks can therefore be thought of as different states within a triplet. This is known as the *SU(3) flavor symmetry*. Within the symmetry, the  $q\bar{q}$  meson states can be combined to form two nonets with angular momentum  $l = 0$ , and spins of  $s = 0$  or  $s = 1$ . The  $s = 0$  states are the lowest energy and provide a quark description of the kaons and pions. The  $qqq$  baryons can form flavor states consisting of a  $j = 1/2$  octet and  $j = 3/2$  decuplet. The  $j = 1/2$  states are the lowest

energy and describe the proton and neutron. These multiplet structures can be seen in Figure 2.1.

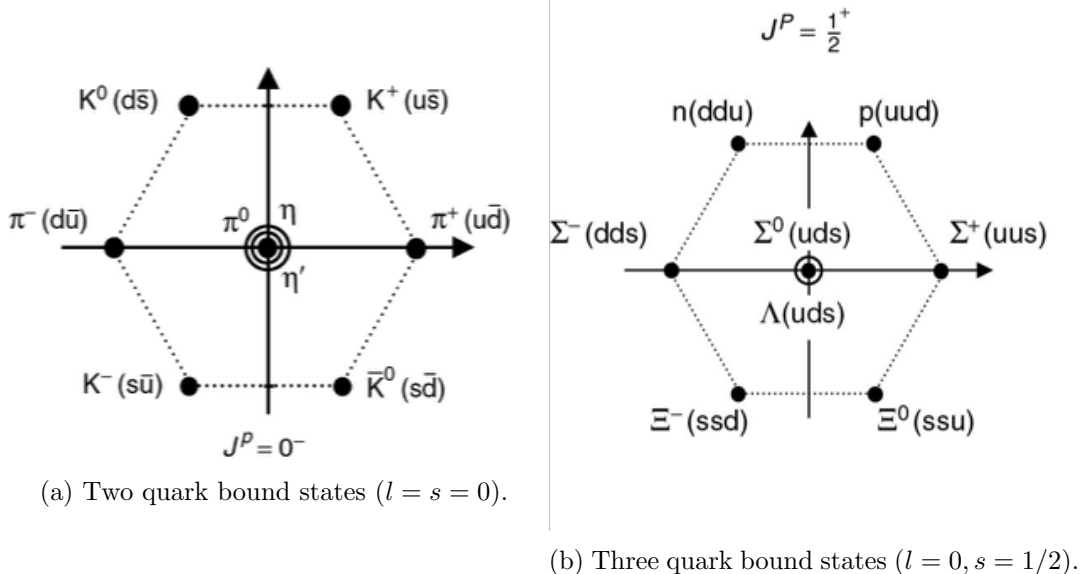


Figure 2.1: SU(3) flavor symmetry multiplets predicted by the quark model.

## 2.4 Electroweak Theory

### 2.4.1 Introduction

The electroweak theory provides a unified and self-consistent description of both the electromagnetic and weak forces. The complete theory is generated by demanding local invariance of the Lagrangian under a combined  $SU(2) \times U(1)$  symmetry. The  $SU(2)$  invariance requires the addition of three new vector bosons, two of which are used to construct the physical  $W^\pm$  bosons responsible for the weak *charged current* interactions. An additional gauge boson is required for the  $U(1)$  symmetry. A mixing between the remaining (neutral)  $SU(2)$  gauge field and the  $U(1)$  gauge field yield the  $Z$  boson and photon, responsible for weak *neutral current* and electromagnetic interactions, respectively.

Consider the following  $U(1)$  transformation on a fermion  $\psi$ , and  $SU(2)$  transformation on an

*isospin doublet*  $\Psi$ :

$$\begin{aligned}\psi(x) &\xrightarrow{\text{U}(1)} e^{ig'\frac{Y}{2}\alpha(x)} \psi(x) \\ \Psi(x) &\xrightarrow{\text{SU}(2)} e^{ig_W\xi(x)\cdot\frac{1}{2}\boldsymbol{\sigma}} \Psi(x)\end{aligned}\tag{2.9}$$

where  $g'$  is the hypercharge coupling constant,  $Y$  is the hypercharge operator,  $g_W$  is the weak coupling constant,  $\alpha$  and  $\xi$  are arbitrary functions of spacetime, and  $\boldsymbol{\sigma}$  represents the 3 2x2 Pauli spin matrices.

As usual, SU(2) and U(1) gauge-invariance requires us to modify the definition of the partial derivative to include three spin-1 vector fields  $\mathbf{W}^\mu$  and a single spin-1 vector field  $B^\mu$ :

$$\begin{aligned}\partial_\mu &\rightarrow \partial_\mu - ig'\frac{Y}{2}B_\mu - ig_W\frac{1}{2}\boldsymbol{\sigma} \cdot \mathbf{W}_\mu \\ B_\mu &\xrightarrow{\text{U}(1)} B_\mu - ig'\partial_\mu\alpha \\ \mathbf{W}_\mu^k &\xrightarrow{\text{SU}(2)} \mathbf{W}_\mu^k - g_W\partial_\mu\xi^k - g_W\epsilon_{ijk}\xi^i\mathbf{W}_\mu^j\end{aligned}\tag{2.10}$$

where  $\epsilon_{ijk}$  is the totally antisymmetric Levi-Civita tensor (the structure constants of SU(2)).

The charged current interaction connects two elements within an isospin doublet  $\Psi$ ; by convention, the upper element has electric charge +1 relative to the lower element. There are doublets which connect the leptons with a corresponding neutrino (massless spin-1/2 particles), and there are doublets which connect an 'up-type' quark (top entry of the doublet) to a 'down-type' quark (bottom entry):

$$\begin{pmatrix} \nu_e \\ e^- \end{pmatrix}, \begin{pmatrix} \nu_\mu \\ \mu^- \end{pmatrix}, \begin{pmatrix} \nu_\tau \\ \tau^- \end{pmatrix}, \begin{pmatrix} u \\ d' \end{pmatrix}, \begin{pmatrix} c \\ s' \end{pmatrix}, \begin{pmatrix} t \\ b' \end{pmatrix}$$

The  $W^1$  and  $W^2$  gauge fields correspond to the first two Pauli matrices; appropriate linear combinations of these two fields therefore define raising and lowering operators which transform elements within a doublet. The physical  $W^\pm$  bosons are the following linear combinations of the two gauge fields:

$$W_\mu^\pm = \frac{1}{\sqrt{2}}(W_\mu^1 \mp iW_\mu^2)\tag{2.11}$$

As Nature has it, the weak force is a *chiral* theory which does not treat the left and right-chiral components of a Dirac fermion on equal footings. The projection operator  $P_{R/L} = \frac{1}{2}(1 \pm \gamma^5)$  is used to define these left and right chiral states, all Dirac fermions can be decomposed as  $\psi = \psi_L + \psi_R$  using these operators. In the Standard Model, only left-handed particle and right-handed antiparticle states enter into the isospin doublets participating in the electrically-charged weak interaction. This is summarized in Table 2.1.

Because of the SU(2) symmetry and doublet nature, we must introduce **two** fermions to the theory, where the left and right chiral components may transform differently under gauge interactions. Consider fields  $\chi$  and  $\tau$ ; the left handed components are members of an isospin doublet  $\overline{\psi_L} = (\overline{\chi_L}, \overline{\tau_L})$ , all components participate in the U(1) transformation. The complete Lagrangian becomes:

$$\begin{aligned}\mathcal{L}_{\text{EWK}} = & i\bar{\chi}\gamma^\mu\partial_\mu\chi - m\bar{\chi}\chi + i\bar{\tau}\gamma^\mu\partial_\mu\tau - m\bar{\tau}\tau - \frac{1}{4}B_{\mu\nu}B^{\mu\nu} - \frac{1}{4}\mathbf{W}_{\mu\nu}\cdot\mathbf{W}^{\mu\nu} \\ & - g'\bar{\chi}\gamma^\mu\frac{Y}{2}\chi B_\mu + g'\bar{\tau}\gamma^\mu\frac{Y}{2}\tau B_\mu - g_W\overline{\psi_L}\gamma^\mu\boldsymbol{\sigma}\psi_L\cdot\mathbf{W}_\mu\end{aligned}\quad (2.12)$$

Mass terms of the form  $\frac{1}{2}m^2A^\mu A_\mu$  are forbidden as they are not invariant under the transformation rule, the  $B$  and  $\mathbf{W}$  bosons remain massless.

#### 2.4.2 The Higgs Mechanism

The gauge bosons responsible for the electroweak force have observationally been determined to have mass, which is a problem as the gauge symmetry requires them to be massless. Surely there must be some mechanism which can be introduced to achieve this meanwhile (at least initially) preserving the  $SU(2)\times U(1)$  symmetry. The *Higgs field* is introduced to generate mass terms for the electroweak gauge bosons. The discovery of the Higgs boson was the final particle contained within the SM to be observed, its discovery in 2012 was monumental.[1]

This Higgs mechanism proceeds by introducing a massive spin-0 complex scalar field with the following Lagrangian:

$$\mathcal{L} = \frac{1}{2}(\partial_\mu\phi^\dagger)(\partial^\mu\phi) - \frac{1}{2}\mu^2\phi^\dagger\phi + \lambda(\phi^\dagger\phi)^2\quad (2.13)$$

where  $\mu$  and  $\lambda$  are the strengths of the self-coupling terms.

Within the SM, the field is implemented as an isospin doublet which consists of electrically neutral and charged components:

$$\phi = \begin{pmatrix} \phi^+ \\ \phi^0 \end{pmatrix} = \begin{pmatrix} \phi_1 + i\phi_2 \\ \phi_3 + i\phi_4 \end{pmatrix}, \quad (2.14)$$

Solving for the minimum of the potential, it is found that the ground state of  $\phi$  is non-zero and satisfies  $\phi^\dagger \phi = \phi_1^2 + \phi_2^2 + \phi_3^2 + \phi_4^2 = \frac{1}{2}v^2 = -\mu^2/2\lambda$ . This is called *spontaneous symmetry breaking* - the Higgs acquiring a *vacuum expectation value*. Perturbation theory of interactions represent particles as fluctuations above the vacuum - we must express the fields in the same manner. Electric charge conservation requires that this vacuum expectation value lie entirely inside the neutral  $\phi^0$ . This ground state is then expressed as:

$$\phi = \begin{pmatrix} 0 \\ v + h(x) \end{pmatrix}, \quad (2.15)$$

where  $h(x)$  is to be identified as the Higgs boson.

If we substitute the ground-state expansion of  $\phi$  to the Lagrangian of Equation 2.13 we obtain the following expression:

$$\mathcal{L} = \frac{1}{2}(\partial^\mu h)(\partial_\mu h) - \lambda v^2 h^2 - \lambda v h^3 - \frac{1}{4}\lambda h^4 + \lambda v^4 \quad (2.16)$$

where we see have generated a mass term  $m_h = \sqrt{2\lambda}v$  for the Higgs boson, additionally there are now 3 and 4-point Higgs self-couplings.

#### 2.4.2.1 Masses of the $W^\pm$ and $Z$ bosons

The kinetic energy term  $\frac{1}{2}(\partial_\mu \phi^\dagger)(\partial^\mu \phi)$  for the Higgs field introduces a coupling with the  $\mathbf{W}^\mu$  and  $\mathbf{B}^\mu$  bosons when they are added to the covariant derivative:

$$\partial_\mu \phi = \left( \frac{1}{2}\partial_\mu + \frac{1}{2}ig_W \boldsymbol{\sigma} \cdot \mathbf{W} + ig' \frac{Y}{2} \mathbf{B}^\mu \right) \begin{pmatrix} 0 \\ v + h(x) \end{pmatrix} \quad (2.17)$$

After performing the matrix calculations, and lots of algebra, there are terms quadratic in the gauge fields:

$$\frac{1}{8}v^2g_W^2(W_\mu^1W_1^\mu + W_\mu^2W_2^\mu) + \frac{1}{8}v^2(g_WW_\mu^3 - g'B_\mu)(g_WW_3^\mu - g'B^\mu) \quad (2.18)$$

Where we see we have generated mass terms for the  $W_1^\mu$  and  $W_2^\mu$  fields:  $m_W = \frac{1}{2}vg_W$ . The last term in the expansion introduces mixed couplings between the electrically neutral and massless  $W_3^\mu$  and  $B^\mu$  fields. The mixing can be represented via a non-diagonal mass matrix. Physical particles propagate as independent eigenstates of the free particle Hamiltonian and therefore we must find the basis in which this matrix is diagonal. Upon diagonalization, we find the states corresponding to these eigenvalues:

$$\begin{aligned} A_\mu &= \frac{1}{\sqrt{g_W^2 + g'^2}}(g'W_\mu^3 + g_WB_\mu); & \text{with mass } 0 \\ Z_\mu &= \frac{1}{\sqrt{g_W^2 + g'^2}}(g_WW_\mu^3 - g'B_\mu); & \text{with mass } \frac{1}{2}v\sqrt{g_W^2 + g'^2} \end{aligned} \quad (2.19)$$

where  $A_\mu$  corresponds to the photon of electromagnetism, and  $Z_\mu$  the neutral gauge boson responsible for the weak neutral currents.

We have seen how the Higgs mechanism is able to generate mass terms for the gauge bosons in the electroweak theory.

#### 2.4.2.2 Masses of the Fermions

It has not been mentioned that the fermion mass terms  $-m\bar{\psi}\psi = -m(\overline{\psi_R}\psi_L + \overline{\psi_L}\psi_R)$  are in fact forbidden within the SM - the chiral nature of SU(2) treats the two chiral states differently and therefore this term is not invariant under the transformation rules. Masses for the fermions are created by introducing *Yukawa interactions* with the Higgs field. Consider the following terms which are invariant under the  $U(1) \times SU(2)$  transformation:

$$\begin{aligned} \mathcal{L} &= -y[\overline{\psi_L}\phi\psi_R + \overline{\psi_R}\phi^\dagger\psi_L] \\ &= -y \left[ \begin{pmatrix} \bar{\nu}, \bar{\ell} \end{pmatrix}_L \begin{pmatrix} \phi^+ \\ \phi^0 \end{pmatrix} \ell_R + \overline{\ell_R} \begin{pmatrix} \phi^{+*}, \phi^{0*} \end{pmatrix} \begin{pmatrix} \nu \\ \ell \end{pmatrix}_L \right] \end{aligned} \quad (2.20)$$

where  $y$  is the *Yukawa coupling*,  $\overline{\psi}_L$  is an isospin doublet of left-chiral fermions, and  $\psi_R$  is a right-chiral fermion.

After spontaneous symmetry breaking, this reduces to:

$$\begin{aligned}\mathcal{L} &= -\frac{1}{\sqrt{2}}yv(\overline{\ell}_L\ell_R + \overline{\ell}_R\ell_L) - \frac{1}{\sqrt{2}}yh(\overline{\ell}_L\ell_R + \overline{\ell}_R\ell_L) \\ &= -\frac{1}{\sqrt{2}}yv\bar{\ell}\ell - \frac{1}{\sqrt{2}}yh\bar{\ell}\ell\end{aligned}\tag{2.21}$$

and we see we have obtained a mass term for the fermion  $m_\ell = \frac{1}{\sqrt{2}}yv$  and an interaction term  $\frac{1}{\sqrt{2}}yh\bar{\ell}\ell$  between the fermion in the lower member of the isospin doublet and a single Higgs boson.

To generate a mass term for the upper component of the isospin doublet we need to follow the same prescription but with the *conjugate* Higgs field:

$$\phi_c = -i\sigma_2\phi^* = \begin{pmatrix} -\phi^{0*} \\ \phi^- \end{pmatrix} = \frac{1}{\sqrt{2}} \begin{pmatrix} -\phi_3 + i\phi_4 \\ \phi_1 - i\phi_2 \end{pmatrix},\tag{2.22}$$

where the same story plays out.

#### 2.4.3 Quark Mixing - the CKM Matrix

The charged weak current acts on isospin doublets connecting quarks of different flavors - the flavor eigenstates: u, d, s, c, b, t. The quarks propagate as mass eigenstates of the free-particle Hamiltonian. This introduces mixing between these two bases and is represented by the *CKM matrix*. The probability of a transition between two states is proportional to a matrix element  $|V|^2$  in the matrix. It is unitary 3x3 matrix with 4 degrees of freedom:

$$\begin{pmatrix} d' \\ s' \\ b' \end{pmatrix} = \begin{pmatrix} V_{ud} & V_{us} & V_{ub} \\ V_{cd} & V_{cs} & V_{cb} \\ V_{td} & V_{ts} & V_{tb} \end{pmatrix} \begin{pmatrix} d \\ s \\ b \end{pmatrix}\tag{2.23}$$

The best estimate of these parameters are:

$$\begin{pmatrix} |V_{ud}| & |V_{us}| & |V_{ub}| \\ |V_{cd}| & |V_{cs}| & |V_{cb}| \\ |V_{td}| & |V_{ts}| & |V_{tb}| \end{pmatrix} \approx \begin{pmatrix} 0.974 & 0.225 & 0.004 \\ 0.225 & 0.973 & 0.041 \\ 0.009 & 0.040 & 0.999 \end{pmatrix} \quad (2.24)$$

#### 2.4.4 Brief Electroweak Summary

We started with a theory of two fields each governed by the Dirac equation. We demanded that the theory be gauge-invariant under combined  $U(1) \times SU(2)$  symmetry operations. The gauge bosons are required to be massless as their transformation rules do not allow their kinetic energy term to be invariant. The Higgs field was introduced, the action of the covariant derivative on the Higgs field generates an interaction term between the gauge bosons and the Higgs field. The Higgs field obtained a vacuum expectation value, re-expressing the field about this ground state led us to mass terms for the gauge bosons. The physical  $W^\pm$ ,  $Z$ , and  $A$  bosons become mixtures of these states. Fermion mass terms are not initially allowed as the chiral  $SU(2)$  symmetry treats the left and right-chiral components differently and therefore can not remain invariant. Fermion mass terms are generated by introducing Yukawa interactions between the Higgs field and fermions which generate appropriate mass terms after the Higgs field expansion. In addition, under the charged-current interaction, quark flavor and mass eigenstates are not the same, this introduces the CKM matrix parametrizing the mixing.

### 2.5 Parameters of the Standard Model

There are 18 parameters that must be specified as an input to the SM - these must all be determined experimentally:

- 9 quark and lepton masses:  $m_u, m_d, m_s, m_c, m_b, m_t, m_e, m_\mu, m_\tau$ ; the values are listed in Figure 1.1b. (Alternatively these can be expressed as the 9 appropriate Yukawa couplings  $y_f = \sqrt{2}m_f/v$ : 1, 1, 1, 1, 1, 1, 1, 1, 1 respectively)

- 4 parameters describing the mixing between quark mass and flavor eigenstates (CKM matrix, see Equations 2.23 and 2.24): often parametrized as  $\lambda, A, \rho, \eta$
- 2 parameters for the Higgs field: mass and vacuum expectation value  $m_H = 125$  GeV,  $v = 246$  GeV
- 3 coupling constants for the relative strengths of the gauge group:

$$\begin{aligned}\alpha &\equiv e^2/4\pi, & \alpha(q^2 \approx 0) &= 1/137.0 \\ && \alpha(q^2 = (193 \text{ GeV})^2) &= 1/(127.4 \pm 2.1) \\ \alpha_s &\equiv g_s^2/4\pi, & \alpha_s(q^2 = m_Z^2 = (91 \text{ GeV})^2) &= 0.1184 \pm 0.0007 \\ G_F &\equiv \sqrt{2}g_W^2/8m_W^2, & G_F(q^2 \approx 0) &= 1.1663787 \times 10^{-5}\end{aligned}$$

## 2.6 Neutrino Mass

Within the 'canonical' SM the neutrinos are assumed to be massless spin-1/2 fermions. In the last decade, experiments have shown that neutrinos go through *flavor oscillations* wherein they change flavor as they propagate through space. This flavor oscillation is dependent on **massive** neutrinos and can be described by a mixing between these mass and flavor eigenstates. The mixing is described by a 3x3 unitary matrix known as the *PMNS matrix* (analogous to the CKM matrix). One could consider giving the neutrinos a Yukawa coupling with the Higgs and give them a Dirac mass  $-m\bar{\nu}\nu = -m(\bar{\nu}_R\nu_L + \bar{\nu}_L\nu_R)$ , but the non-observation of right-handed neutrinos does not allow that approach. The correct implementation of the neutrino mass is still an open question in the field. The currently known estimates for their masses are seen in Figure 1.1b.

The neutrino mass sector possibly adds an additional 7 parameters to the SM:

- 3 neutrino masses:  $m_{\nu_1}, m_{\nu_2}, m_{\nu_3}$
- 4 parameters describing the mixing between the neutrino mass and flavor eigenstates (PMNS matrix): often parameterized as  $\theta_{12}, \theta_{13}, \theta_{23}, \delta$ .

The best fit values of the PMNS matrix are:

$$\begin{pmatrix} |U_{e1}| & |U_{e2}| & |U_{e3}| \\ |U_{\mu 1}| & |U_{\mu 2}| & |U_{\mu 3}| \\ |U_{\tau 1}| & |U_{\tau 2}| & |U_{\tau 3}| \end{pmatrix} \approx \begin{pmatrix} 0.85 & 0.50 & 0.17 \\ 0.35 & 0.60 & 0.70 \\ 0.009 & 0.35 & 0.70 \end{pmatrix} \quad (2.25)$$

## Chapter 3

### The Minimal Supersymmetric Model

In addition to the  $SU(3) \times SU(2) \times U(1)$  symmetry imposed on the Lagrangian within the Standard Model, one can introduce additional *supersymmetries* to the theory. Supersymmetry transformations act on fields containing both fermionic and bosonic degrees of freedom, the Lagrangian is required to remain invariant under rotations between these two states. Many such extensions to the Standard Model exist, but only the simplest of these, requiring a single global transformation  $Q$  is phenomenologically viable: the Minimal Supersymmetric Standard Model (MSSM).

Within the MSSM, every SM particle has a *superpartner* which differs by  $1/2$  unit of spin but otherwise has identical properties. For example, the electron is paired with an electrically charged, massive, spin-0 scalar field, called a “selectron”.

A striking prediction of the MSSM is more than a doubling of the known particle content of the Universe. In addition to the single SM Higgs doublet, the MSSM requires another spin-0 Higgs isospin doublet, with opposite hypercharge. These two spin-0 doublets each have their own chiral superpartner. Table 3.1 lists the fields required within the MSSM (the sort of complement of Table 2.1). As the nature of the newly supersymmetric electroweak sector is unknown, the various components of the fields may mix. The charged components from the new  $SU(2)$  fields and the Higgs summarized in Table 3.2 (color charge prevents gluinos from mixing outside QCD). This chapter is adapted from [2].

Matter particles (both the left and right-chiral components separately) are placed in *chiral supermultiplets* consisting of a spin- $1/2$  Majorana fermion  $\psi$  and complex scalar field  $\phi$ . In the

Table 3.1: Summary of the additional particle content within the MSSM.

<b>SM Gauge Sector</b>	sfermions	gauginos
SU(3)	$\tilde{u}, \tilde{d}, \tilde{c}, \tilde{s}, \tilde{t}, \tilde{b}$	$\tilde{g}_{1\dots 8}$
SU(2) $\times$ U(1)	$\tilde{Q}_L = \begin{pmatrix} \tilde{u} \\ \tilde{d} \end{pmatrix}_L, \begin{pmatrix} \tilde{s} \\ \tilde{c} \end{pmatrix}_L, \begin{pmatrix} \tilde{t} \\ \tilde{b} \end{pmatrix}_L$ $\tilde{q} = \tilde{u}, \tilde{d}, \tilde{c}, \tilde{s}, \tilde{t}, \tilde{b}$ $\tilde{L}_L = \begin{pmatrix} \tilde{\nu}_e \\ \tilde{e}^- \end{pmatrix}_L, \begin{pmatrix} \tilde{\nu}_\mu \\ \tilde{\mu}^- \end{pmatrix}_L, \begin{pmatrix} \tilde{\nu}_\tau \\ \tilde{\tau}^- \end{pmatrix}_L$ $\tilde{\ell} = (\tilde{e}, \tilde{\mu}, \tilde{\tau})$	$\widetilde{W}_{012}, \widetilde{B}_0$
<b>Higgs Sector</b>	$H_u = \begin{pmatrix} H_u^+ \\ H_u^0 \end{pmatrix}, H_d = \begin{pmatrix} H_d^0 \\ H_d^- \end{pmatrix}$	$\begin{matrix} \text{spin-0} & \text{spin-1/2} \end{matrix}$ $\widetilde{H}_u = \begin{pmatrix} \widetilde{H}_u^+ \\ \widetilde{H}_u^0 \end{pmatrix}, \widetilde{H}_d = \begin{pmatrix} \widetilde{H}_d^0 \\ \widetilde{H}_d^- \end{pmatrix}$

Table 3.2: Mixing of the supersymmetric electroweak fields.

label 1	label 2
item 1	item 2

massless and non-interacting case (i.e. just the two kinetic terms in the Lagrangian, known as the *Wess-Zumino model* [3]), the transformation laws of the fields can be deduced by demanding invariance under the simple Lagrangian, they are found to be:

$$\begin{aligned}\phi &\xrightarrow{Q} \phi + \epsilon\psi \\ \psi &\xrightarrow{Q} \psi - i(\sigma^\mu\epsilon^\dagger)\partial_\mu\phi\end{aligned}\tag{3.1}$$

where  $\epsilon$  is a 2-component Weyl **spinor** parametrizing the transformation. For the duration of this chapter, all references to *auxiliary* fields will be omitted. Auxiliary fields are internal to the theory and must be introduced to allow the fields to satisfy their classical wave equations.

The requirement of renormalizability restricts the numbers of fields in any interaction involving  $\psi$  and  $\phi$ , the most generic Lagrangian for a chiral supermultiplet is of the form:

$$\mathcal{L}_{chiral} = -D^\mu\phi^*D\mu\phi - V(\phi, \phi^*) + i\psi^\dagger\bar{\sigma}^\mu D\mu\psi - \frac{1}{2}(M\psi\psi + h.c.) - \frac{1}{2}(y\phi\psi\psi + h.c.)\tag{3.2}$$

where  $D^\mu$  is the covariant derivative,  $V(\phi, \phi^*)$  is a scalar potential for the theory,  $\bar{\sigma}^0$  is the 2x2 identity matrix and  $\bar{\sigma}^{123} \equiv -\sigma^{123}$ ,  $M$  is a (Majorana) mass term,  $\psi\psi \equiv \epsilon^{ab}\psi_a\psi_b$ , and  $y$  is a Yukawa coupling. The Yukawa coupling connects two SM fermions with the corresponding supersymmetric scalar field - a vertex diagram for this process is seen in Figure 3.1(a). The covariant derivative  $\partial_\mu\phi \rightarrow \partial_\mu\phi - igA_\mu^aT^a\phi$ , when introduced in the kinetic term, creates two interactions between the SM gauge bosons and the new supersymmetric scalar field:  $-ig[(\partial_\mu\phi)A_\mu^aT^a\phi + h.c.]$  and  $g^2A^{a\mu}\phi^*t^aA_\mu^aT^a\phi$ , seen in Figures 3.1d,e, respectively. Throughout this chapter I will only discuss interactions involving at least one SM particle and at least one supersymmetric particle.

Gauge bosons (before spontaneous symmetry breaking) are placed in *gauge supermultiplets* consisting of gauge bosons  $A_\mu^a$  and spin-1/2 gauginos  $\lambda^a$ ;  $a$  is a label which runs over the SM gauge fields within the theory. Under the supersymmetry, fields can be found to transform as:

$$\begin{aligned}A_\mu^a &\xrightarrow{Q} A_\mu^a - \frac{1}{\sqrt{2}}(\epsilon^\dagger\bar{\sigma}_\mu\lambda + h.c) \\ \lambda_\alpha^a &\xrightarrow{Q} \lambda_\alpha + \frac{i}{2\sqrt{2}}(\sigma^\mu\bar{\sigma}^\nu\epsilon)F_{\mu\nu}^a\end{aligned}\tag{3.3}$$

where  $F_{\mu\nu}^a$  is the regular field strength tensor for the gauge field  $A_\mu^a$ . The SM symmetries (i.e. SU(3), SU(2), U(1)) transform the gauge supermultiplet in the following way:

$$\begin{aligned} A_\mu^a &\xrightarrow{\text{SM}} A_\mu^a + \partial_\mu \Lambda^a + g f^{ijk} A_\mu^b \Lambda^c \\ \lambda^a &\xrightarrow{\text{SM}} \lambda^a + g f^{abc} \lambda^b \Lambda^c \end{aligned} \quad (3.4)$$

where  $\Lambda^a$  is a parameter describing the transformation. (The transformation law for  $A^\mu$  is the same we have seen in Chapter 2.)

The Lagrangian for a free gauge multiplet consists simply of the kinetic terms for each field  $A_\mu^a$  and  $\lambda^a$ :

$$\mathcal{L}_{gauge} = -\frac{1}{4} F_{\mu\nu} F^{\mu\nu} + i \lambda^\dagger \bar{\sigma}^\mu \nabla^\mu \lambda^a \quad (3.5)$$

where  $f^{abc}$  are the structure constants of the gauge group.  $\nabla^\mu \lambda^a = \partial^\mu \lambda^a + g f^{abc} A_\mu^b \lambda^c$  represents the covariant derivative acting on  $\lambda^a$  - creating an interaction term between a gauge boson and two gauginos:  $i g \lambda^\dagger \bar{\sigma}^\mu f^{abc} A_\mu^b \lambda^c$ , as seen in Figure 3.1c.

The requirement of renormalization restricts the interactions between the gauge and chiral supermultiplets to be only of the form  $-\sqrt{2}g(\phi^* T^a \psi \lambda^a + h.c.)$ , involving a single spin-0, spin-1/2, and spin-1 particle - a vertex diagram is seen in Figure 3.1e.

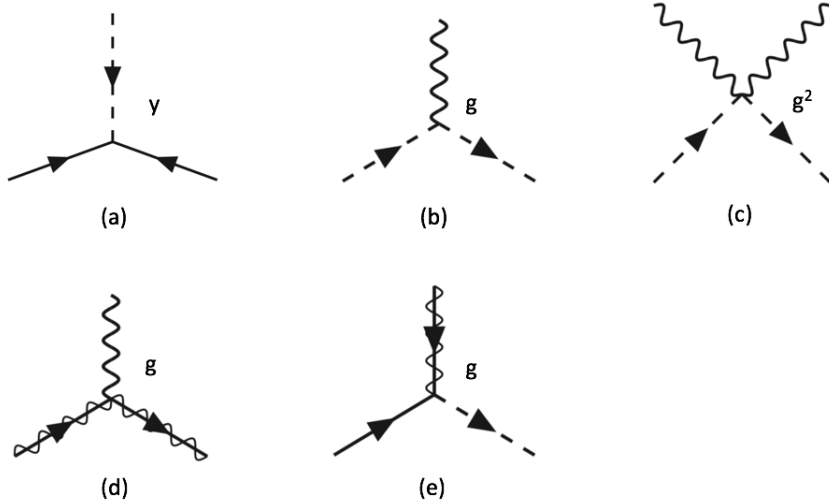


Figure 3.1: Interactions between SM and MSSM particles.  $y$  is a Yukawa coupling to be determined,  $g$  is the SM gauge coupling.

Within a supersymmetric theory, the superpartners are required to have the same mass as their corresponding SM field. If SUSY were exact, we would have expected to see evidence of sparticles over the years. There must be some mechanism which generates large mass for the sparticles such that their production is highly suppressed at our colliders. The remainder of this thesis presents a search for evidence of physics beyond the SM, such as the MSSM. Our motivation is taken from final state topologies arising from gluino pair production - possible mechanisms seen in Figure 3.2. The gluino is the spin-1/2 fermion which is the superpartner to the gluon, the mediator of the strong force. Within the context of QCD - the chiral supermultiplets consist of spin-1/2 quarks and spin-0 squarks. Searches for supersymmetric particles of QCD are partly motivated by the fact that most of their production mechanisms proceed through diagrams proportional to the strong coupling constant  $g_s$ , which is largest among the three in the SM. The supersymmetric partners of QCD necessarily carry color charge, and therefore the QCD squarks and gluinos do not directly interact with other MSSM particles. There have been many searches for SUSY which provide lower limits on the mass of the gluino, such as [4, 5], and its current limit is at about 2 TeV. Figure 3.3 summarizes the results of one of these searches, excluding gluinos below 1.8 TeV given assumptions about the decay (seen in the diagram below the plot). The blob in the diagrams below the limit plots indicates we are not interested in the particular production mechanism, but in the decay chain.

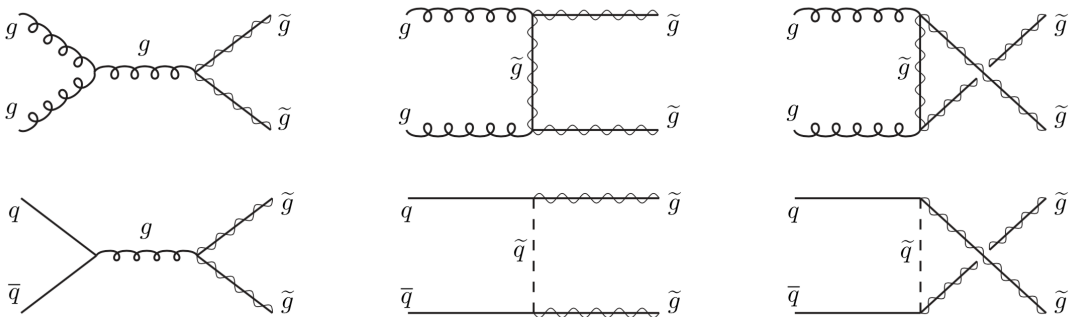


Figure 3.2: Tree-level gluino pair-production mechanisms.

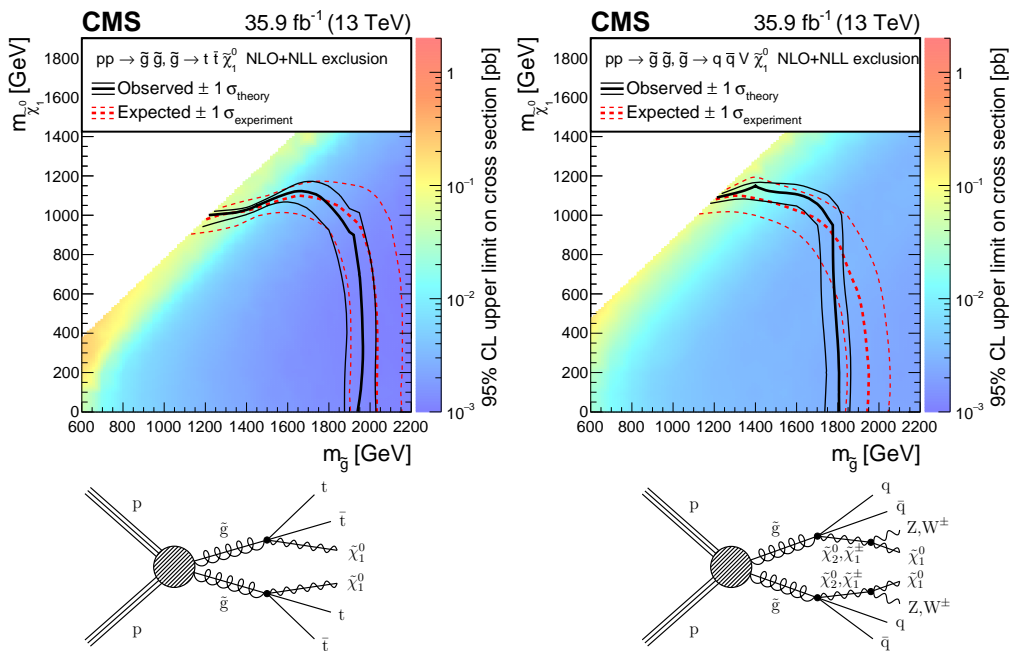


Figure 3.3: Previous results for searches of gluino-mediated supersymmetry for two the T1tttt (left) and T1qqqqVV models [4]. The excluded regions are towards the lower left.

## Chapter 4

### The Large Hadron Collider

Nature itself has provided us with a source of high-energy particle collisions in the form of cosmic rays. Cosmic rays are very high energy protons and light atomic nuclei which originate from outside the Solar System. When they enter our atmosphere, they collide with the (primarily) nitrogen, oxygen, or argon atoms causing them to break apart creating showers of particles within the atmosphere. As the particles rain down on Earth, many of them decay into less massive ones or are absorbed in the atmosphere - muons and neutrinos are the only particles which make it to the surface. A diagram of this phenomena is seen in Figure 4.1. Indeed there are many experiments which set out to detect cosmic ray showers, but at the LHC a different approach is taken and we build machines on Earth to generate the particle collisions - although at not nearly such large energies provided by extrastellar space. The particle collisions can be focused to a single part of space, the region around the beam spot can be extensively instrumented to detect the debris of the collision.

The Large Hadron Collider (LHC) is a facility which houses two beams of protons (each beam centimeters in transverse size) running parallel in an underground ring 17 miles in circumference. The protons are accelerated to nearly the speed of light by electric fields and are steered within their circular trajectory using magnetic fields generated by superconducting magnets. A schematic of the complex which houses this machine is seen in the left panel of Figure 4.2; as seen in the diagram, the LHC is the final machine of a number of stages which each incrementally increase the energy of the protons. There are 5 locations around the ring where the beams are crossed and

particle detectors are placed. The right panel of Figure 4.2 shows the LHC complex underground near Geneva, Switzerland.

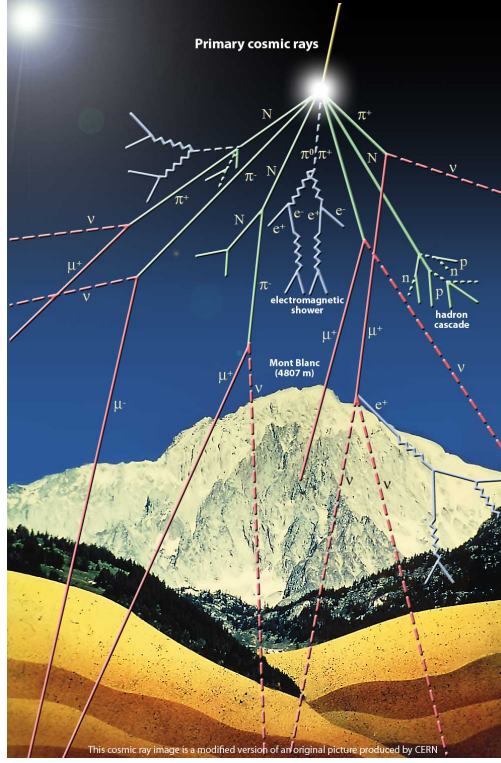


Figure 4.1: Nature's source of high-energy particle collisions: a particle shower initiated by high energy cosmic rays hitting the atmosphere.

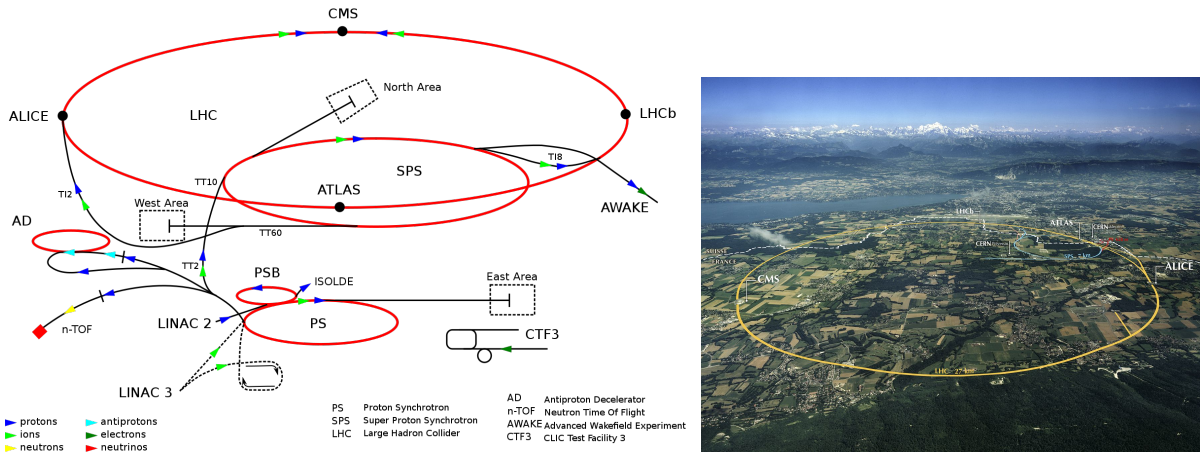


Figure 4.2: The LHC complex housing the proton-proton beams, 17 mi in circumference and 500 ft underground.

$$\mathcal{L}(t) = f \frac{n_1 n_2}{4\pi \sigma_x \sigma_y} \quad (4.1)$$

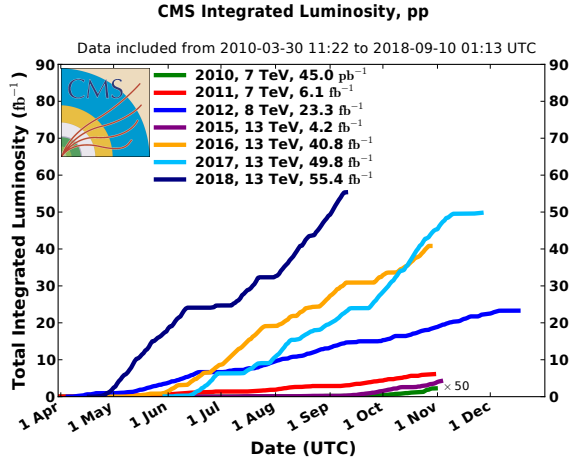


Figure 4.3: The integrated luminosity of CMS over its lifetime.

## Chapter 5

### The CMS Detector

To ensure as much as possible of the debris of the proton-proton collisions can be detected, CMS is constructed to maximize the solid-angle coverage of the interaction region. CMS is composed of a modular design of different detectors, each with their own technology and working points, allowing for direct measurements of a wide spectra of particles. Figure 5.1 illustrates how well instrumented the interaction region is, highlighting each of the detector systems. The proton-proton beamline is seen as a grey tube oriented from the bottom right to the top left of the figure. The interaction region is within the silicon tracker.

Of the SM particles, only the lightest have a long enough lifetime to travel any appreciable distance within our detector. Electrons  $e^\pm$ , photons  $\gamma$ , and protons  $p^\pm$  are stable and can be directly detected via interactions with the bulk of the detector. Muons  $\mu^\pm$ , charged pions  $\pi^\pm$ , neutrons n, and kaons  $K^\pm, K_L^0$  are intrinsically unstable but have long enough lifetimes to travel far enough to interact with our detector. The different CMS subdetectors responsible for the detection of these particles are seen in Figure 5.2. By piecing together these elements we are able to provide a reconstruction of the physics processes occurring within each particle collision. Different types of interactions leave unique signatures by decaying into specific final states, which are those we detect.

The detector can generically be divided into central *barrel* and forward *endcap* regions. The geometry either takes the form of concentric cylinders (in the barrel) or flat planes of detectors (in the endcaps). Figure 5.3 illustrates these barrel ( $|\eta| < 1.5$ ) and endcap ( $1.5 < |\eta| < 5$ ) regions.

The beamline is seen as the thin cyan line across the base of the image.

This chapter will discuss the main elements of the CMS detector, beginning with the innermost (closest to the beam pipe) silicon tracker and concluding with the muon tracker.

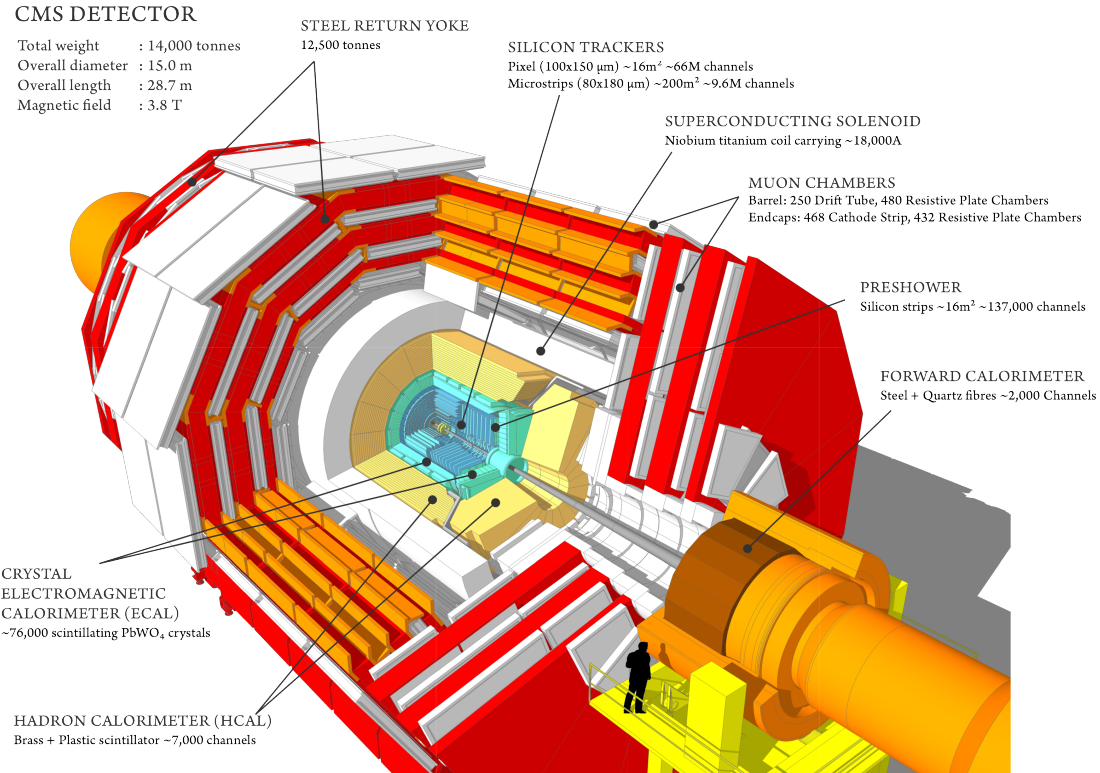


Figure 5.1: A diagram of the CMS detector. Specific detector subsystems are labeled.

## 5.1 Silicon Tracker

The silicon tracker is responsible for the reconstruction of charged particles, which are mainly electrons, muons, kaons and pions. The particle trajectory is reconstructed using ionization deposits left in layers of thin silicon. The particle momentum is measured by the curvature of the trajectory when immersed in the magnetic field. The silicon tracker is divided into two major components. The pixel detector is at a closer proximity to the beam line and has finer spatial segmentation. The strips detector covers a much larger spatial volume and is responsible for the majority of the hits along a particle trajectory. [6, 7]. A diagram of the geometry and layers of the tracker is seen in

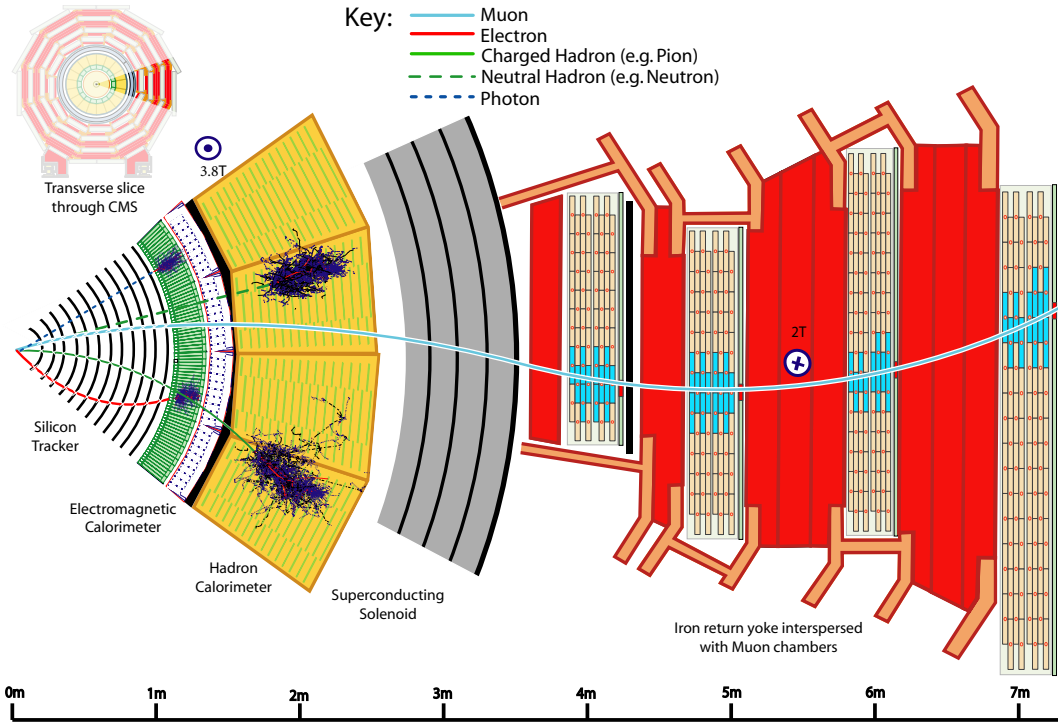


Figure 5.2: A diagram of the CMS detector in the  $r\phi$  plane; the beam axis is perpendicular to the page; SM particle signatures within the detector are shown.

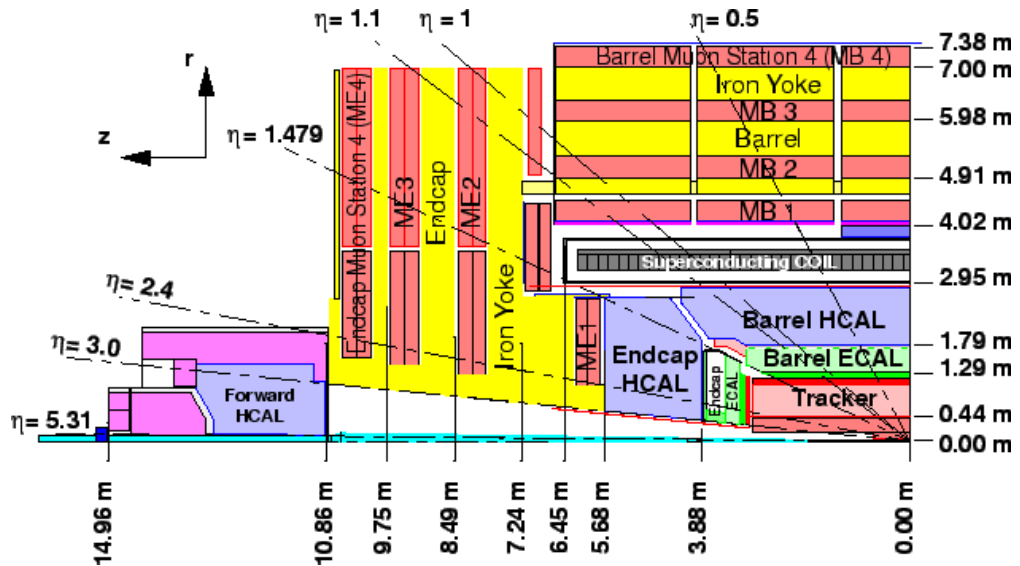


Figure 5.3: A diagram of the CMS detector in the  $rz$  plane; the beampipe is the thin cyan sliver along the bottom. The detector subtends a large solid angle about the interaction region.

Figure 5.4.

The tracker is built of modules consisting of a layer of sensitive silicon bonded on top readout electronics. The silicon is arranged as a p-n junction, reversed-biased and fully-depleted. As a charged particle travels through the material, it ionizes the silicon creating electron-hole pairs within the depletion zone. Electric fields accelerate the charge through the silicon to the readout electronics bonded to the back of the sensor. The readout chips amplify, digitize, and store the hit information before being piped outside the detector. The silicon is very thin ( $\sim 300 \mu\text{m}$ ), the tracker is constructed of as little material as possible so as not to perturb the trajectory of the particle.

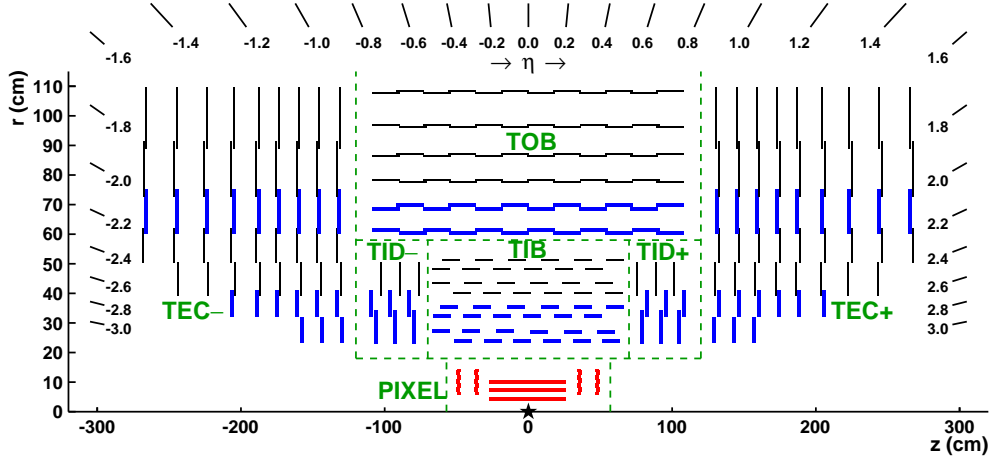


Figure 5.4: The CMS silicon tracker. The vertical and horizontal lines represent layers of silicon modules. Lines in blue represent layers with “stereo” hits, formed from two silicon layers.

### 5.1.1 Pixel Detector

The task of the pixel detector is to provide the spatial granularity required for precision track vertexing. The barrel region ( $|\eta| < 1.5$ ) of the pixel detector consists of 3 concentric cylinders sitting at radii of 4.4, 7.3, and 10.2 cm from the beamline. The endcaps ( $1.5 < |\eta| < 2.5$ ) consist of two discs on each side ( $\pm z$ ) placed at  $z = \pm 35.5, 48.5$  cm. A pixel module, used to form the detector layers, consists of 16 readout chips glued to a  $2 \times 6 \text{ cm}$  mechanical support structure. Bump-bonded to the readout chips are the  $285 \mu\text{m}$  thick silicon sensors. The readout chips and sensor are divided

up into  $100 \times 150 \mu m$  pixels which allow the excellent hit resolution (over 65 million channels for the entire detector). The  $100 \mu m$  lengths are oriented to give the most precise measurement of the  $\phi$  coordinate of the track, as that is the direction on bending due to the magnetic field.

A new pixel detector was installed in 2016 to accommodate the ever-increasing instantaneous luminosity provided by the LHC [8]. The increase in the luminosity results in many more additional proton-proton interactions per bunch crossing, called *pileup*. High pileup results in a very dense environment for track reconstruction to operate as all the individual hits in the detector layers must be disentangled correctly. To increase the performance, the new detector therefore included **4** layers in the barrel and **3** endcap discs on either end. The readout chip was upgraded to fully digital readout to give larger hit buffers to accommodate the increased hit rate.

### 5.1.2 Strips Detector

The silicon strips detector sits immediately outside the pixel detector and provides additional hits along a particle’s trajectory. The barrel region ( $|\eta| < 1.5$ ) provides 10 layers of sensor situated between 20 and 116cm from the beamline. The endcap regions ( $1.5 < |\eta| < 2.5$ ) have a total of 12 layers situated between 58 and 282cm from the center of the detector, on each side. The silicon modules are partitioned in roughly 10cm long strips which are oriented parallel to the beamline. The strip pitch varies ranging from  $80 - 180 \mu m$  wide. The silicon thickness ranges from 320 to 500  $\mu m$  thick. Some of the layers, indicated in the blue lines in Figure 5.4, have two modules which are slightly rotated relative to each other to give a “stereo-hit”, providing a more precise position measurement.

## 5.2 Electromagnetic Calorimeter

The electromagnetic calorimeter is responsible for the reconstruction of electrons  $e^\pm$  and photons  $\gamma$ . The energy is measured by collecting the light generated by an electromagnetic shower as the particle is absorbed in the calorimeter [9, 10].

The bulk of the calorimeter consists of clear lead-tungstate ( $PbWO_4$ ) crystal. Electromag-

netic showers are created when high energy photons or electrons enter the crystal. From there, a number of energy loss mechanisms may occur which eventually allow for the complete absorption of the energy of the primary particle. a) Low-mass particles, such as electrons, scatter often as they traverse the material and emit bremsstrahlung radiation. b) High energy photons are able to convert into electron-positron pairs within the crystal. c) Charged particles produce scintillation light within the crystal. These interactions proceed until eventually all the particles are sufficiently low energy and absorbed by the photodetectors mounted at the end of each crystal. Avalanche photodiodes with a gain of 50 and vacuum phototriodes with a gain of 10 are used in the barrel and endcap, respectively. The signal is then further amplified and digitized.

The electromagnetic calorimeter is divided into barrel ( $|\eta| < 1.5$ ) and endcap ( $1.5 < |\eta| < 3$ ) regions comprising 75,848 crystals. The crystals measure  $2.2 \times 2.2 \times 23$  cm in the barrel and  $3 \times 3 \times 22$  cm in the endcaps; they are oriented radially outward from the interaction region. A schematic of the detector is seen in Figure 5.5b. Additionally, the electromagnetic calorimeter serves as an absorber for the hadronic calorimeter, initiating a shower in approximately 1/3 of the hadrons that are headed the HCAL.

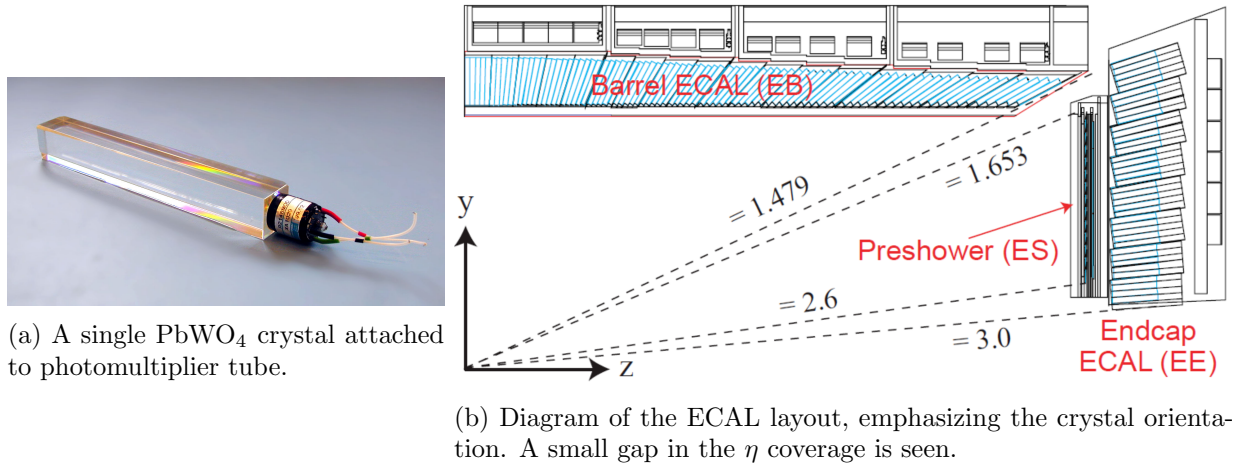


Figure 5.5: The CMS electromagnetic calorimeter.

### 5.2.1 Preshower

The preshower is an additional detector which allows for greater spatial hit resolution of calorimeter clusters in the  $1.7 < |\eta| < 2.6$  region. Placed in front of the crystal calorimeter, it consists of a lead absorber, followed by a plane of silicon-strip sensors, followed by another lead absorber, followed by an orthogonal plane of silicon strip sensors. The silicon sensors are  $320\mu m$  thick and measure  $6.1 \times 6.1\text{cm}^2$  per sensor module. Measurements in the two orthogonal directions of each silicon layer are combined to provide more precise shower shape measurements.

The preshower is designed to properly identify photon pairs resulting from high- $p_T$  neutral pion decay (98.8% branching fraction). When a sufficiently high  $p_T$  pion decays, the daughter photons become collimated to the extent they can not be separately resolved within the ECAL crystals. Proper identification of neutral pions are important as they are copiously produced in high-energy particle collisions. There is a physics motivation for instrumenting this particular region of the ECAL: at least one of the photons from  $H \rightarrow \gamma\gamma$  falls within this region of  $\eta$ .

## 5.3 Hadronic Calorimeter

The hadronic calorimeter is responsible for the reconstruction of undecayed hadrons: pions  $\pi^\pm$ , protons  $p$ , neutrons  $n$ , and kaons  $K^\pm, K_L^0$ . It is composed of 4 distinct components with some amount of overlap. It is divided into barrel ( $|\eta| < 1.4$ , HB), endcap ( $1.3 < |\eta| < 3$ , HE), forward ( $3 < |\eta| < 5.2$ , HF), and outer ( $|\eta| < 1.2$ , HO) regions [11]. A diagram of the HCAL geometry is seen in Figure 5.6.

In the HE and HB, a particle will interact with the brass absorber inducing a shower of secondary particles. These secondary particles in turn may interact with the brass, and so on creating a hadronic shower within the detector. Interspaced within the absorber are clear plastic scintillator which create flashes of light after de-excitation of the scintillating molecules embedded in the plastic. Wavelength shifting fibers are routed throughout the plastic to absorb the light, which is then piped to hybrid photodiodes. Light incident on the photodiodes liberates electrons

via the photoelectric effect which are then accelerated onto the surface of a silicon diode which further amplifies and digitizes the signal. The particle energy is therefore measured by collecting light generated by a hadronic shower as the particle is absorbed in the calorimeter.

Each of these detectors consists of 17 alternating layers of 5cm brass and 1cm plastic. The readout of the optical signals are summed into *towers* of size of roughly  $0.09 \times 0.09$  in  $\eta - \phi$ , this results in the  $\eta$  segmentation seen in Figure 5.6, labeled from 1 to 15 for HB and then 18-29 in HE. Layers of constant color represent depth segmentation of the summed light within a single tower. e.g. two energy deposits in the central HE may be formed from a single shower. (Upgrades beginning in 2020 will increase this segmentation, as well as update the signal collection to using silicon photomultipliers [12].)

The HO sits **outside** the magnet in the barrel region  $|\eta| < 1.2$  and collects additional radiation not absorbed in the material in front of it with an additional layer of scintillator planes.

An addition to HB, HO, and HE, there is a steel calorimeter HF which detects radiation in the very forward region  $3 < |\eta| < 5.2$  on each side of the interaction point. This forward region has a very large radiation flux - the majority of the proton-proton interactions are “glancing blows” in which there is very little momentum transfer and the particles are deflected only slightly, directly into this region of the detector - this environment requires a different approach than in the rest of the HCAL. Each detector is comprised of 165cm thick steel interspersed with radiation-hard quartz fibers (parallel to the beamline) to collect light which is read out by photomultipliers. The tower size in this detector is about  $0.175 \times 0.175$  in  $\eta - \phi$ .

## 5.4 Solenoidal Magnet

The solenoidal magnet provides the magnetic field necessary to deflect charged particles within the tracker volume to allow for a measurement of the momentum. The tracker, ECAL, and HCAL all fit inside the magnet bore diameter of 6m and length of 12.5m. It delivers a 3.8T solenoidal field (parallel to the beampipe) within the tracker volume. The field is produced by running current through coils of superconducting NbTi wires cooled to less than 5K. The magnetic

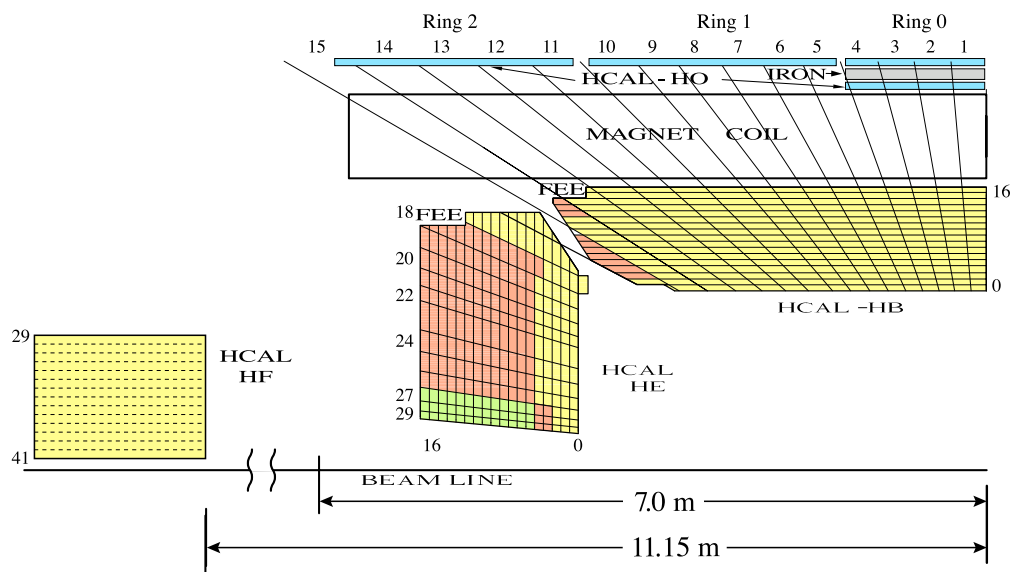


Figure 5.6: The CMS hadron calorimeter [13].

field lines are returned via steel yokes sitting outside the magnet interspaced within the muon tracker volume, the field strength throughout the muon system is approximately 2T [14]. A simulation of the magnetic field within the whole of CMS is seen in Figure 5.7 [15].

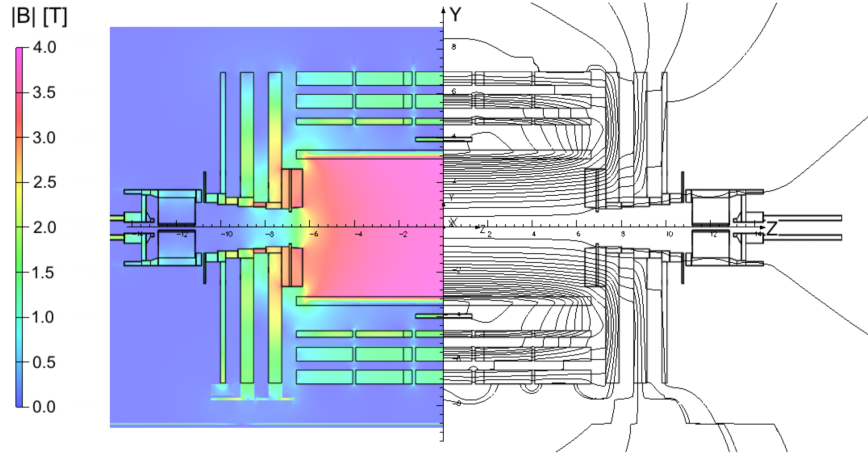


Figure 5.7: A simulation of the 4T CMS magnetic field. Note the uniformity within the tracker volume.

## 5.5 Muon System

The muon system is responsible for the reconstruction (and triggering) of muons  $\mu^\pm$ . The muon trajectory is reconstructed using ionization deposits left in layers of gaseous detectors. The muon momentum is measured by the curvature of the trajectory when immersed in the magnetic field [16].

The muon system sits at the furthest distance from the beamline, high performance reconstruction is made possible by the balanced combination of the muon and detector properties. Any particles which have made the journey to the muon system have traveled far and through many layers of detector material (e.g. Si, PbWO<sub>4</sub>, Cu), Fe before finally being detected. Many particles are unstable and decay before reaching the muon system; other particles are absorbed in either of the calorimeters. But the muon has a relatively large mass (compared to an electron) and is not very likely to initiate electromagnetic showers in the ECAL. Nor does the muon interact strongly,

and so there will be no hadron showers within the HCAL. Muons have a sufficiently long lifetime to make it to the outer detector. This combination yields a very pure sample of reconstructed muons.

There are three components of the muon system: The drift tubes (DT) are in the barrel ( $|\eta| < 1.3$ ), the cathode strip chambers (CSC) are in the endcaps ( $0.9 < |\eta| < 2.4$ ), and resistive plate chambers (RPC) are in both regions ( $|\eta| < 1.6$ ). These detectors rely on different technology and have some amount of overlap with each other. All detectors participate in triggering and track reconstruction, but the DTs and CSCs provide greater position and momentum resolution, while the RPCs have excellent timing resolution allowing for more precise bunch crossing tagging.

### 5.5.1 Drift Tubes

The drift tubes are used for muon tracking in the barrel portion of the detector ( $|\eta| < 1.3$ ). The basic element is a gas tube  $4 \times 1.3$  cm in transverse size and 2-4 m long (depending on its position). High-voltage is applied to a wire strung the length of the cylinder and collects charge released when an incident muon ionizes an 85/15% Ar/CO<sub>2</sub> gas mixture [17].

The drift tubes are divided into four barrel regions (each called a station) at different radii within the magnetic return yoke. Each station contains 3 *superlayers*, where a superlayer is composed of four layers of stacked tubes, each layer staggered by one half width. For each station, two of the superlayers are oriented parallel to the beamline for  $r - \phi$  measurements and one superlayer is perpendicular to the beamline to allow for measurements of the r-z position. An image of a DT station is seen in Figure 5.8.

### 5.5.2 Cathode Strip Chambers

The cathode strip chambers are used for muon tracking in the endcap portion of the detector ( $0.9 < |\eta| < 2.4$ ). The system is divided up into 468 trapezoidal chambers arranged in 2 or 3 concentric rings on a disk. There are 4 discs on either side of the detector ( $\pm z$ ). The geometry of the chambers on a disk are seen in Figure 5.9a (an example image of the hit occupancy of a disc during cosmic ray runs). Each chamber (diagram in Figure 5.9b) consists of 6 layers of electrode

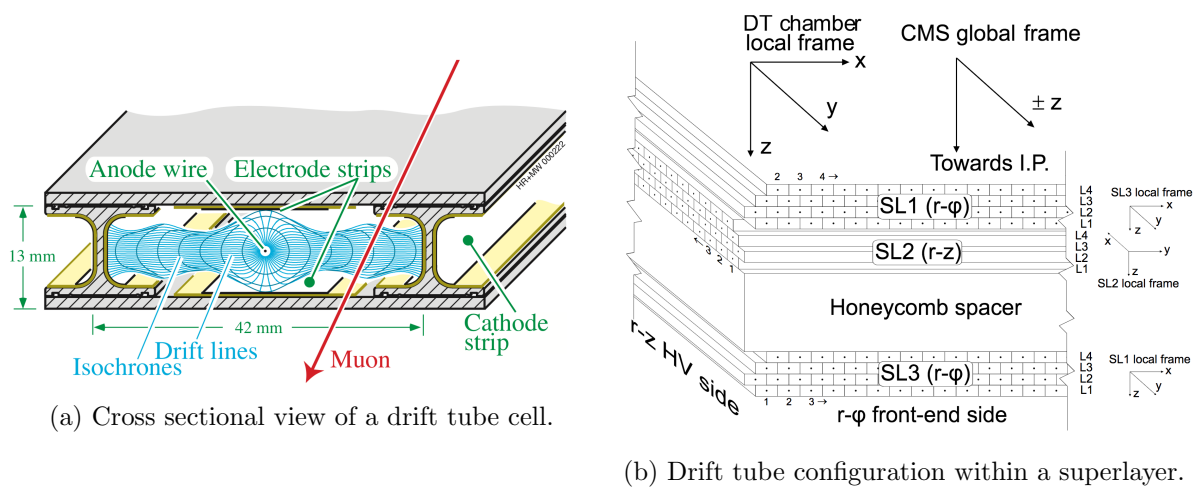


Figure 5.8: The CMS muon drift tube detector [18].

planes separated by a gas layer of  $C_2H_2F_4$  (freon) and  $C_4H_{10}$  (isobutane). Wires are strung in the phi direction (concentric circles about the z axis) and therefore make a measurement of the radial coordinate of the hit. The electron shower generates an image charge in cathode planes. For each layer, one of the planes is segmented into strips which are perpendicular to the wires providing an good measure of the  $\phi$  coordinate [19].

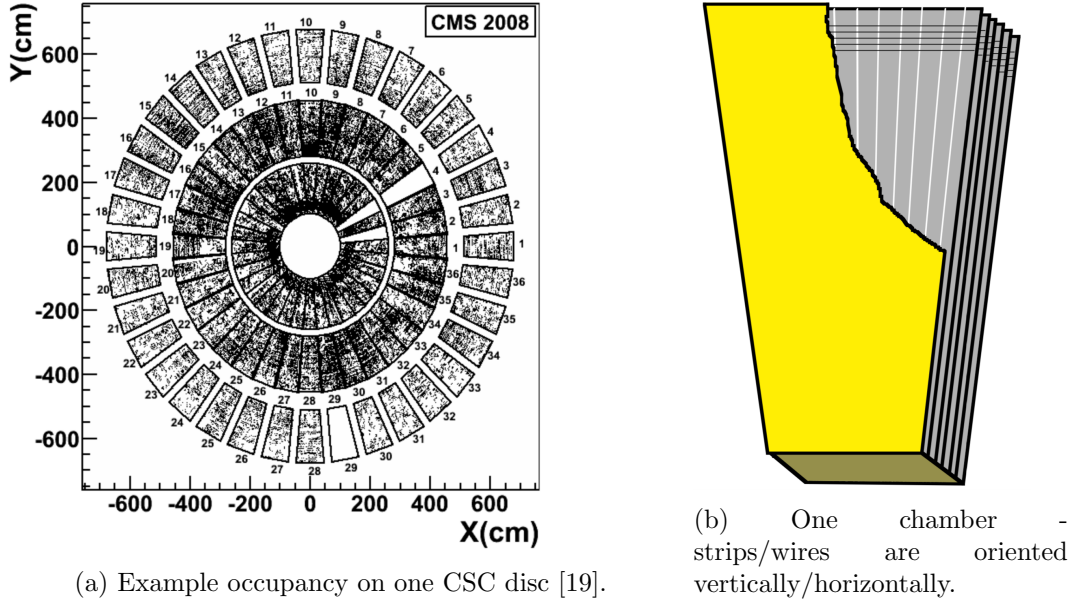


Figure 5.9: The CMS muon cathode strip chambers.

### 5.5.3 Resistive Plate Chambers

Resistive plate chambers cover the region  $|\eta| < 1.6$  and are interspersed within CSC and DT and the magnetic return yoke [20]. They have an excellent timing resolution of about 3 ns which allows for fast muon triggering and identification of the different bunch crossings. Pattern matching across the hits in the different layers allows for estimates of the muon  $p_T$  to be used in further trigger processing. Hits created in the resistive plate chambers are additionally used for global fitting of the muon tracks.

The resistive plate chambers consist of an airtight system of two parallel high-resistivity planes separated by a 1 cm gas gap. The outside of each plate is coated to form an electrode for

the high-voltage bias. On top of each electrode sits aluminum strips which are insulated from the electrode and serve as the readout. Electron showers created in the gas bulk induce an image charge on the strips which is then recorded. The gas mixture is 95/5% C<sub>2</sub>H<sub>2</sub>F<sub>4</sub> (freon) and C<sub>4</sub>H<sub>10</sub> (isobutane), with trace amounts of SF<sub>6</sub>. A diagram of an RPC chamber is seen in Figure 5.10.

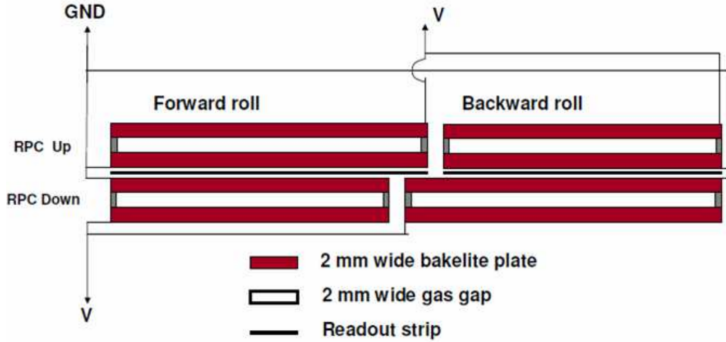


Figure 5.10: The CMS muon resistive plate chamber [20].

## 5.6 Trigger System

While in operation mode, the LHC provides collisions at a rate of 40 MHz (25ns per bunchcrossing). This is a phenomenal rate which the CMS detector bandwidth is not able to accommodate, nor does the experiment have access to the amount of storage space necessary to store all this information. Therefore, the CMS detector makes use of a trigger system to quickly determine if the event is 'interesting' and will be saved for storage - events which are not triggered are lost forever. Examples of interesting events are those with high- $p_T$  muons, or a large imbalance in the total momentum of the event [21].

The trigger consists of two stages known as the Level-1 (L1) and High-Level Trigger (HLT). L1 is a hardware based trigger which combines information from the calorimeters and muon systems to make a decision if the event will be passed to HLT for further processing. L1 is able to reduce the event rate from 40 MHz to 100 kHz and must make the decision within 4  $\mu s$ . Primitive objects such as calorimeter energy deposits or muon track segments are first constructed locally within the detector before being combined to form the global decision at L1. If the decision is made at L1

that the event is of potential interest, it is passed to HLT. HLT is a software based trigger which makes use of more sophisticated reconstruction algorithms which can be tuned to select events of choice.

## Chapter 6

### Event Reconstruction

#### 6.1 Basic Elements From the Detector

Depending on their nature, the particles emanating from the collision leave various forms of energy deposits in the different subdetectors. All these signals need to be aggregated and processed to allow for the reconstruction of what could be considered particle-level information. The first step in this process consists of building *Particle Flow elements* using information only locally within each subdetector. There are four primary elements from the subdetectors: tracks from the tracker, calorimeter deposits in each of the ECAL and HCAL, and tracks from the muon detector. The elements are eventually combined via the *Particle Flow algorithm*, yielding reconstructed particles used for physics analysis.

Note that the definition of any object within the detector makes use of additional selection criteria which are not generally discussed here. For instance, one may require that a track in the tracker have at least 3 hits in the pixel detector, or that a calorimeter hit is above some minimum threshold energy. The effects of these criteria are generally a balance between the reconstruction efficiency of any given particle and the probability to misidentify a particle (purity).

##### 6.1.1 Tracks and Vertices

Tracker hits are formed in the pixel and strips detectors by clustering any hits in neighbouring elements of the detector plane. The cluster position is measured by weighted average of the individual channel positions. Charge sharing among detector channels allow for a finer spatial

resolution in the position measurement. Track reconstruction first begins by forming track seeds consisting of a small number of detector hits. These track seeds are then projected onto successive detector layers looking for nearby additional hits. This follows the Kalman filtering procedure, in which track information is updated after the addition of each hit. Electron tracking is performed with a slightly modified algorithm to better account for the energy loss mechanisms as the electron traverses the detector [22].

The track building procedure follows an iterative procedure, where the requirements on the quality of the track seed decrease as the iterations proceed. The first iterations begin with seeds consisting of 3 pixel hits and lead to high performance reconstruction of high  $p_T$  tracks emanating from the collision region. The iterations proceed until essentially only requiring hits in the outer tracker and reconstructs displaced tracks or those missing hits. The iteration procedure provides a balance between reconstruction efficiency, track purity, and computation economics. Table 6.1 lists these iterations - the requirements on the seed and types of tracks that iteration targets.

Table 6.1: Seeding requirements for each step in the iterative track reconstruction [23].

Iteration	Name	Seeding	Targeted Tracks
1	InitialStep	pixel triplets	prompt, high $p_T$
2	DetachedTriplet	pixel triplets	from b hadron decays, $R \lesssim 5$ cm
3	LowPtTriplet	pixel triplets	prompt, low $p_T$
4	PixelPair	pixel pairs	recover high $p_T$
5	MixedTriplet	pixel+strip triplets	displaced, $R \lesssim 7$ cm
6	PixelLess	strip triplets/pairs	very displaced, $R \lesssim 25$ cm
7	TobTec	strip triplets/pairs	very displaced, $R \lesssim 60$ cm
8	JetCoreRegional	pixel+strip pairs	inside high $p_T$ jets
9	MuonSeededInOut	muon-tagged tracks	muons
10	MuonSeededOutIn	muon detectors	muons

### 6.1.2 ECAL & HCAL Clusters

*Superclusters* are built by first identifying a crystal with the largest energy deposit, this is called a *seed*. The supercluster is then formed by aggregating any hits among the neighbors (8) of the hits already in the cluster. This process then proceeds building all the superclusters and consuming all the calorimeter hits. Superclusters are built separately in the barrel and endcap.

Within a given supercluster, N clusters are identified using an iterative algorithm assuming the observed hits arise from N Gaussian-distributed energy deposits; each of energy E, position in the  $\eta - \phi$  plane  $\vec{\mu}$ , and width  $\sigma$  scale set by the crystal size.

### 6.1.3 Muon Tracks

As there are multiple detector layers within a single muon station, track segments are locally formed within a chamber for both the DTs and CSC. These track segments represent the muon momentum at that station; pattern recognition is able to provide to measurement and its high speed allows the segments to be used trigger primitives for the muon systems. For track reconstruction, the track segments act as seeds for the track finding algorithm. The hits in each the DT, CSC, and RPC subdetectors are used in the final track reconstruction.

## 6.2 Obtaining a Particle-level Description

Once the elements have been built, the Particle Flow algorithm exploits the information from each of the detectors to form the best possible particle candidate [23]. As different varieties of particles have unique signatures in the detector, particle identification is aided by the particular combination of elements *linked* with one another. An illustrative example of these combinations are shown in Figure 5.2. Elements are linked when projections from one element to the other are spatially consistent. There are four primary links:

- Tracks formed in the tracker are linked to an ECAL or HCAL cluster if the projection of the track, at a depth of the expected maximum of a shower in the ECAL or at one interaction length inside the HCAL, lies within the cluster area.
- ECAL and HCAL clusters are linked if the ECAL cluster falls within the envelope of the HCAL cluster; ECAL provides finer spatial resolution compared to the HCAL.
- A tracker track and a muon track are linked if their projections onto a common surface are spatially consistent.

- To collect bremsstrahlung radiation (photons) associated to an electron track, an ECAL cluster is linked to tracker tracks if projections tangent to the track at any of the tracker layers lies within the cluster volume. Additionally, as the probability for a photon to convert to an  $e^+e^-$  pair is significant within the tracker, track pairs are linked if they are consistent with photon conversion.
- If a Preshower cluster is within the envelope of an ECAL cluster the two are linked; Preshower has finer spatial granularity.
- Tracks consistent with arising from a secondary vertex are linked to allow for reconstruction of nuclear-interactions.

Particle Flow *blocks* are constructed by aggregating objects directly or indirectly linked with one another. The Particle Flow algorithm then processes each block in turn to create the final reconstructed particles. The algorithm builds the objects in the following order

(1) **Muons:** There are three types of tracks which can be used for muon reconstruction:

- ***standalone*** muons are built from tracks reconstructed solely in the muon system.
- ***tracker*** muons are built from tracks reconstructed solely in the inner silicon tracker. It is tagged as being from a muon if, when projected onto a common surface, it is spatially consistent with a muon solely reconstructed from the muon chambers.
- ***global*** muons are reconstructed using the hits from both the inner silicon tracker and the muon stations. The track pairing is the same done for tracker muons. For momenta above 200 GeV, the use of the muon system for tracks improves the momentum measurement.

Any ECAL or HCAL clusters associated with the muon track are used as muon selection/definition criteria if those clusters are found to be consistent with the muon hypothesis.

## (2) Electrons & Isolated Photons:

An electron is formed by combining a track in the silicon tracker with a cluster in the ECAL. Its energy assignment uses a combination of both elements. The momentum direction is made using the track in the silicon tracker, as it gives greater spatial resolution. A photon is defined as an ECAL cluster not associated with a track. Photon isolation is a requirement on the sum of the track  $p_T$  within a cone  $\Delta R = 0.3$  around the photon; photons which arise during hadron fragmentation (i.e. poor isolation) are treated in the next section.

Electrons and isolated photons are reconstructed within the same Particle Flow step to account for similar behavior within the tracker bulk. There is a large probability for both a) an electron to radiate a brehmsstrahlung photon and b) for a photon to convert to an  $e^+e^-$  pair. Therefore in object reconstruction care must be taken to collect the photons radiated from electrons in order to make appropriate measurements of the particles.

## (3) Hadrons & non-isolated Photons:

Hadrons & non-isolated photons result from hadronization/fragmentation of jets. ECAL clusters not associated to any tracks are assigned to be photons. Neutral hadrons ( $K_L^0$ , neutrons) are reconstructed from HCAL clusters with no associated track; neutral hadrons leave a very small amount of energy in the ECAL. Charged hadrons ( $\pi^\pm$ ,  $K^\pm$ , protons) are reconstructed using the remaining tracks and HCAL deposits. Charged hadrons do not radiate bremsstrahlung photons nor cause  $e^+e^-$  pair creation and thus do not leave signals in the ECAL.

## (4) Nuclear Interactions:

Nuclear interactions can occur when hadrons from the pp collision interact within the detector material causing a shower of secondary particles. If multiple tracks are linked through a common secondary vertex they will be summed to create a single charged hadron particle which replaces its constituents in the particle list of the event.

## 6.3 Additional High-Level Objects

### 6.3.1 Jets

Bare quarks and gluons can never be observed in Nature due to a QCD phenomenon called *color confinement*. Therefore, quark and gluon production manifests as a “jet” of color-neutral particles emanating from the production point. These particles can be clustered together to reconstruct the original parton. The jets used in this analysis are made by clustering particles with the “anti-kt” algorithm with cone sizes of  $\Delta R = 0.4, 0.8$  [24], denoted as AK4 and AK8 jets respectively. This algorithm produces nearly conical jets and is infrared and collinear safe. The AK4 jets subtend less solid angle and are used to capture the hadronisation of single quarks and gluons. AK8 jets subtend a larger solid angle and are used for reconstruction of boosted objects that decay to multiple jets (e.g.  $t$ , H, Z, W).

### 6.3.2 b-tagging of Jets

Jets resulting from the production of b quarks (and to some extent c quarks) garner special attention in our experiment. As usual for quarks and gluons, the b-quark will quickly hadronize and form a b hadron. However, the lifetimes of b hadrons are such that it will generally travel hundreds of microns before decaying. Vertexing the tracks resulting from the decay will reveal the presence of a *secondary vertex* which is spatially displaced from the primary vertex from which the other hadrons inside the jet originate. This secondary vertex allows for one handle on being able to identify jets as coming from b quark production. Other handles include the momenta and multiplicity of the other particles clustered into the jet.

In addition to tagging jets as originating from a single b quark, tagging of jets as originating from **two** b quarks is also possible [25].

### 6.3.3 Invisible Particles $\rightarrow p_T^{\text{miss}}$

Neutrinos are so weakly interacting that they leave no energy deposits in CMS and cannot be detected by our experiment. Although direct detection is not possible, we are able to infer their presence. The net momentum of the protons involved in the collisions are zero, but the individual partons (quarks and gluons) within the proton carry unknown fractions of this total (longitudinal) momentum. Only in the transverse direction may we require momentum conservation. We define this imbalance as:

$$p_T^{\text{miss}} \equiv \left| - \sum_i \vec{p}_T^i \right|, \quad \forall \text{ particles i.} \quad (6.1)$$

In the case all the particles in the event are perfectly reconstructed,  $p_T^{\text{miss}}$  would equal zero. Large values indicate the presence of an undetected particle, such as a SM neutrino or something more exotic like the light supersymmetric neutralinos  $\chi_0^0, \chi_1^0$ . This quantity is sometimes labeled as *MET*.

### 6.3.4 $\pi^0$ meson

Charged and neutral  $\pi$  mesons are the lightest of all hadrons with masses of 140 and 135 MeV, respectively. Pions are copiously produced within hadronic interactions and often contain much of the jet energy. As a rule-of-thumb, the charged to neutral energy fraction within a jet is approximately two-thirds to one-third (to match the respective pion multiplicities).

Because the neutral pion branching to photons is over 98% and its lifetime is relatively short (25.5 nm), the detection of neutral pions therefore involves reconstruction of photon pairs with the appropriate invariant mass. This is simple enough in principle, but as the pion  $p_T$  increases the photons from the pion decay become more and more collimated. Eventually, for pions above about 7 GeV, individual photons are not able to be resolved because of the ECAL resolution (crystal size), the same crystal gets the energy from both photons. This was the primary motivation for the Preshower ECAL detector.

## Chapter 7

### Search for new physics using boosted H bosons and missing energy

#### 7.1 Motivation & Strategy

If a more unifying theory than the SM exists it certainly has not been forthright in its manifestation. One possibility for the lack of discoveries of phenomena not explained within the SM is that there are indeed particles existing in nature which have not been observed, but they have such a large mass that the energy of the proton-proton collisions provided by the LHC is insufficient to directly create them. The outcome of many searches for new particles is thus the setting of limits placed on the cross section of their production mechanism. As these cross sections are dependent on the particle mass, the limits can be interpreted as setting lower bounds on the mass of any new physics - if the particle were any lighter than this limit it would have been produced copiously enough for its unambiguous detection (see for example [4, 5]). As these particles become more massive more momentum is imparted upon the particles involved in the final state; any SM particles resulting from the decay of higher mass states will be produced with large momentum (this is called high boost). As a particle becomes more boosted its decay products are emitted at smaller angles, eventually collimating sufficiently to be reconstructed as a single jet. If new physics exists with masses accessible at the LHC, one could suspect that there exists non-zero coupling with the electroweak H, Z, or W bosons. Observation of events containing high- $p_T$  ( $>300$  GeV) electroweak bosons are thus of considerable interest for finding new particles of large mass.

The Minimal Supersymmetric SM contains a  $\mathbb{Z}_2$  symmetry in which all SM particles have charge -1 and all supersymmetric particles have charge +1, this is called R-parity [2]. One direct

consequence of R-parity is that the decay of a massive supersymmetric particle must include at least one supersymmetric particle in the final state. Necessarily this is the lightest such particle in the theory, denoted the lightest supersymmetric particle (LSP). If the LSP is electrically neutral it may escape detection, creating an imbalance in the net momentum of the event (similar to a neutrino). Therefore, events with a large momentum imbalance are also interesting as potential regions for SUSY.

With this as motivation, we designed an analysis searching for physics beyond the SM in events with boosted H or Z bosons and a large transverse momentum imbalance of the event. We reconstruct the H and Z bosons in the  $b\bar{b}$  decay mode, with 57% and 15% branching fractions, respectively. Although our analysis is sensitive to any new physics with this final state, we have adopted two benchmark models (known as SMS models [26] - phenomenological models of SUSY at hadron colliders), seen in Figure 7.1, to give motivation to the analysis. In this scenario, the proton-proton interaction produces a pair of gluinos  $\tilde{g}$  (the blob in the figure indicates we are not interested in the particulars of the gluino production mechanism) which decay to a neutralino  $\tilde{\chi}_2^0$  along with the emission of quarks. This neutralino  $\tilde{\chi}_2^0$  further decays into neutralino  $\tilde{\chi}_1^0$  with the emission of a H or Z boson. The neutralino  $\tilde{\chi}_1^0$  is the LSP and escapes detection.

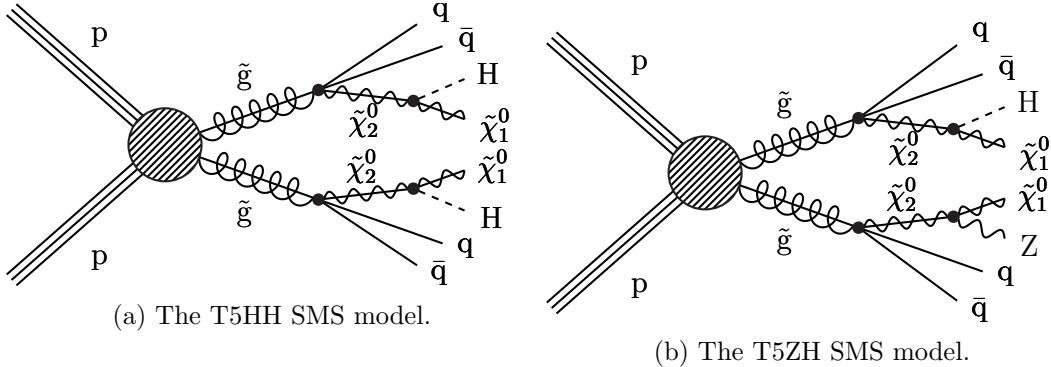


Figure 7.1: Diagrams of the benchmark models used for motivation of the targeted signal.

## 7.2 Object Definition & Event Selection

We establish a baseline selection choosing events with all-hadronic final states and missing transverse momentum ( $p_T^{\text{miss}}$ ), as motivated by Figure 7.1. The baseline selection is as follows:

- $\geq 2$  AK8 jets, with  $p_T > 300 \text{ GeV}$  and  $50 < \text{mass} < 250 \text{ GeV}$
- $p_T^{\text{miss}} > 300 \text{ GeV};$
- no isolated electrons with  $p_T > 10 \text{ GeV}:$

To remove events with  $W \rightarrow e\nu$ . Isolation requires the  $p_T$  sum of the particles within a cone of  $\Delta R < 0.2$  to be less than 10% of the electron  $p_T$ . (See [27] for details about “mini-isolation”.)

- no isolated muons with  $p_T > 10 \text{ GeV}:$

To remove events with  $W \rightarrow \mu\nu$ . The energy fraction for the isolation requirement is relaxed to 20%.

- no isolated tracks:

To remove events with top or W production in which the W decays to a tau. The tau branching fraction to states containing at least one charged particle is 85%. As an isolated track is defined by looser criteria than that of an electron or muon, this cut also serves to increase the efficiency of the isolated electron and muon vetoes. Leptonic tracks must satisfy  $p_T > 5 \text{ GeV}$  and have 20% isolation. Hadronic tracks must satisfy  $p_T > 10 \text{ GeV}$  and have 10% isolation.

- $\Delta\phi_{1,2,3,4} > 0.5, 0.5, 0.3, 0.3$ ;  $\Delta\phi_i \equiv \Delta\phi(p_T^{\text{miss}}, \text{AK4 jet}_i)$

The  $\Delta\phi$  cut is designed to remove QCD events in which a jet is under-measured leading to an artificial imbalance in the event  $p_T$ . This cut requires that the difference in  $\phi$  between the  $p_T^{\text{miss}}$  vector and each of the four highest- $p_T$  jets is sufficiently large to remove events in

which a jet has been under-measured giving rise to fake  $p_T^{\text{miss}}$  pointing in the same direction. If less than four AK4 jets are available the additional cuts are removed.

A dedicated heavy tagging algorithm is used to identify AK8 jets arising from the decay of two b quarks [25]. The distribution of the output discriminator for the two highest- $p_T$  AK8 jets are seen in the left and right panels of Figure 7.2; signal-like events peak towards larger values. To  $b\bar{b}$  tag the AK8 jets we choose the loose working-point ( $>0.3$ ) corresponding to an efficiency of approximately 70 – 80% for  $H \rightarrow b\bar{b}$  (see Figure A.1). The stacked histogram and solid lines shows the distribution after baseline selection for simulation and two representative signal points, respectively.

Further H/Z tagging of an AK8 jet is accomplished by restricting the jet mass window to [85, 135 GeV] to be consistent with that of the H boson. The distributions of the jet mass are seen in Figure 7.2. The signal shown in the solid line is the T5HH model (i.e. Figure 7.1a). The same identification criteria are applied to tag an AK8 jet as either an H or Z boson, there is no distinction made.

### 7.3 Dataset & Trigger

We use a total of 35.9  $\text{fb}^{-1}$  of data collected by the CMS experiment in 2016. Events are selected with the requirement of at least 100 GeV of  $p_T^{\text{miss}}$  calculated at high-level trigger (HLT\_PFMET100\_PFMHT100\_IDTight, HLT). To improve the trigger efficiency, the logical OR of similar triggers of thresholds 110, 120 GeV are included.

The HLT is seeded at level-1 (L1) by the requirement of at least 100 GeV of missing transverse energy (L1\_ETM100). Missing transverse energy is calculated by the vectorial sums of the regional energy deposits in the calorimeters (and rotation by 180°). This is additionally ORed with similar seeds of thresholds 90, 80, 70, 60, 50 GeV. Two additional ORed seeds require calorimeter jets with  $p_T$  of at least 60 GeV (L1\_ETM60\_Jet60\_dPhi\_Min0p4, L1\_DoubleJetC60\_ETM60).

The trigger efficiency is defined as  $\epsilon = N_1/N_2$ , where  $N_2$  is the total number of events passing

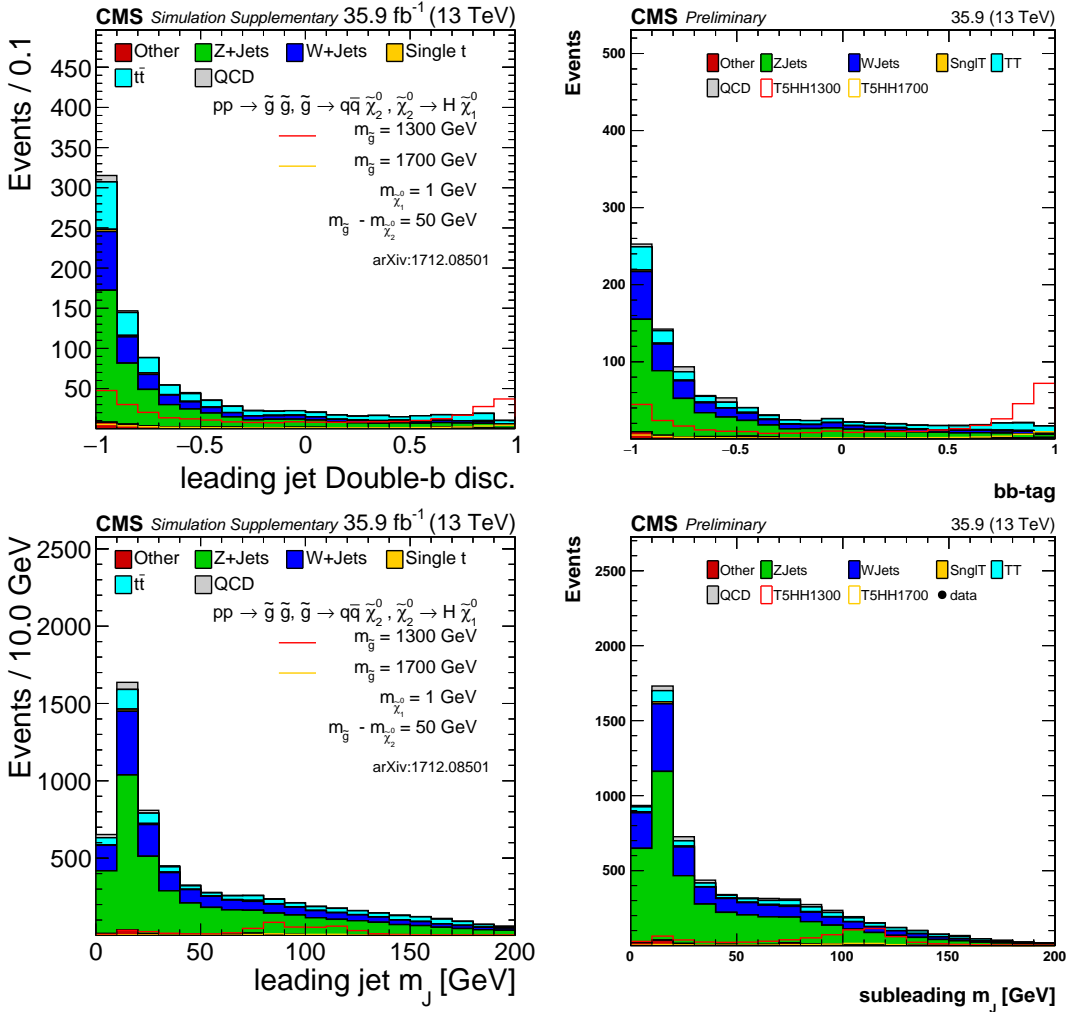


Figure 7.2: Distributions of the bb-tagging discriminator (top row) and the jet mass (bottom row) for the highest (left column) and second highest (right column)  $p_T$  AK8 jets. In the signal models, the H bosons are allowed to decay inclusively.

baseline selection and  $N_1$  is the total number of events selected by the trigger and passing baseline selection. In order to calculate this efficiency, we need to form an additional (hopefully independent) dataset by selecting events via a *reference trigger*. Our reference trigger requires a single electron of  $p_T > 27 \text{ GeV}$ , in addition to the baseline selection we require these events to contain at least three AK4 jets and exactly one reconstructed electron of  $p_T > 25 \text{ GeV}$ . The signal region trigger is found to be greater than 98% for events with  $p_T^{\text{miss}} > 250 \text{ GeV}$  and  $H_T > 300 \text{ GeV}$  [4]. This correction is ultimately applied as a systematic error to the final results.

## 7.4 Event Simulation

Event simulation of the proton-proton collisions proceeds in several steps. To simulate the hard physics process MadGraph@NLO2.2.2 [28] is used to calculate matrix-element amplitudes. The parton distribution functions (PDFs) used in these calculations are from NNPDF 3.0 [29]. Parton showering and other event dynamics are generated with Pythia [30]. The final-state particles are traced through the detector using GEANT. For example, this includes the effect of the magnetic field, interactions with both the dead and sensitive detector material, and additional particle decay [31]. This simulated data is processed in the same manner as that of the physical experiment.

### 7.4.1 Standard Model Processes

The SM samples which enter as the primary backgrounds are listed in Table 7.1 (see Section 7.5.1 for a discussion of the background). All samples are generated with a pileup distribution with an average of 25 interactions per bunch crossing and a 25ns interval between bunches. For acceptable statistics over a wide range of parameter space, the samples are often binned in  $H_T \equiv \sum_{\text{AK4 jets}} p_T$ . As our event selection requires at least two AK8 jets with  $p_T > 300 \text{ GeV}$  we roughly operate in the regime of  $H_T > 600 \text{ GeV}$ .

Table 7.1: SM samples used in the analysis.

process	final state	$H_T$ (GeV)	$\sigma$ (pb)	$\int \mathcal{L}$ ( $\text{fb}^{-1}$ )
$t\bar{t}$	$t \rightarrow \ell\nu, \bar{t} \rightarrow 2q$	inclusive	182.72	283.90
$t\bar{t}$	$\bar{t} \rightarrow \ell\nu, t \rightarrow 2q$	inclusive	182.72	326.48
$t\bar{t}$	$2\ell$	inclusive	88.34	346.25
$t\bar{t}$	inclusive	[600, 800]	2.734	5231.81
$t\bar{t}$	inclusive	[800, 1200]	1.121	9416.61
$t\bar{t}$	inclusive	[1200, 2500]	0.198	14819.34
$t\bar{t}$	inclusive	[2500, $\infty$ ]	0.002	221088.29
QCD	inclusive	[200, 300]	1735000	0.03
QCD	inclusive	[300, 500]	366800	0.16
QCD	inclusive	[500, 700]	29370	1.95
QCD	inclusive	[700, 1000]	6524	6.68
QCD	inclusive	[1000, 1500]	1064	12.62
QCD	inclusive	[1500, 2000]	121.5	32.63
QCD	inclusive	[2000, $\infty$ ]	25.42	239.30
Z+jets	$\nu\bar{\nu}$	[100, 200]	344.8	54.13
Z+jets	$\nu\bar{\nu}$	[200, 400]	95.53	208.46
Z+jets	$\nu\bar{\nu}$	[400, 600]	13.20	77.30
Z+jets	$\nu\bar{\nu}$	[600, 800]	3.148	1795.26
Z+jets	$\nu\bar{\nu}$	[800, 1200]	1.451	1486.09
Z+jets	$\nu\bar{\nu}$	[1200, 2500]	0.355	1029.81
Z+jets	$\nu\bar{\nu}$	[2500, $\infty$ ]	0.0085	47498.87
W+jets	$\ell\nu$	[100, 200]	1627.45	18.16
W+jets	$\ell\nu$	[200, 400]	435.24	45.88
W+jets	$\ell\nu$	[400, 600]	59.18	123.64
W+jets	$\ell\nu$	[600, 800]	14.58	221.32
W+jets	$\ell\nu$	[800, 1200]	6.66	1123.13
W+jets	$\ell\nu$	[1200, 2500]	1.608	153.44
W+jets	$\ell\nu$	[2500, $\infty$ ]	0.039	6497.28

#### 7.4.2 Signal Models

For commissioning of the analysis technique (as well as the limit-setting procedure, see Section 7.7) Monte Carlo samples with our final-state signal topology were generated, based on the processes in Figure 7.1. The signal sample follows the same processing chain as the SM samples. The mass splitting between the gluino  $\tilde{g}$  and neutralino  $\tilde{\chi}_2^0$  is fixed to 50 GeV, resulting in low  $p_T$  SM quarks produced in the gluino  $\tilde{g}$  decays. The mass of the neutralino  $\tilde{\chi}_1^0$  (LSP) is fixed to 1 GeV. We have samples with a range of gluino  $\tilde{g}$  masses from 750 to 2200 GeV. The  $p_T$  distribution for the generated H bosons in these samples is seen in Figure 7.3 for a number of gluino  $\tilde{g}$  masses. Additionally the angular separation  $\Delta R \equiv \sqrt{\Delta\phi^2 + \Delta\eta^2}$  between the  $b\bar{b}$  pair is shown. As the  $p_T$  of a parent boson increases the  $b\bar{b}$  pair from its decay tend to align, allowing complete reconstruction with a single AK8 jet.

#### 7.5 Event Binning & Background Estimation

The background estimation procedure makes use of what is known as an “ABCD” prediction in which the analysis phase space is divided into signal and sideband regions; scaling relations are applied to sideband yields to make predictions for the background in the signal regions. The events are categorized according to whether the two highest  $p_T$  AK8 jets are a) in the signal or sideband mass region and b) have or have not been  $b\bar{b}$  tagged. A diagram of this partitioning is seen in Figure 7.4. An additional dimension is added by binning in  $p_T^{\text{miss}}$  : [300, 500 GeV], [500, 700 GeV], [700,  $\infty$  GeV]. This gives a total of  $2 \times 3 = 6$  signal and  $4 \times 3 = 12$  sideband bins. The two signal regions  $A_1$  and  $A_2$  contain events with exactly one and exactly two jets being consistent with H/Z boson decay, respectively.

Assuming that there is no correlation between the jet mass and the  $b\bar{b}$  tagging one would expect that

$$\frac{A_1}{B_1} = \frac{A_2}{B_2} = \frac{C}{D} \quad (7.1)$$

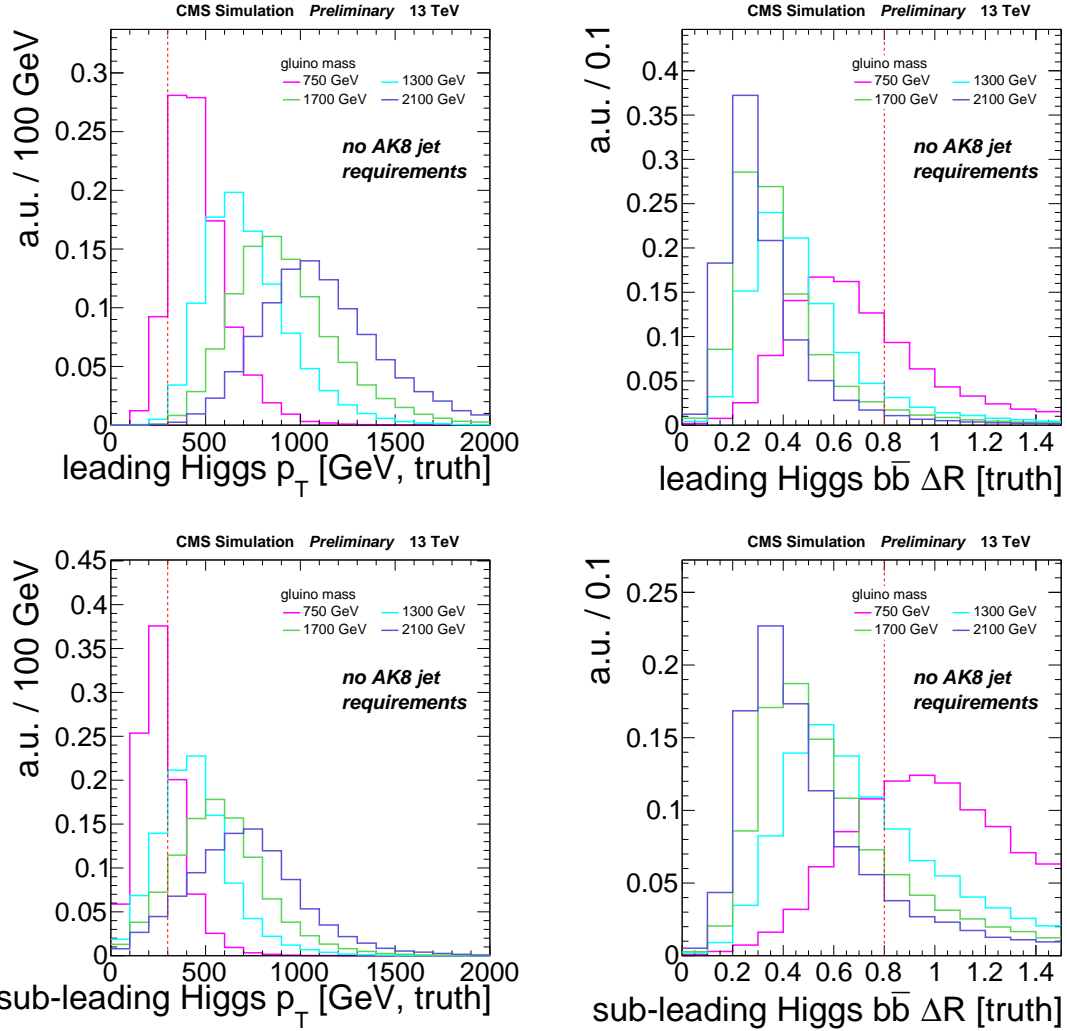


Figure 7.3: Generator level distributions for the highest (top row) and second highest (bottom row)  $p_T$  H boson in the T5HH model. The plot on the left shows the  $p_T$  of the H boson. The plot on the right shows  $\Delta R$  between the b-quark daughters - for large H  $p_T$  the daughters become collimated.

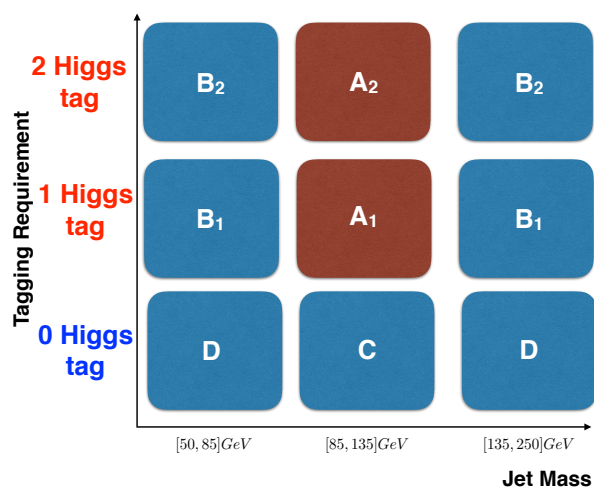


Figure 7.4: Partitioning of the signal and sideband regions for event binning. Additional binning in  $p_T^{\text{miss}}$  brings the total to 6x3=18.

Rearranging this gives a prediction for the events in the signal regions

$$A_{1,2}^{\text{predicted}} = \left( B_{1,2} \cdot \frac{C}{D} \right)^{\text{observed}} \quad (7.2)$$

The expected  $p_T^{\text{miss}}$  distribution from simulation is seen in the stacked histograms of Figure 7.5.

The prediction using the ABCD method on the same simulated samples is seen in the red hash. The performance of the method within simulation can be determined by dividing the true content in the signal region with the prediction. This ratio, denoted  $\kappa$ , is seen in the bottom panel of Figure 7.5.  $\kappa = 1$  represents perfect modeling. As will be discussed in Section 7.5.2,  $\kappa$  is used as a correction in the background estimation procedure.

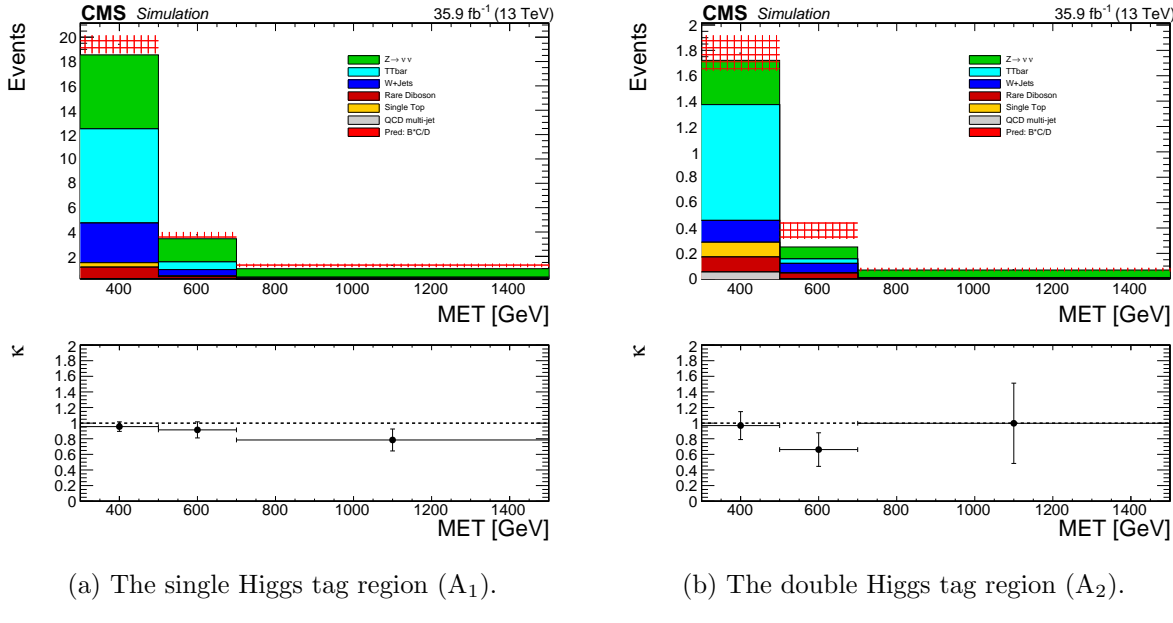


Figure 7.5:  $p_T^{\text{miss}}$  distributions and predictions in the signal regions using simulation only.

### 7.5.1 Control Regions within Data

We assume the background arises from three main sources:

- $Z \rightarrow \nu\bar{\nu}$  in which the neutrinos from the  $Z$  decay results in true  $p_T^{\text{miss}}$  ('Z-invisible').
- $W \rightarrow \ell\nu$  from direct  $W$  or top quark production in which the lepton  $\ell$  is not identified,

resulting in the event not being vetoed, and the associated neutrino from the leptonic decay creating true  $p_T^{\text{miss}}$  ('lost-lepton').

- Jet production via QCD in which the  $p_T$  of a jet is substantially under-measured, this creates a fake source of  $p_T^{\text{miss}}$ .

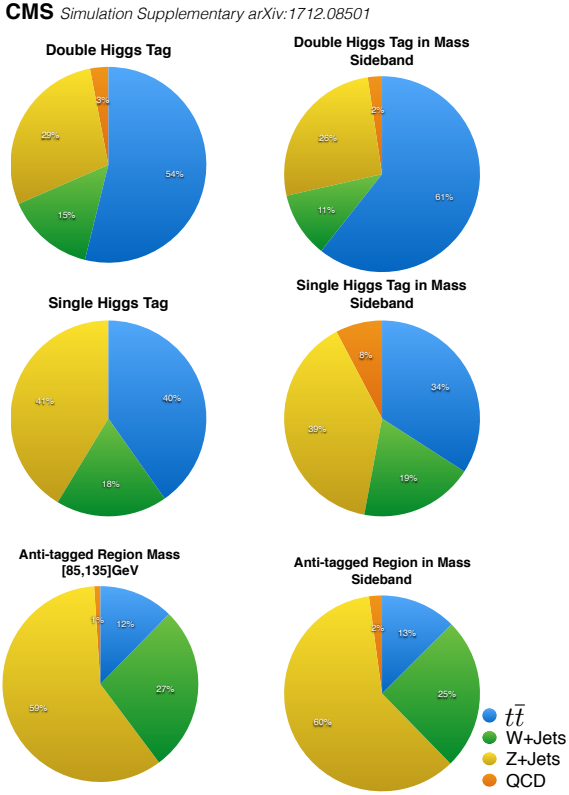


Figure 7.6: The fractional composition of expected SM backgrounds in the 6 analysis regions.

In order to study these backgrounds in data, we define three control regions which are expected to be enhanced in processes similar to the targeted background. The event selection is the same as applied to the nominal signal and sideband regions, but with some defining orthogonal condition:

- A control region with a single photon. For high- $p_T$ , photons and Z bosons are both massless, neutral, gauge bosons and therefore their kinematics are expected to be similar. “Artificial”

removal of the photon from the reconstruction (i.e. ignore its calorimeter deposit) results in event topologies phenomenologically similar to  $Z \rightarrow \nu\bar{\nu}$ .

- A control region with a single lepton. The topology of events from direct W or top quark production is the same regardless if the electron or muon is identified as such.
- A control region defined by the logical inversion of the low- $\Delta\phi$  cut. This explicitly selects events in which the AK4 jet momentum was likely under-measured, resulting in close alignment with  $p_T^{\text{miss}}$ .

As they are orthogonal to the analysis region, we are able to test the validity of the background estimation technique independently **within** each of the three control regions. By comparing the prediction of the yields using the ABCD method with those observed, the validity of the technique can be verified for that particular background category. The comparisons for the single-photon, single-lepton and low- $\Delta\phi$  control regions can be seen in Figure 7.7.  $\kappa$  in the bottom panel is defined as the ratio of the true event yield to the prediction.  $\kappa = 1$  represents the case in which the prediction perfectly matches the observation. These comparisons are used for commissioning of the background estimation technique only.

### 7.5.2 $\kappa$ as a Correction to the Estimation

A correction factor  $\kappa$  is applied to the prediction to account for the under-prediction of the background estimation procedure as observed in Figure 7.5.  $\kappa$  is obtained by dividing the yields for the signal region by that predicted:

$$\kappa \equiv A^{MC} / \left( B \cdot \frac{C}{D} \right)^{MC} \quad (7.3)$$

There are  $2 \times 3 = 6$  values of  $\kappa$ , one for each signal bin.  $\kappa = 1$  represents the case of a perfect prediction. The corrections are then applied as follows:

$$A_{1,2}^{\text{predicted}} = \kappa \cdot \left( B_{1,2} \cdot \frac{C}{D} \right)^{\text{observed}} \quad (7.4)$$

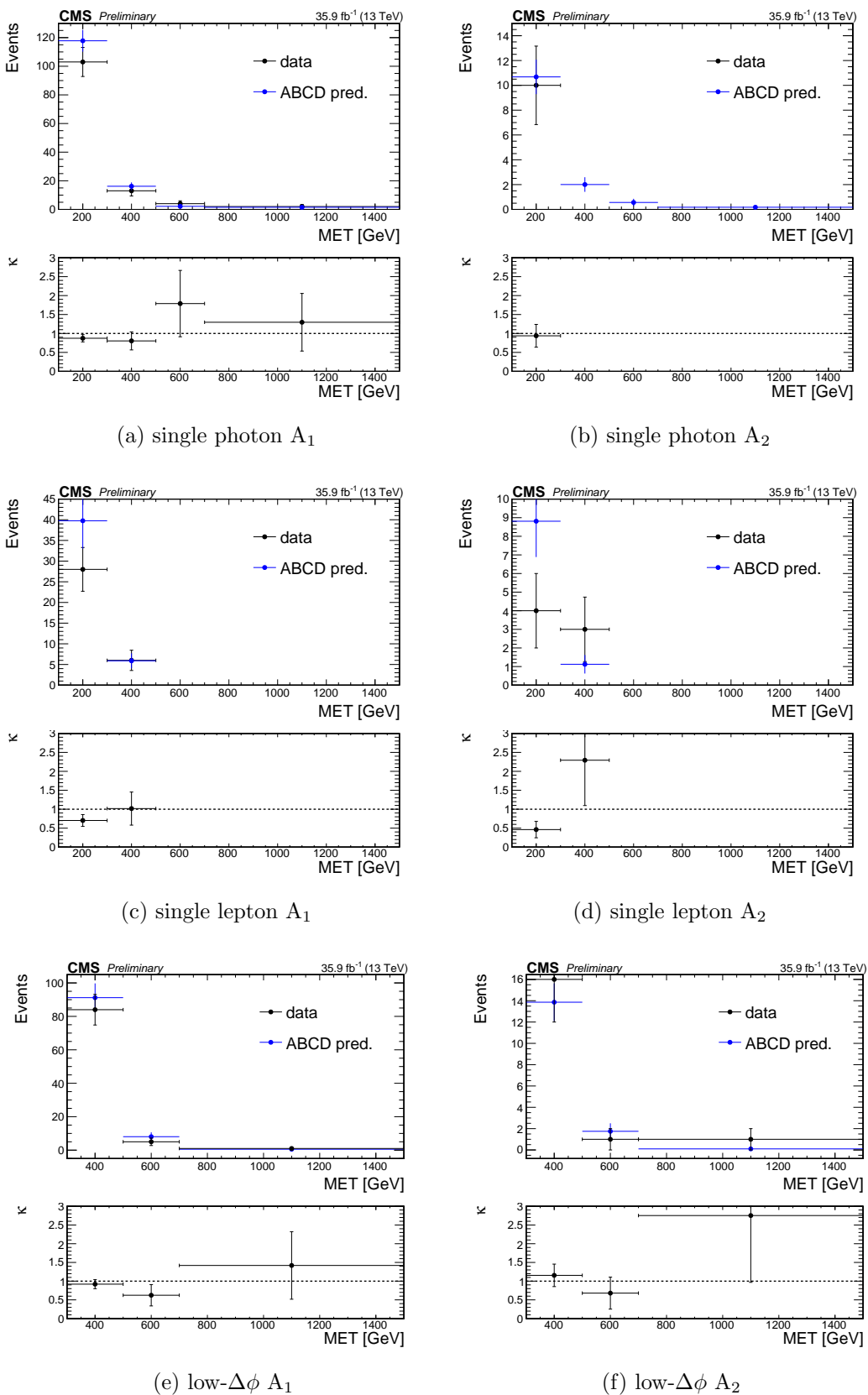


Figure 7.7: Comparisons of the predicted and observed yields within the data control regions.

These values of  $\kappa$  are those which we have already seen in Figure 7.5.

The value of  $\kappa$  is dependent on the yields of each analysis bin and is therefore sensitive to the accuracy of the modeling of in each of the 18 analysis bins. To improve the determination of  $\kappa$ , scale factors are derived using the data control regions to correct the normalization of in each of these bins. Different scale factors are assigned separately to the Z-invisible, lost-lepton, and QCD background samples. Rare processes (e.g. diboson) are taken directly from.

First consider how the yield  $N$  predicted by in an arbitrary bin (of 18) is the sum of the yields in the different datasets ( $t\bar{t}$  and  $W \rightarrow \ell\nu$  are grouped as they together represent the lost-lepton background):

$$N^{MC} = N_{Z \rightarrow \nu\bar{\nu}}^{MC} + N_{t\bar{t}, W \rightarrow \ell\nu}^{MC} + N_{QCD}^{MC} + N_{rare} \quad (7.5)$$

Scale factors are defined for this bin using the corresponding control regions in data and forming the ratio of events in simulation to that observed. They are then applied as follows:

$$N_{corrected}^{MC} = \left( \frac{N_{single-\gamma}^{data}}{N_{single-\gamma}^{MC}} \right) \cdot N_{Z \rightarrow \nu\bar{\nu}}^{MC} + \left( \frac{N_{single-\ell}^{data}}{N_{single-\ell}^{MC}} \right) \cdot N_{t\bar{t}, W \rightarrow \ell\nu}^{MC} + \left( \frac{N_{low-\Delta\phi}^{data}}{N_{low-\Delta\phi}^{MC}} \right) \cdot N_{QCD}^{MC} + N_{rare} \quad (7.6)$$

The  $p_T^{\text{miss}}$  distribution within the control regions is shown for both data and in Figures 7.8, 7.9, 7.10 for the single photon, single lepton, and low- $\Delta\phi$  control regions, respectively. The ratio in the bottom panel of each plot represents the scale factor for that  $p_T^{\text{miss}}$  bin. The dotted horizontal line shows the average scale factor inclusive in  $p_T^{\text{miss}}$ . The scale factors for the single-photon and low- $\Delta\phi$  control regions show no  $p_T^{\text{miss}}$  dependence and are determined integrated over  $p_T^{\text{miss}} > 300 \text{ GeV}$ . The values of the scale factors are summarized in Table 7.2. The Single-lepton region, shown in Figure 7.9, does show  $p_T^{\text{miss}}$  dependence and are summarized in Tables 7.2 and 7.3. In order to improve statistics for the single-lepton region, the low- $\Delta\phi$  requirement has been removed.

The scale factors are then applied to the samples to give yields which better reflect data. The  $p_T^{\text{miss}}$  distributions for the signal regions and expectations from the ABCD background prediction are seen in Figure 7.11 (the data-corrected version of Figure 7.5). The improved value of  $\kappa$  is seen

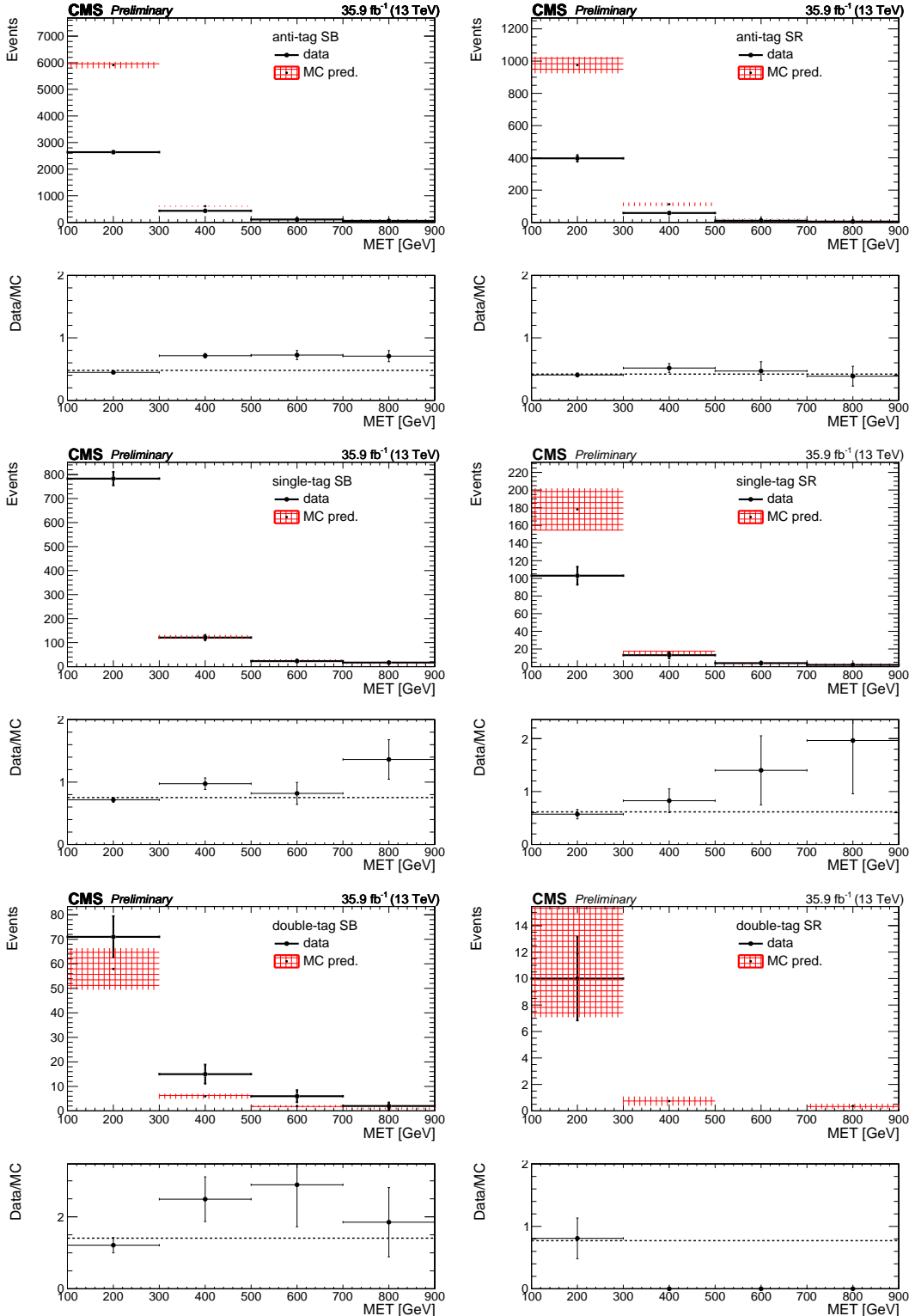


Figure 7.8: Signal and sideband yields in the single photon control region. The hashed red band denotes the prediction from simulation; the solid black points denote the observed yields in data. The Data/ ratio in the lower panel of each plot represents the scale factor for that bin.

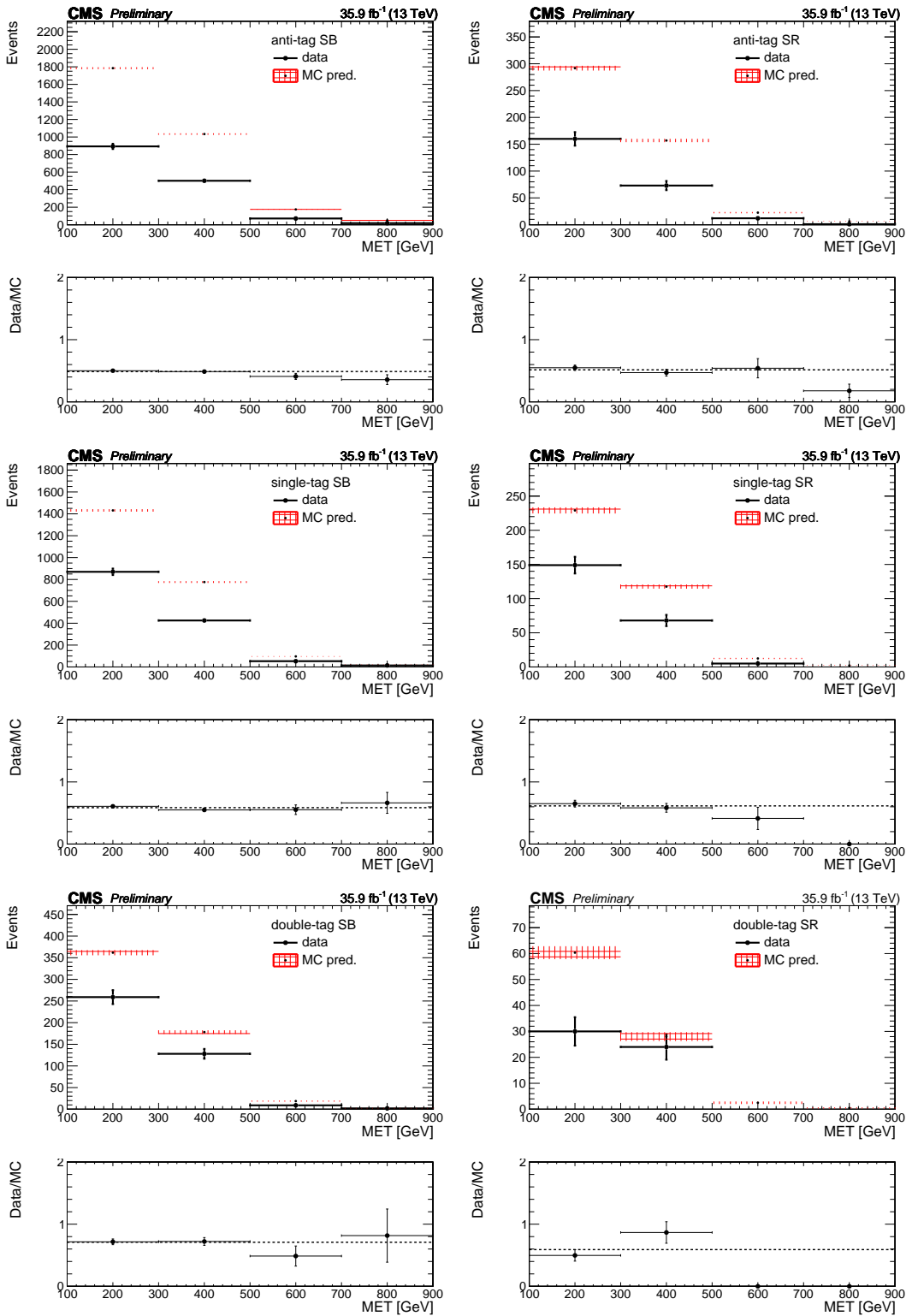


Figure 7.9: Signal and sideband yields in the single lepton control region. The hashed red band denotes the prediction from simulation; the solid black points denote the observed yields in data. The Data/ ratio in the lower panel of each plot represents the scale factor for that bin. The low- $\Delta\phi$  requirement has been removed to improve statistics.

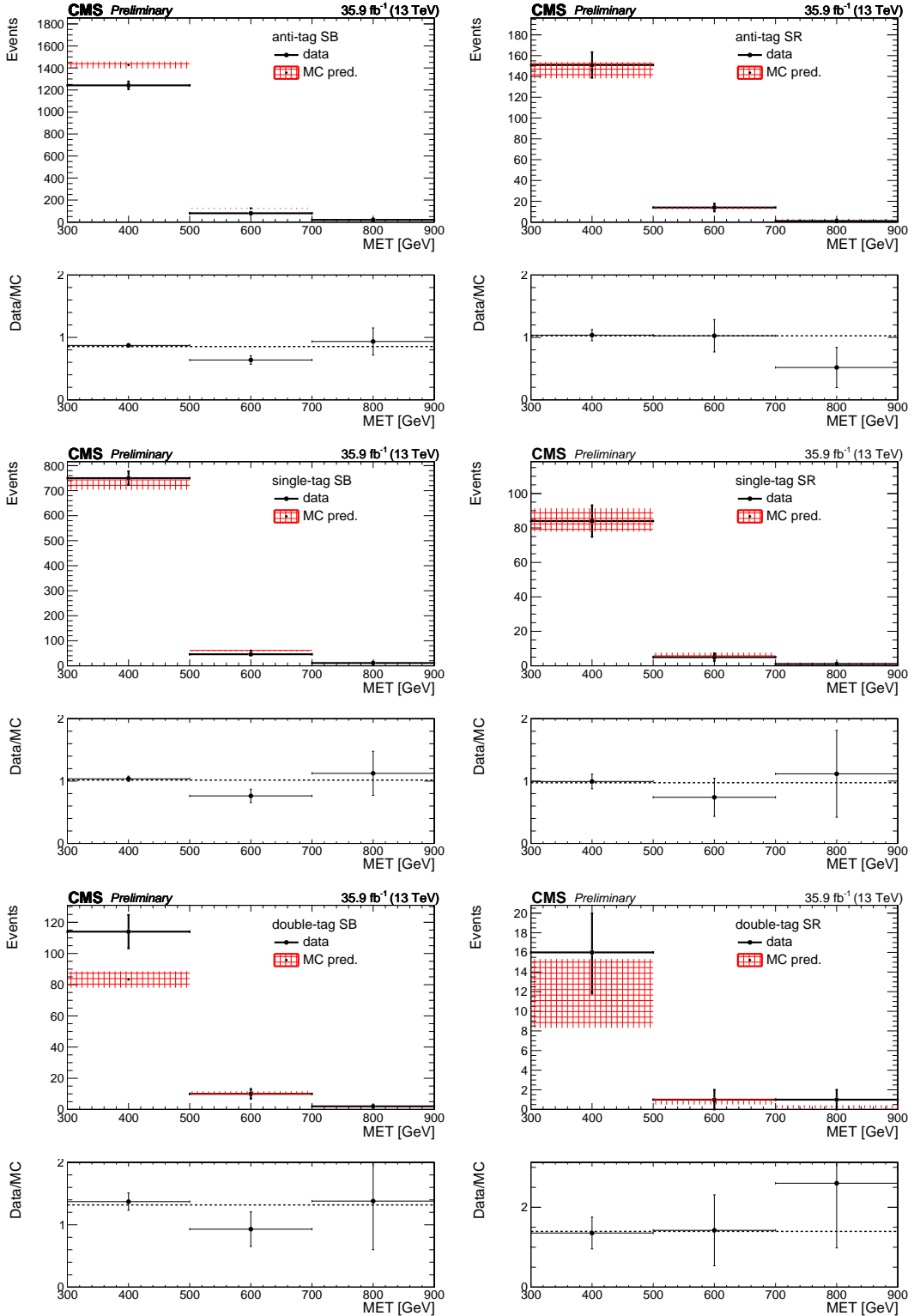


Figure 7.10: Signal and sideband yields in the the low- $\Delta\phi$  control region. The hashed red band denotes the prediction from simulation; the solid black points denote the observed yields in data. The Data/ ratio in the lower panel of each plot represents the scale factor for that bin.

Table 7.2: Summary of the control region scale-factors integrated over  $p_T^{\text{miss}}$ .

Low $\Delta\phi$					
$A_{SF}^{1H}$	$A_{SF}^{2H}$	$C_{SF}$	$B_{SF}^1$	$B_{SF}^2$	$D_{SF}$
$1.1 \pm 0.33$	$0.85 \pm 0.12$	$0.93 \pm 0.1$	$0.88 \pm 0.04$	$1.2 \pm 0.16$	$0.71 \pm 0.027$
Single Lepton					
$A_{SF}^{1H}$	$A_{SF}^{2H}$	$C_{SF}$	$B_{SF}^1$	$B_{SF}^2$	$D_{SF}$
$0.61 \pm 0.04$	$0.59 \pm 0.08$	$p_T^{\text{miss}}$ dependent	$0.59 \pm 0.016$	$0.71 \pm 0.04$	$p_T^{\text{miss}}$ dependent
Photon					
$A_{SF}^{1H}$	$A_{SF}^{2H}$	$C_{SF}$	$B_{SF}^1$	$B_{SF}^2$	$D_{SF}$
$0.61 \pm 0.088$	$0.75 \pm 0.29$	$0.5 \pm 0.07$	$0.98 \pm 0.094$	$2.58 \pm 0.63$	$0.71 \pm 0.035$

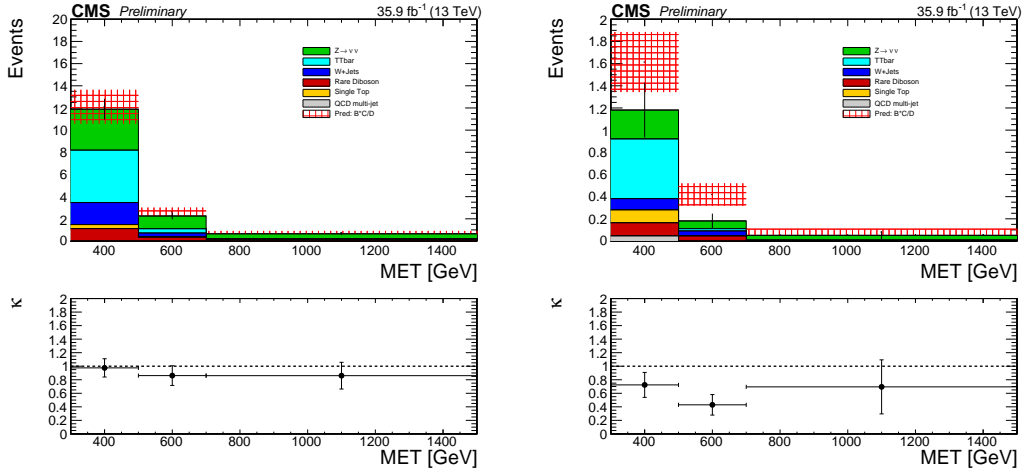
Table 7.3: Single lepton control region scale-factors in the anti-tag sideband region.

Single Lepton $C_{SF}$		
$p_T^{\text{miss}}$ [300, 500]	[500, 700]	[700, $\infty$ ]
$0.47 \pm 0.05$	$0.54 \pm 0.15$	$0.18 \pm 0.1$
Single Lepton $D_{SF}$		
$0.49 \pm 0.02$	$0.40 \pm 0.05$	$0.35 \pm 0.08$

in the lower panel of each plot. The modified values of the yields in the signal region (seen in the calculation of  $\kappa$ ) are seen in Tables 7.6 and 7.6. Since most of the scale factors are less than one the background decreases in Figure 7.5 relative to Figure 7.11 but still preserves the normalization so that  $\kappa$  is statistically compatible with unity. A distribution of  $\kappa$  is derived by throwing gaussian toys for each of the scale factors, the final results being summarized in Table 7.4.

Table 7.4: The  $\kappa$  factor computed by throwing Gaussian toys for the scale factors.

	1-Higgs Tag	2-Higgs Tag
$p_T^{\text{miss}}$	$\kappa$	
[300, 500 GeV]	$0.98 \pm 0.11$	$0.73 \pm 0.14$
[500, 700 GeV]	$0.86 \pm 0.16$	$0.43 \pm 0.12$
[700, $\infty$ GeV]	$0.86 \pm 0.17$	$0.62 \pm 0.30$



(a) The single Higgs tag region ( $A_1$ ).

(b) The double Higgs tag region ( $A_2$ ).

Figure 7.11: Signal region  $p_T^{\text{miss}}$  distributions using scale-factor corrected simulation.

Table 7.5: Corrected yields in the signal regions.  $\kappa = \text{AD} / \text{BC}$ 

$p_T^{\text{miss}}$	Z+Jets	W+Jets	TTbar	QCD	Rare	Total	Data
Region: $A^{1H}$							
[300, 500] GeV	3.76 ± 0.54	2.05 ± 0.30	4.87 ± 0.72	0 ± 0	1.48 ± 0.40	12.17 ± 1.03	15
[500, 700] GeV	1.18 ± 0.21	0.33 ± 0.08	0.40 ± 0.12	0 ± 0	0.39 ± 0.16	2.30 ± 0.29	2
> 700 GeV	0.43 ± 0.10	0.053 ± 0.025	0.046 ± 0.01	0 ± 0	0.13 ± 0.053	0.66 ± 0.12	1
Region: $A^{2H}$							
[300, 500] GeV	0.26 ± 0.12	0.11 ± 0.05	0.58 ± 0.21	0.045 ± 0.05	0.23 ± 0.12	1.24 ± 0.28	1
[500, 700] GeV	0.07 ± 0.045	0.049 ± 0.031	0.022 ± 0.0098	0 ± 0	0.045 ± 0.039	0.19 ± 0.068	0
> 700 GeV	0.044 ± 0.032	0.005 ± 0.005	0 ± 0	0 ± 0	0.002 ± 0.016	0.051 ± 0.036	0

Table 7.6: Corrected yields in the sideband regions.  $\kappa = \text{AD} / \text{BC}$ 

$p_T^{\text{miss}}$	Z+Jets	W+Jets	TTbar	QCD	Rare	Total	Data
Region: $C$							
[300, 500] GeV	17.66 ± 2.52	8.23 ± 1.44	3.87 ± 0.73	0.81 ± 0.49	2.78 ± 1.142	33.36 ± 3.24	44
[500, 700] GeV	5.20 ± 0.77	0.57 ± 0.27	0.22 ± 0.11	0 ± 0	0.63 ± 0.16	6.63 ± 0.84	12
> 700 GeV	2.48 ± 0.39	0.12 ± 0.12	0.028 ± 0.031	0 ± 0	0.14 ± 0.06	2.76 ± 0.41	4
Region: $B^{1H}$							
[300, 500] GeV	42.13 ± 4.17	15.61 ± 10.15	30.99 ± 20.15	1.57 ± 0.54	12.16 ± 1.37	102.47 ± 23.00	112
[500, 700] GeV	12.05 ± 1.28	2.74 ± 1.79	3.04 ± 2.00	0 ± 0	2.55 ± 0.43	20.37 ± 3.00	20
> 700 GeV	5.92 ± 0.69	0.67 ± 0.61	0.49 ± 0.46	0 ± 0	1.93 ± 0.72	9.01 ± 1.25	5
Region: $B^{2H}$							
[300, 500] GeV	5.51 ± 1.47	0.73 ± 0.44	4.46 ± 2.65	0.33 ± 0.23	2.06 ± 0.32	13.09 ± 3.09	13
[500, 700] GeV	1.80 ± 0.56	0.17 ± 0.11	0.59 ± 0.39	0 ± 0	0.62 ± 0.23	3.17 ± 0.73	1
> 700 GeV	0.67 ± 0.27	0.0084 ± 0.009	0.035 ± 0.031	0 ± 0	0.23 ± 0.073	0.94 ± 0.28	1
Region: $D$							
[300, 500] GeV	164.82 ± 8.31	61.24 ± 3.70	33.20 ± 2.16	8.50 ± 2.73	20.64 ± 1.78	288.41 ± 9.90	273
[500, 700] GeV	47.37 ± 2.52	6.36 ± 1.39	2.37 ± 0.55	0 ± 0	4.42 ± 1.46	60.51 ± 3.27	60
> 700 GeV	26.79 ± 1.50	0.99 ± 0.53	0.16 ± 0.086	0 ± 0	3.48 ± 1.01	31.42 ± 1.88	28

### 7.5.3 Sideband Yields & Predictions

Observed yields in data and the expectation for the 12 sideband bins (e.g.  $B_{1,2}$ ,  $C$ ,  $D$  in Figure 7.4) are seen in Figure 7.12. Table 7.7 lists these observed yields and calculated background prediction for the 6 signal bins.

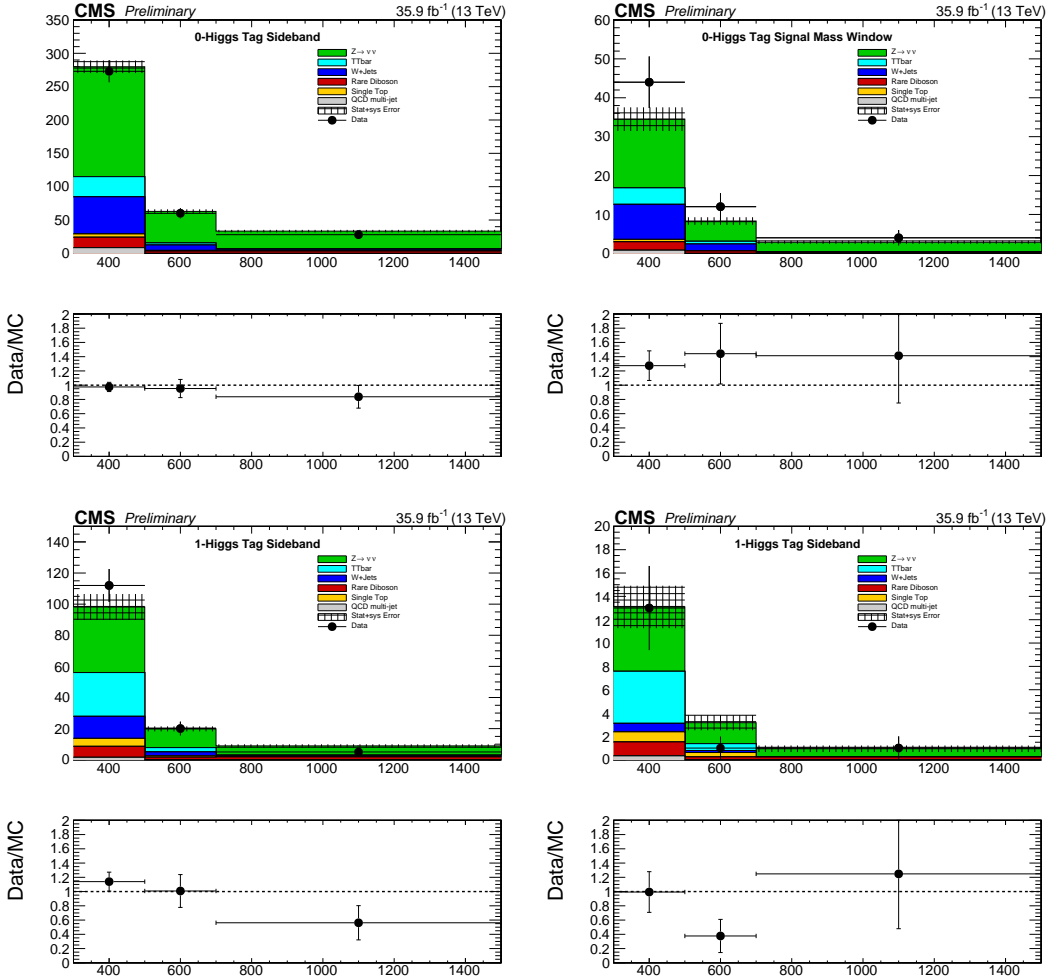


Figure 7.12: Control region  $p_T^{\text{miss}}$  distributions comparing data and scale-factor corrected simulation. The hashed red distribution denote the prediction from simulation; the solid points denote the observed yields in data.

## 7.6 Signal Systematics

We consider a variety of systematic uncertainties on the signal efficiency and distribution. Some are common to more inclusive SUSY analyses [32] and there are additional systematics related to  $b\bar{b}$  tagging efficiency and the effect of the pruned mass scale and resolution on the signal efficiency.

- **Luminosity:** The recommendation for the 2016 dataset is currently a flat uncertainty of 2.5%.
- **Isolated track veto:** A flat uncertainty of 2% is assigned to the signal samples to account for any data/ differences based on the study from the 2015 analysis [32].
- **statistics:** The sign fal sample statistical uncertainty is generally 2-4% .
- **Trigger efficiency:** The effect of the uncertainty on the signal yield is about 2%.
- **Pileup reweighting:** The sensitivity to the pileup distribution was studied for various benchmark signal models by comparing events with  $n_{\text{vtx}} < 20$  (low PU) or  $n_{\text{vtx}} \geq 20$  (high PU). Accordingly, no pileup reweighting is applied to the signal samples and no associated uncertainty is assessed.
- **ISR:** An ISR correction is derived from  $t\bar{t}$  events, with a selection requiring two lep- tons (electrons or muons) and two b-tagged jets, implying that any other jets in the event arise from ISR. The correction factors are 1.000, 0.920, 0.821, 0.715, 0.662, 0.561, 0.511 for  $\text{NISR} = 0, 1, 2, 3, 4, 5, 6+$ . The corrections are applied to the simulated signal jet samples with an

Table 7.7: Sideband region yields,  $\kappa$ , and background predictions for the 6 signal bins.

$N_H$	$p_T^{\text{miss}}$ (GeV)	B	C	D	$\kappa$	$\kappa \cdot B \cdot C/D$
$A_1$	[300, 500 GeV]	112	44	273	$0.98 \pm 0.11$	$17.7 \pm 3.8$
$A_1$	[500, 700 GeV]	20	12	60	$0.86 \pm 0.16$	$3.4 \pm 1.5$
$A_1$	[700, $\infty$ GeV]	5	4	28	$0.86 \pm 0.17$	$0.61 \pm 0.45$
$A_2$	[300, 500 GeV]	13	44	273	$0.73 \pm 0.14$	$1.52 \pm 0.57$
$A_2$	[500, 700 GeV]	1	12	60	$0.43 \pm 0.12$	$0.09 \pm 0.08$
$A_2$	[700, $\infty$ GeV]	1	4	28	$0.62 \pm 0.30$	$0.09^{+0.11}_{-0.09}$

additional normalization factor, typically 1.15 (depending on the signal model), to ensure the overall cross section of the sample remains constant. The systematic uncertainty in these corrections is chosen to be half of the deviation from unity for each correction factor. The effect on the yield ranges from 0.01%, with the largest effect at high  $p_T^{\text{miss}}$ .

- **Scales:** The uncertainty is calculated using the envelope of the weights from varying the renormalization and factorization scales,  $\mu_R$  and  $\mu_F$ , by a factor of 2 [33, 34]. The effect on the yield of is less than 0.1%.
- **Jet Energy Corrections:** The jet energy corrections (JECs) are varied using the  $p_T$ - and  $\eta$ -dependent jet energy scale uncertainties from the official database. These variations are propagated into the various jet-dependent variables, including:  $H_T$ , MET,  $\Delta\phi(\text{MET}, j_i)$ . The overall effect is less than 1%.
- **Jet Energy Resolution:** The jet momenta in the samples are smeared to match the jet energy resolution in data. The smearing factors are varied according to the uncertainties on the jet energy resolution measurements. These variations are propagated into the various jet-dependent variables, including:  $H_T$ , MET,  $\Delta\phi(\text{MET}, j_i)$ . The overall effect ranges from 0.01%.
- **PDFs:** The LHC4PDF prescription for the uncertainty on the total cross section is included as  $\pm 1$  sigma bands in the results plots. No additional uncertainty is considered for the uncertainty in the acceptance due to PDFs, as per SUSY group recommendation.

The above signal systematics are applied as an uncertainty on the signal normalization. These uncertainties are in general small. The main signal systematics come from the AK8 Jet Double-b tagging efficiency data/ scale factors and the uncertainty on the pruned mass resolution. The AK8 Jet Double-b tagging efficiency has an uncertainty which is propagated to the signal efficiency. This uncertainty is applied as a shape uncertainty across the Higgs tag regions and the anti-tag region. Also the pruned jet mass scale and resolution uncertainties are propagated to the final signal ef-

ficiency using POG recommendations. The pruned mass scale factor is derived using W-jets in semi-leptonic  $t\bar{t}$  and extrapolating to the H mass. This uncertainty is assigned a shape uncertainty on the signal mass window and the sideband.

- A data/ scale-factor is derived from double-muon tag data selected with HLT Trigger `HLT_BTagMu_AK8Jet300_Mu5_v` and muon enriched QCD Monte-Carlo. The scale factors have mainly a statistical error along with a smaller set of systematic errors due to shape systematics, Jet-Energy scale uncertainty, Pile-up corrections, uncertainty on the number of tracks, uncertainty of b-fragmentation and c-fragmentation, and the uncertainty on  $K_s$  and  $\Lambda$  fraction.
- The pruned mass scale-factor is derived by comparing the efficiency to select W-jets in data and within a mass window of [65, 85] GeV. The fit for the gaussian resolution of the W-mass peak is shown in Figure 7.13 and the fit results are shown in Table 7.8. The mass scale between and data is consistent though predicts a narrower mass resolution compared to data. The jet mass in each event is smeared to mimic the pruned jet mass resolution in data and an uncertainty is assigned based on the ratio of efficiencies between the smeared and un-smeared cases [35].

The summary of the signal systematics and their effect on the signal yields is shown in Table 7.9. The dominant effect is from the mass resolution uncertainty.

Table 7.8: Fit results for W-mass resolution in data and simulation.

	Data	$t\bar{t}$
Mean	$78.2 \pm 0.46$	$78.4 \pm 0.35$
Sigma	$10.10 \pm 0.67$	$7.23 \pm 0.48$

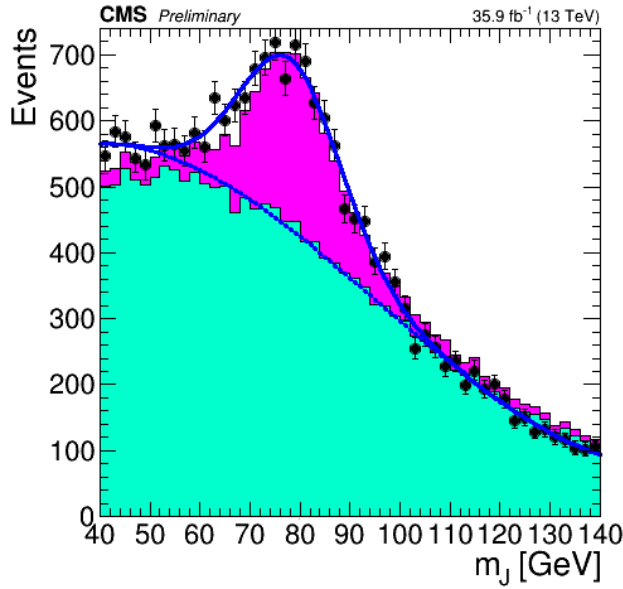


Figure 7.13: Pruned jet mass in semi-leptonic  $t\bar{t}$  events. The mass peak for the W-jets is used to derive the mass resolution uncertainty.

Unc. on Normalization	
Systematic	% Effect on yields
Luminosity	2.6%
Trigger Eff.	2.0%
Iso. Track Veto	2%
ISR modeling	0.01%
PDF Scale	0.1%
JEC	1%
JER	0.01%
Stat	1-4%
Shape Unc.	
Double-b SF	6%
Mass Resolution	1-15%

Table 7.9: Summary of signal shape and normalization uncertainties.

## 7.7 Results - Yields in the Signal Regions & Exclusion Curves

After unblinding the 4x3=12 sideband regions and performing the background estimation the 2x3=6 signal regions were unblinded. The observed yields, along with the background predictions, are seen in Table 7.10. Our signal region yields are consistent with the background expectation. Additionally, Table 7.10 shows the expected signal yields for two model points corresponding to gluino  $\tilde{g}$  masses of 2000 or 1800 GeV; the mass of the neutralino  $\tilde{\chi}_1^0$  is fixed at 1 GeV; the mass splitting between the gluino  $\tilde{g}$  and neutralino  $\tilde{\chi}_2^0$  is fixed at 50 GeV.

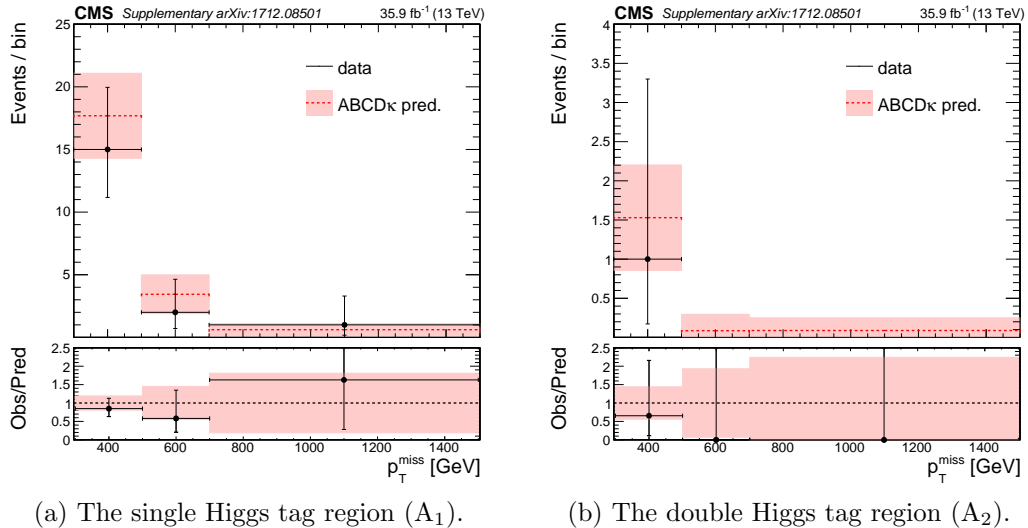


Figure 7.14: Observed yields in the signal regions.

Table 7.10: Signal yields and background predictions.

$p_T^{\text{miss}}$	$B \cdot C/D$	$\kappa$	$\kappa \cdot B \cdot C/D$	Obs.	T5HH(2000)	T5HZ(1800)
1-Higgs Tag						
[300, 500 GeV]	$18.05 \pm 3.39$	$0.98 \pm 0.11$	$17.68 \pm 3.85$	15	0.24	0.75
[500, 700 GeV]	$4 \pm 1.54$	$0.86 \pm 0.16$	$3.44 \pm 1.47$	2	0.32	0.98
[700, $\infty$ GeV]	$0.71 \pm 0.50$	$0.86 \pm 0.17$	$0.61 \pm 0.45$	1	2.13	4.34
2-Higgs Tag						
[300, 500 GeV]	$2.09 \pm 0.67$	$0.73 \pm 0.14$	$1.52 \pm 0.57$	1	0.17	0.35
[500, 700 GeV]	$0.2 \pm 0.20$	$0.43 \pm 0.12$	$0.09^{+0.08}_{-0.08}$	0	0.23	0.44
[700, $\infty$ GeV]	$0.14 \pm 0.16$	$0.62 \pm 0.30$	$0.09^{+0.11}_{-0.09}$	0	1.36	1.98

A visual representation of the one event in the double-H tagged signal bin is seen in Fig-

ure 7.15. The purple line represents  $p_T^{\text{miss}} = 426$  GeV. The three yellow cones represent the AK8 jets labeled with  $p_T$ . Note the two additional objects not satisfying our object definition but still plotted in the representation a) the additional low- $p_T$  and low mass AK8 jet b) the  $p_T=18$  GeV muon (red line) suffers from poor reconstruction properties.

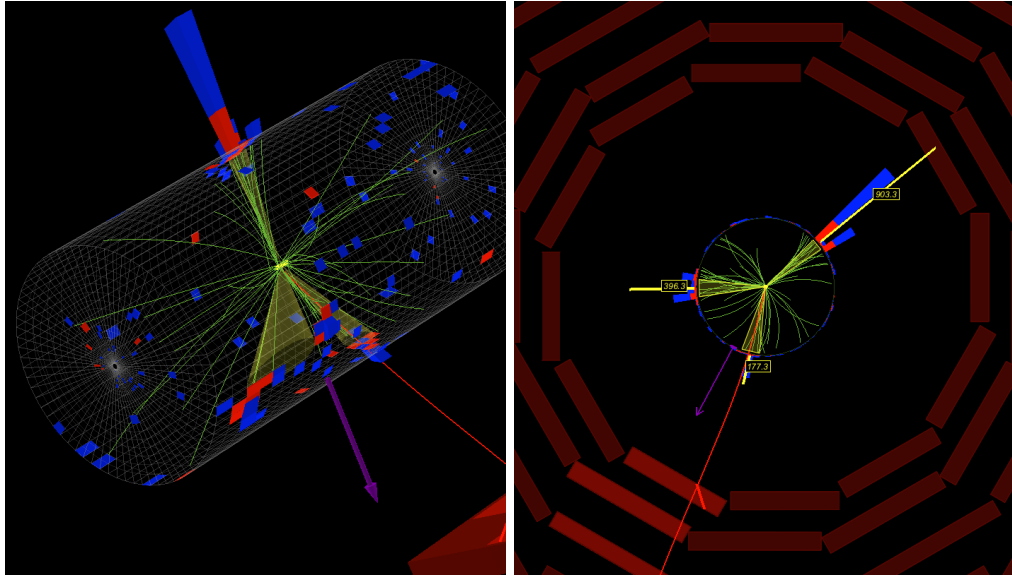


Figure 7.15: The single event in the  $A_2$  region.

Interpreting our results in the context of the T5HH or T5ZH models, the absence of signal allows us to place lower limits on the mass of the gluino  $\tilde{g}$ . For the statistical treatment, we use the Higgs combination tool to encode the ABCD approach in the likelihood. In this approach, the data card for one search bin contains the observed number of events and the expected signal and background in each of the ABCD regions. A likelihood function is built that contains these ABCD regions and explicitly encodes the relation  $A = \kappa B \frac{C}{D}$  and its uncertainty. The likelihood for each search bin can be described by:

$$\mathcal{L} = \prod_{i \in A, B, C, D} \text{Poisson}(n_i | bkg_i + r \cdot sig_i) \times \prod_j^{nuisances} \text{Constraints}(\theta_j, \hat{\theta}_j) \quad (7.7)$$

where the 4 regions are modeled by Poisson distribution and the term Constraints refers to either Gaussian distributions for the  $\kappa$  uncertainties or log normal distributions that model the

signal systematics. The expected and observed limits are then calculated based on approximations of the profile likelihood ratio using the CLs criterion to place limits at the 95% confidence level. These exclusion curves are seen in Figure 7.16. We are able to place lower limits at 95% confidence level on the gluino  $\tilde{g}$  mass at 2010 and 1825 GeV for the T5HH and T5ZH models, respectively. The weaker limit for the T5ZH model is due to the smaller branching fraction of the Z boson to b-quarks and our choice of signal mass window not being optimal for Z reconstruction.

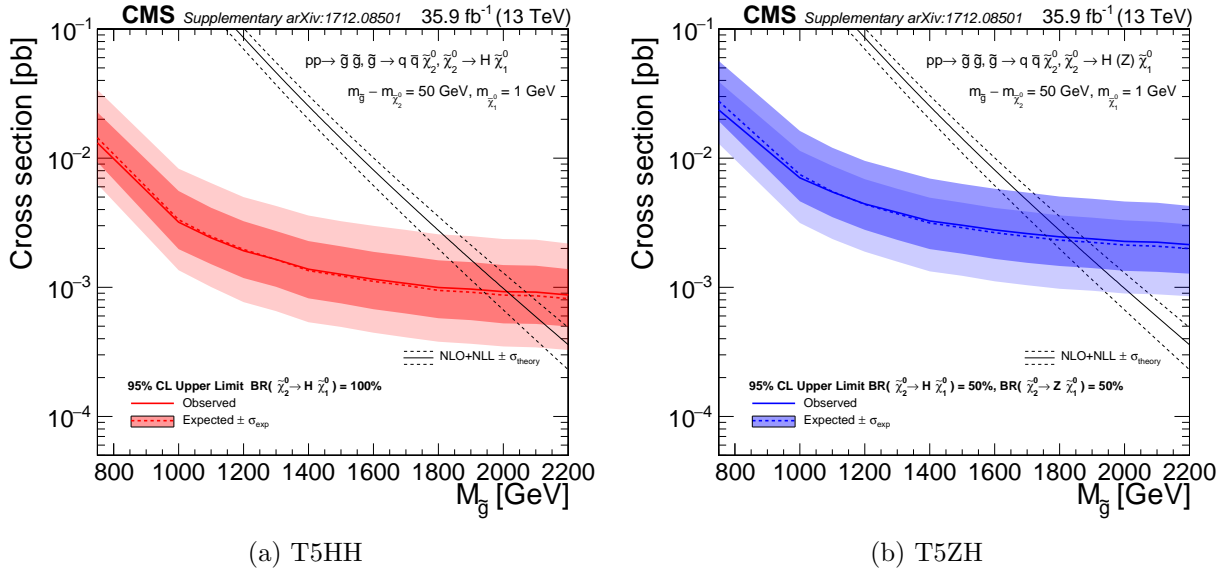


Figure 7.16: Observed and expected limits on the gluino cross section.

## Chapter 8

### Conclusions

This thesis has attempted to give a broad overview of the field of high-energy and collider-based particle physics. A brief introduction to the Standard Model was given in Chapter 2. This is a quantum field theory describing the fundamental particles and gauge-mediated interactions between them which govern the matter of our Universe; these particles were summarized in Figure 1.1b. In Chapter 3, we gave an overview of Supersymmetry, just one of many possible extensions to the SM which may in fact be realized in Nature. In Chapter 4 we gave a description of the Large Hadron Collider, the 27 km machine which houses a ring of two separate proton beams and provides the source of the high-energy proton-proton collisions. In Chapter 5 we gave a description of the CMS detector, an onion-like apparatus consisting of multiple layers of different particle detector technologies. Chapter 6 demonstrates how the hit information and data from the detector allows us to reconstruct the particles produced in the final states of these collisions. The SM is thus far able to provide a very good model of what we observe in these sorts of experiments.

We concluded in Chapter 7 of how an analysis of data collected by CMS is able to spot signs of physics beyond the Standard Model:

A search for physics beyond the SM was presented using events with boosted H bosons and missing transverse energy ( $p_T^{\text{miss}}$ ). The search targeted events with two or more wide-angle jets (AK8) being consistent with the decay of a boosted H or Z boson decaying to  $b\bar{b}$ .  $p_T^{\text{miss}}$  could potentially arise in the case a supersymmetric particle escapes detection. An ABCD method uses a sideband region to predict the the SM background in our signal region. Events are categorized

according to the  $b\bar{b}$  and mass tagging of the leading two AK8 jets in the event. The observed yields in the 6 signal bins are statistically compatible with the SM background expectation and no excess of events is observed. We use these results to set limits on the gluino mass for the SUSY-inspired T5HH or T5ZH models. For the T5HH model we are able to exclude gluino masses below 2010 GeV at 95% confidence level. This is with the assumption the NLSP mass is 50 GeV less than the gluino mass and that the LSP has a mass of 1 GeV. The work presented here has been published in Phys. Rev. Lett. [36].

## Appendix A

### Reinterpretation

In Section 7.7, we presented our observed yields in the signal region and found they were consistent with the background expectations. We chose to apply these results

In light of this, we set upper limits esented in the context of setting lower limits on the mass of gluinos in a supersymmetric model.

mass for specific the T5HH and T5ZH models. Many such SMS models exist within the MSSM which predict the production of high- $p_T$  bosons and it is therefore important to include information necessary to make predictions of yields for different final states. This is aided by providing the interested party with efficiencies for  $b\bar{b}$  tagging and mass tagging of the AK8 jets. Tagging efficiencies for the five largest decay modes relevant to the analysis for the H boson are seen in A.1. Tagging efficiencies for the hadronic decay modes of the Z boson are seen in Figure A.2, the much lower mass tagging efficiency for the Z boson is due to our choice of signal mass window [85, 135 GeV] not being optimal for Z boson reconstruction. These are used to calculate the expected yields in the 6 analysis regions when performing a reinterpretation of the analysis using different final states.

For each event, the yield in each bin can be predicted by first forming the following weights using the tagging efficiencies for the two highest  $p_T$  AK8 jets as seen below.  $j0$  and  $j1$  represent the highest and second highest  $p_T$  AK8 jet, respectively. The weights on the right-hand-side are  $p_T$  dependent.

- double mass tag weight =  $j0_{signalmass} \cdot j1_{signalmass}$

- anti mass tag weight =  $(j0_{sidebandmass} \cdot j1_{signalmass}) + (j1_{signalmass} \cdot j1_{sidebandmass}) + (j0_{sidebandmass} \cdot j1_{sidebandmass})$
- double bb tag weight =  $j0_{bbtag} \cdot j1_{bbtag}$
- single bb tag weight =  $(j0_{bbtag} \cdot (1 - j1_{bbtag})) + ((1 - j0_{bbtag}) \cdot j1_{bbtag})$
- anti bb tag weight =  $(1 - j0_{bbtag}) \cdot (1 - j1_{bbtag})$

These weights are then combined in the following manner to determine the yields across each of the 6 bins for a single event.

$$(1) \text{ A1 weight} = (\text{single bb tag weight}) \cdot (\text{double mass tag weight})$$

$$(2) \text{ A2 weight} = (\text{double bb tag weight}) \cdot (\text{double mass tag weight})$$

$$(3) \text{ B1 weight} = (\text{single bb tag weight}) \cdot (\text{anti mass tag weight})$$

$$(4) \text{ B2 weight} = (\text{double bb tag weight}) \cdot (\text{anti mass tag weight})$$

$$(5) \text{ C weight} = (\text{anti bb tag weight}) \cdot (\text{double mass tag weight})$$

$$(6) \text{ D weight} = (\text{anti bb tag weight}) \cdot (\text{anti mass tag weight})$$

These weights for the 6 analysis bins (inclusive in  $p_T^{\text{miss}}$ ) are then summed over all events to get the expected yields. The prescription was tested using the T5HH model with a gluino mass of 2200 GeV and compared it to the true value. The largest deficit was in the D region, with a difference of -36% difference from nominal. The greatest over-prediction is found in the B2 region, with a surplus of +8.2% events relative to nominal. The closure in the other bins fall somewhere in this range. These results are summarized in Table A.1. As a further cross-check to the yield estimates, Table A.2 shows the true signal event efficiencies for the T5HH model with a gluino mass of 2200 GeV.

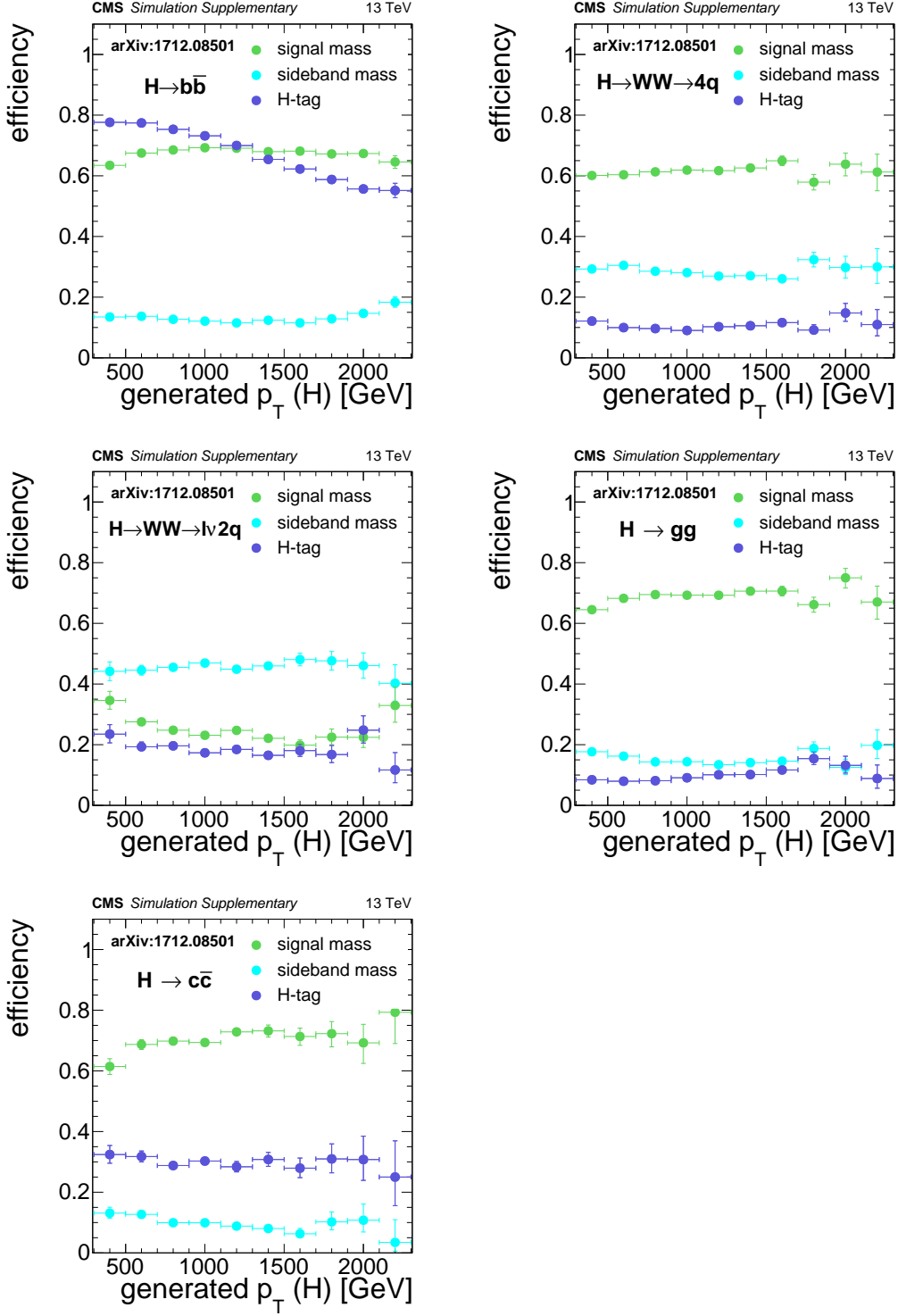


Figure A.1: Efficiencies for an AK8 jet originating from H boson decay, relative to baseline selection. "signal mass" represents the probability the jet will have mass [85, 135 GeV]. "sideband mass" represents the probability the jet will have mass [50, 85 GeV] or [135, 250 GeV]. "H-tag" represents the probability the jet have a double-b discriminator value greater than 0.3, for jets with mass [50, 250 GeV]. Efficiencies were derived using the T5ZH with a gluino mass of 2200 GeV.

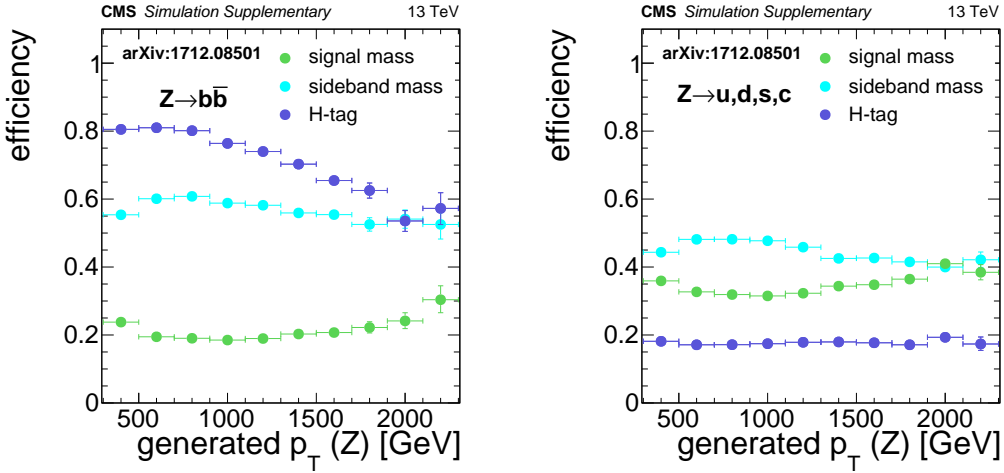


Figure A.2: Efficiencies for an AK8 jet originating from Z boson decay, relative to baseline selection. "signal mass" represents the probability the jet will have mass [85, 135 GeV]. "sideband mass" represents the probability the jet will have mass [50, 85 GeV] or [135, 250 GeV]. "H-tag" represents the probability the jet have a double-b discriminator value greater than 0.3, for jets with mass [50, 250 GeV]. Efficiencies were derived using the T5ZH with a gluino mass of 2200 GeV.

Table A.1: Comparison of the true reco-level event yield with those obtained via the prediction. The columns with the RECO or GEN labels are the prediction using RECO or GEN event variables only, respectively. The prediction was made using the T5HH with a gluino mass of 2200 GeV.

	RECO "truth"	RECO prediction	GEN prediction
Baseline	4.08	3.46 (-15%)	3.53 (-16%)
A1	1.21	1.18 (-2.3%)	1.26 (+3.6%)
A2	0.777	0.748 (-3.7%)	0.815 (+4.7%)
B1	0.802	0.703 (-12%)	0.664 (-21%)
B2	0.322	0.338 (+5.0%)	0.350 (+8.2%)
C	0.498	0.473 (-4.9%)	0.487 (-2.1%)
D	0.478	0.353 (25%)	0.308 (-36%)

Table A.2: Signal efficiencies for an event to land in a given analysis bin. The efficiencies were derived using the T5HH with a gluino mass of 2200 GeV. Choosing a gluino mass of 1800 GeV decreases the efficiencies by a relative 5%.

	Baseline	A1	A2	B1	B2	C	D
$p_T^{\text{miss}} < 300 \text{ GeV}$	32%	9.4%	6.0%	6.2%	2.5%	3.9%	3.7%
$300 < p_T^{\text{miss}} < 500 \text{ GeV}$	2.7%	0.78%	0.52%	0.54%	0.25%	0.31%	0.30%
$500 < p_T^{\text{miss}} < 700 \text{ GeV}$	3.5%	1.0%	0.65%	0.72%	0.28%	0.43%	0.40%
$p_T^{\text{miss}} > 700 \text{ GeV}$	26%	7.6%	4.9%	5.0%	2.0%	3.1%	3.0%

Table A.3: T5HH and T5ZH signal efficiencies cutflow for two different gluino masses. The first row represents no selection, the final row represents the selection for the “A<sub>2</sub>” signal event bin of the main analysis (inclusive in  $p_T$ ).

	Model	HH 1300	HH 2200	ZH 1300	ZH 2200
	Gluino mass (GeV)				
	Total yield at 35.9 fb <sup>-1</sup>	1660	12.8	1651	12.9
+	Lepton & isolated track vetoes	1253	10.1	1277	10.3
+	$\Delta\phi_{1,2,3,4}$	1037	8.3	1049	8.4
+	HT > 600 & $p_T^{\text{miss}} > 300$ GeV	886	7.8	834	7.6
+	$\geq 2$ AK8 jets with $p_T > 300$ GeV	602	6.5	523	5.4
+	Jet 1,2 mass $\epsilon$ [50, 250 GeV]	374	4.1	313	3.3
+	Jet 1,2 mass $\epsilon$ [85, 135 GeV]	209	2.5	101	1.0
+	One or two H-tags	168	2.0	67	0.6

## Appendix B

### $b\bar{b}$ -tagging Scale Factors for W jets in $t\bar{t}$ Events

Boosted W bosons can arise in many models of beyond the SM physics. The 67.41% branching fraction of  $W \rightarrow$  hadrons make their reconstruction as AK8 jets an efficient channel. Although W bosons do not decay to b-quarks (the top quark is too heavy), the  $b\bar{b}$ -tagger has a non-zero probability to tag one of these jets as having decayed to a  $b\bar{b}$  pair. This *mistag* rate can, in principle, be different in simulation compared to in data. Depending on the use, it may be necessary to apply *scale factors* to the simulation to correct for this difference. By using a sample of AK8 jets identified as W bosons in semi-leptonic  $t\bar{t}$  events, we can calculate the mistag rate in both data and simulation, taking their ratio to form the scale factors.

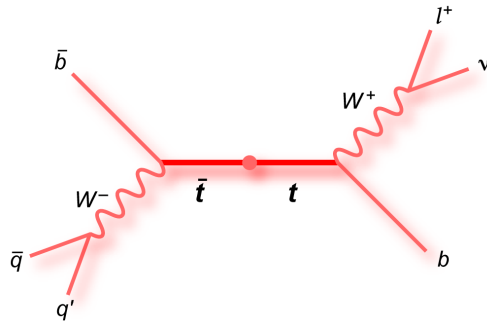


Figure B.1: A diagram of a semi-leptonic  $t\bar{t}$  event in the center-of-mass frame [37].

Semi-leptonic  $t\bar{t}$  events, as in Figure B.1, are selected by requiring a single muon ( $p_T > 50$  GeV,  $|\eta| < 2.1$ ) within close proximity ( $\Delta\phi < \frac{2}{3}\pi$ ) of a loose-b-tagged AK4 jet ( $p_T > 30$  GeV,  $|\eta| < 2.4$ ). Opposite this muon ( $\Delta\phi > \frac{2}{3}\pi$ ) we require at least one AK8 jet ( $p_T > 250$  GeV,  $|\eta| < 2.4$ ) and at least one AK4 jet. The AK8 jet is to be reconstructed as the W boson. Events

are triggered in data by requiring a  $p_T > 50$  GeV muon at HLT. Three additional selections are applied to ensure a high purity sample:

- The AK8 jet must be consistent with having a two-jet substructure (using a quantity called “n-subjettiness” [38, 39]).
- The AK8 jet must have a mass within the window [50, 200 GeV]. Jets from QCD tend to have low mass.
- To minimize contamination from nearby objects, no AK4 jets are allowed with  $\Delta R < 0.8$  of the reconstructed W.

The purity of the sample can be seen on the left in Figure B.2, a plot of the AK8 jet mass - the distribution is centered near  $m_W = 80.385$  GeV. A small contribution near  $m_{top} = 172.44$  GeV arises from the merging of a W and b quark into a single AK8 jet.

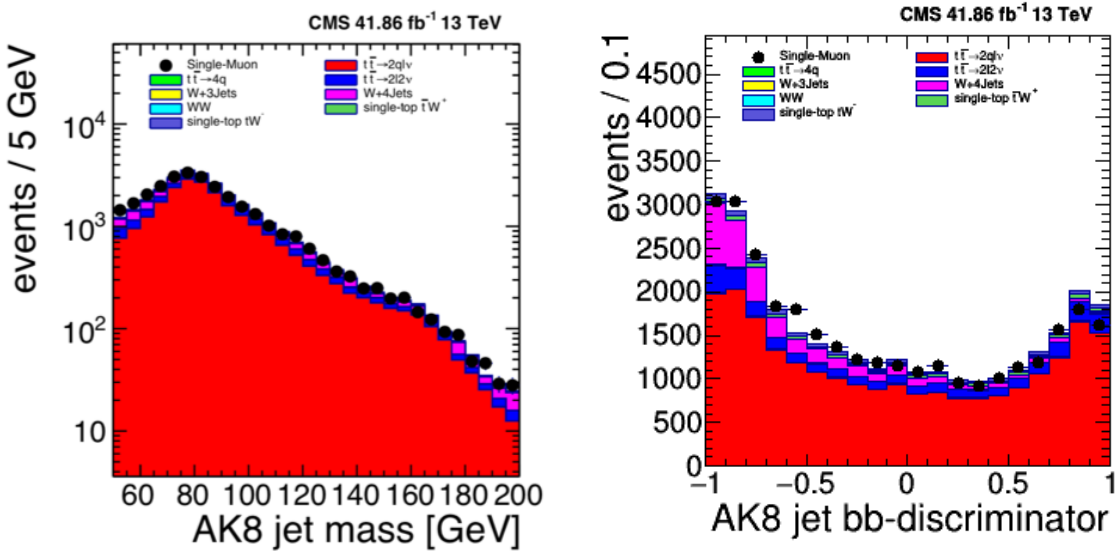


Figure B.2: W jet mass and  $b\bar{b}$ -tagging discriminator in data and simulation. Simulation is scaled to match the data normalization.

The right side of Figure B.2 shows the distribution of the  $b\bar{b}$ -tagging discriminator for data and simulation. For a given working point (i.e. a fixed point along the x-axis of the figure), the

mistag rate in  $t\bar{t}$  MC (inclusive in all decays) is defined as the number of jets with a discriminator greater than that value, divided by the total number of jets. In data, the observed yields are first corrected by a subtraction of the expected prompt W and single-top background estimated from simulation. Equation B.1 summarizes these equations:

$$\epsilon_{mc} = \frac{N_{bb\text{-tagged}}^{sig,mc}}{N^{sig,mc}}, \quad \epsilon_{data} = \frac{N_{bb\text{-tagged}}^{data} - N_{bb\text{-tagged}}^{bkg,mc}}{N^{data} - N^{bkg,mc}}, \quad \text{scale factor} = \frac{\epsilon_{data}}{\epsilon_{mc}} \quad (\text{B.1})$$

Following this prescription, we obtain the mistag rates in data and simulation seen in Table B.1. Four working points are defined ranging from  $\text{disc}>0.3$  to  $\text{disc}>0.9$ . It is seen that the mistag rate in MC is higher for all working points than in data. This trend can be seen in the right-hand plot of Figure B.2 - the MC under-predicts the yields with low discriminator value, and over-predicts those with a large discriminator value.

Table B.1: W jet  $b\bar{b}$  mistag rates in data and simulation, inclusive in  $p_T$ . Errors are statistical only.

working point	data	MC
disc > 0.3	$0.326 \pm 0.003$	$0.340 \pm 0.003$
disc > 0.6	$0.219 \pm 0.003$	$0.236 \pm 0.002$
disc > 0.8	$0.122 \pm 0.002$	$0.138 \pm 0.002$
disc > 0.9	$0.058 \pm 0.001$	$0.067 \pm 0.001$

The scale factors are then formed by taking the ratio of the mistag rate in data to that of simulation. Table B.2 shows the scale factors, binned in jet  $p_T$ , for the four different working points. The errors shown arise from the quadrature sum of the statistical and two additional systematic errors: uncertainty in the normalization of the prompt-W background MC, and the effect of reweighting the  $t\bar{t}$  MC to better match the top  $p_T$  spectra observed in data [40]. The size of the error from the prompt-W MC normalization is estimated by scaling the MC  $\pm 30\%$ , we assign an absolute 2, 4, 6% uncertainties for the low, medium, and high  $p_T$  bins, respectively. The error due to the top  $p_T$  re-weighting is estimated by taking the difference in scale factors with and without the weights. We assign an absolute error of 0, 1, 2% to the low, medium, and high  $p_T$  bins, respectively.

Table B.2: Summary of scale factors for  $b\bar{b}$ -tagging W jets in  $t\bar{t}$  events.

working point	$250 < p_T < 350 \text{ GeV}$	$350 < p_T < 430 \text{ GeV}$	$p_T > 430 \text{ GeV}$
disc > 0.3	$0.939 \pm 0.026$	$1.007 \pm 0.055$	$0.996 \pm 0.079$
disc > 0.6	$0.922 \pm 0.027$	$0.967 \pm 0.057$	$0.902 \pm 0.082$
disc > 0.8	$0.875 \pm 0.030$	$0.939 \pm 0.063$	$0.893 \pm 0.090$
disc > 0.9	$0.855 \pm 0.036$		$0.914 \pm 0.068$

## Bibliography

- [1] CMS Collaboration, “Observation of a new boson at a mass of 125 GeV with the CMS experiment at the LHC,” *Phys. Lett. B*, vol. 716, pp. 30–61, September 2012. arXiv:1207.7235.
- [2] S. P. Martin, “A Supersymmetry Primer,” pp. 58–60, January 2016. arXiv:hep-ph/9709356.
- [3] J. Wess and B. Zumino, “Supergauge transformations in four dimensions,” , 1974. arXiv:0910.5530.
- [4] CMS Collaboration, “Search for supersymmetry in multijet events with missing transverse momentum in proton-proton collisions at 13 TeV,” *Phys. Rev. D*, vol. 96, p. 032003, 2017. arxiv:1704.07781.
- [5] CMS Collaboration, “Search for supersymmetry in the multijet and missing transverse momentum final state in pp collisions at 13 TeV,” *Phys. Lett. B*, vol. 758, p. 152, 2016. arXiv:1602.06581.
- [6] CMS Collaboration, “The CMS Tracker Project: Technical Design Report,” 1997. CERN-LHCC-98-006 ; CMS-TDR-5.
- [7] CMS Collaboration, “The CMS Tracker Project: Addendum to the Technical Design Report,” 2000. CERN-LHCC-2000-016 ; CMS-TDR-5-add-1.
- [8] D. A. Matzner Dominguez, D. Abbaneo, K. Arndt, N. Bacchetta, A. Ball, E. Bartz, W. Bertl, G. M. Bilei, G. Bolla, H. W. K. Cheung, *et al.*, “CMS Technical Design Report for the Pixel Detector Upgrade,” , September 2012. CERN-LHCC-2012-016 ; CMS-TDR-11.
- [9] CMS Collaboration, “The CMS Electromagnetic Calorimeter Project: Technical Design Report,” 1997. CERN-LHCC-97-033 ; CMS-TDR-4.
- [10] P. Bloch, R. Brown, P. Lecoq, and H. Rykaczewski, “The CMS Electromagnetic Calorimeter Project: Addendum to the Technical Design Report,” 2002. CERN-LHCC-2002-027 ; CMS-TDR-4-add-1.
- [11] CMS Collaboration, “The CMS Hadron Calorimeter Project: Technical Design Report,” 1997. CERN-LHCC-97-031 ; CMS-TDR-2.
- [12] N. Strobbe, “The upgrade of the CMS hadron calorimeter with silicon photomultipliers,” *JINST*, vol. 12, January 2017. FERMILAB-CONF-16-501-CMS-E.

- [13] CMS Collaboration, “Performance of the CMS Hadron Calorimeter with Cosmic Ray Muons and LHC Beam Data,” *JINST*, vol. 5, March 2010. arXiv:0911.4991.
- [14] CMS Collaboration, “The CMS Magnet Project: Technical Design Report,” 1997. CERN-LHCC-97-010 ; CMS-TDR-1.
- [15] CMS Collaboration, “Precise Mapping of the Magnetic Field in the CMS Barrel Yoke using Cosmic Rays,” . arXiv:0910.5530.
- [16] CMS Collaboration, “The CMS Muon Project: Technical Design Report,” 1997. CERN-LHCC-97-032 ; CMS-TDR-3.
- [17] CMS Collaboration, “Performance of the CMS Drift Tube Chambers with Cosmic Rays,” *JINST*, vol. 5, March 2010. arXiv:0911.4855.
- [18] CMS Collaboration, “The performance of the CMS muon detector in proton-proton collisions at  $\sqrt{s} = 7$  TeV at the LHC,” *JINST*, vol. 8, November 2013. arXiv:1306.6905.
- [19] CMS Collaboration, “Performance of the CMS cathode strip chambers with Cosmic Rays,” *JINST*, vol. 5, March 2010. arXiv:0911.4992.
- [20] Costantini et al., “Uniformity and Stability of the CMS RPC Detector at the LHC,” *JINST*, vol. 8, 2013. arXiv:1209.1989.
- [21] CMS Collaboration, “The CMS trigger system,” *JINST*, vol. 12, p. 01020, 2017. arXiv:1609.02366.
- [22] CMS Collaboration, “Description and performance of track and primary-vertex reconstruction with the CMS tracker,” *JINST*, vol. 9, October 2014. arXiv:1405.6569.
- [23] CMS Collaboration, “Particle-flow reconstruction and global event description with the CMS detector,” *JINST*, vol. 12, p. 10003, 2017. arXiv:1706.04965.
- [24] M. Cacciari, G. P. Salam, and G. Soyez, “The anti-kt jet clustering algorithm,” *JHEP*, no. 04, p. 063, 2008. arXiv:0802.1189.
- [25] CMS Collaboration, “Identification of double-b quark jets in boosted event topologies,” 2016. CMS-PAS-BTV-15-002.
- [26] CMS Collaboration, “Interpretation of searches for supersymmetry with simplified models,” *Phys. Rev. D*, vol. 88, p. 2017, 24 2013. arXiv:1301.2175.
- [27] CMS Collaboration, “Search for supersymmetry in pp collisions at  $\sqrt{s} = 13$  TeV in the single-lepton final state using the sum of masses of large-radius jets,” *JHEP*, August 2016. arXiv:1605.04608.
- [28] J. Alwall, R. Frederix, S. Frixione, V. Hirschi, F. Maltoni, O. Mattelaer, H.-S. Shao, T. Stelzer, P. Torrielli, and M. Zaro, “The automated computation of tree-level and next-to-leading order differential cross sections, and their matching to parton shower simulations,” *JHEP*, vol. 07, p. 079, 2014. arXiv:1405.0301.
- [29] R. D. Ball *et al.*, “Parton distributions for the LHC Run II,” *JHEP*, vol. 04, p. 040, 2015. arXiv:1410.8849.

- [30] T. Sjstrand, S. Ask, J. R. Christiansen, R. Corke, N. Desai, P. Ilten, S. Mrenna, S. Prestel, C. O. Rasmussen, and P. Z. Skands, “An introduction to PYTHIA 8.2,” *Computer Physics Communications*, vol. 191, pp. 159–177, June 2015. arXiv:1410.3012.
- [31] S. Agostinelli et al., “GEANT4—a simulation toolkit,” *Nucl. Instrum. Meth. A*, vol. 506, p. 250, July 2003. [https://doi.org/10.1016/S0168-9002\(03\)01368-8](https://doi.org/10.1016/S0168-9002(03)01368-8).
- [32] CMS Collaboration, “Search for supersymmetry in multijet events with missing transverse momentum in proton-proton collisions at 13 TeV,” CMS AN-16-350.
- [33] M. Cacciari, S. Frixione, M. L. Mangano, P. Nason, and G. Ridolfi, “The  $t\bar{t}$  cross-section at 1.8 TeV and 1.96 TeV: A Study of the systematics due to parton densities and scale dependence,” *JHEP*, vol. 4, no. 2004, p. 068, 2004. arXiv:hep-ph/0303085.
- [34] S. Catani, D. de Florian, M. Grazzini, and P. Nason, “Soft gluon resummation for Higgs boson production at hadron colliders,” *JHEP*, vol. 07, p. 028, 2003. arXiv:hep-ph/0306211.
- [35] I. Belotelov, I. Golutvin, D. Bourilkov, A. Lanyov, E. Rogalev, M. Savina, and S. Shmatov, “Identification and calibration of boosted hadronic W/Z bosons at 13 TeV,” CMS AN-16-215.
- [36] CMS Collaboration, “Search for physics beyond the standard model in events with high-momentum Higgs bosons and missing transverse momentum in proton-proton collisions at 13 TeV,” *Phys. Rev. Lett.*, vol. 120, p. 241801, 2018. arXiv:1712.08501.
- [37] [https://www-d0.fnal.gov/Run2Physics/top/top\\_public\\_web\\_pages/top\\_feynman\\_diagrams.html](https://www-d0.fnal.gov/Run2Physics/top/top_public_web_pages/top_feynman_diagrams.html).
- [38] Jesse Thaler, Ken Van Tilburg, “Identifying Boosted Objects with N-subjettiness,” *JHEP*, March 2011. arXiv:1011.2268.
- [39] Jesse Thaler, Ken Van Tilburg, “Maximizing Boosted Top Identification by Minimizing N-subjettiness,” *JHEP*, February 2012. arXiv:1108.2701.
- [40] <https://twiki.cern.ch/CMS/TopPtReweighting>.